Nanoscale Thermoelectric Energy Conversion

Yuri M. Zuev

Submitted in partial fulfillment of the
requirements for the degree
of Doctor of Philosophy
in the Graduate School of Arts and Sciences

COLUMBIA UNIVERSITY
2011

ABSTRACT

Nanoscale Thermoelectric Energy Conversion

Yuri M. Zuev

In the last two decades numerous novel nanoscale materials have been synthesized. Electronic characterization is essential for the integration of these materials into current semiconductor devices. The investigation of thermoelectric transport properties of novel materials provides not only an understanding of their effectiveness in energy conversion applications but also insight into their electronic structure. We will present our investigations of the thermoelectric transport properties of semiconducting ZnO and Si nanowires (NWs), phase changing antimony telluride (Sb_2Te_3) NWs, single layer graphene and single walled carbon nanotubes. Since it is often difficult to measure the carrier density of nanowires using a Hall bar geometry, we will present a method to acquire the carrier density through the measurement of the temperature dependence of the thermoelectric power (TEP) in semiconducting NWs. Graphene and carbon nanotubes exhibit both positive and negative values of TEP, with a peak value on the order of k_B/e at room temperature. At high magnetic fields in the quantum Hall regime in graphene, the TEP exhibits characteristic oscillations similar to those found in 2-dimensional electron gases. We explore thermoelectric effects in the presence of Fabry-Perot interference at low temperatures in carbon nanotubes. We analyze the validity of the semiclassical description of transport in these low dimensional carbon materials by comparing the measured TEP to that predicted by the Mott relation.

Contents

Acknowledgments **iv**

1 Introduction **1**
1.1 Thermoelectric effect . . . 2
1.2 Thermoelectric generation . . . 4
1.2.1 Diffusive - semiclassical Mott Relation . . . 4
1.2.2 Phonon-drag TEP . . . 7
1.3 Applications . . . 9
1.3.1 Thermoelectric Figure of Merit, ZT . . . 9
1.3.2 Peltier coolers . . . 11
1.3.3 Power generation . . . 12
1.4 Nanoscale materials . . . 13
1.5 Organization of thesis . . . 16

2 Mesoscopic Measurement technique **18**
2.1 Temperature calibration, on-chip thermometry . . . 19
2.2 DC method vs. AC method . . . 24
2.3 GeSi heterostructure nanowires . . . 26
2.4 Input impedance and frequency dependence . . . 28

3 Carrier density in semiconducting nanowires **30**
3.1 Hall measurement . . . 31
3.2 Conductance and TEP in semiconducting Si nanowires . . . 33
3.3 Measuring carrier density using TEP in Si and ZnO NWs . . . 35
3.4 ZnO nanowire field effect carrier density . . . 37
3.5 Summary . . . 39

4 Diameter dependence of the transport coefficients in chalcogenide nanowires **40**
4.1 Bismuth nanowires . . . 41
4.1.1 Theoretical predictions . . . 41
4.1.2 Experimental values . . . 43
4.2 Antimony telluride . . . 45
4.3 Nanowire synthesis and device fabrication . . . 46

4.4 Diameter dependence 48
4.5 Temperature dependence 50
4.6 Magnetoresistance measurements 52
4.7 Summary 55

5 Thermoelectric transport in graphene **56**
5.1 Linear band structure 57
5.2 Device fabrication 59
5.3 Gate dependence 61
5.4 Semiclassical formalism 63
5.5 Quantum Hall effect in graphene 67
5.6 Magnetothermoelectric transport in graphene 69
5.7 Generalized Mott relation 72
5.8 Summary 74

6 Thermoelectric transport in single walled carbon nanotubes **75**
6.1 Band structure 76
6.2 Device fabrication 78
6.2.1 CNT Synthesis 78
6.2.2 SWNT verification 79
6.3 Transport in the Fabry-Perot regime 81
6.4 Analysis of TEP in the Fabry-Perot regime 84
6.5 Summary 86

7 Conclusion **87**

List of Figures

1.1 TEP basics . . . 3
1.2 Bulk Si phonon drag . . . 8
1.3 Values of efficiency ZT . . . 10
1.4 Peltier cooler . . . 12
1.5 Theoretical predictions of high ZT . . . 15

2.1 Device diagram . . . 20
2.2 Calibration measurement . . . 22
2.3 DC method vs. AC method . . . 24
2.4 GeSi heterostructure nanowires . . . 27
2.5 Impedance and frequency dependence . . . 29

3.1 Hall measurement . . . 32
3.2 Conductance and TEP of Si nanowires . . . 34
3.3 TEP of semiconducting nanowires . . . 35
3.4 Nanowire gate coupling . . . 38

4.1 Bi nanowire theoretical modeling . . . 42
4.2 Bi nanowire experimental values . . . 44
4.3 Antimony telluride nanowire synthesis and device fabrication . . . 47
4.4 Diameter dependence of Sb_2Te_3 nanowire resistivity and TEP . . . 49
4.5 Temperature dependence of Sb_2Te_3 nanowire resistivity and TEP . . . 51
4.6 Magnetoresistance of a Sb_2Te_3 nanowire . . . 53

5.1 Graphene band structure . . . 58
5.2 Graphene device fabrication . . . 60
5.3 Gate dependence of conductivity and TEP of graphene . . . 62
5.4 Semiclassical analysis of measured TEP in graphene . . . 66
5.5 Quantum Hall effect in graphene . . . 68
5.6 Magnetothermoelectric transport in graphene . . . 70
5.7 Generalized Mott relation . . . 73

6.1 Band structure of a (12,0) carbon nanotube . . . 77
6.2 Verification of SWNTs . . . 80
6.3 Conductance and TEP of a SWNT in Fabry-Perot regime . . . 82
6.4 Measured and calculated TEP of a SWNT . . . 84

Acknowledgments

The works in this thesis could not be completed without the help, advice, and support of many individuals. First and foremost, I would like to thank my advisor Philip Kim. Philip has guided my professional abilities from the mindset of an undergraduate to the level of an independent scientist. He taught me many experimental techniques in the lab as well as the benefits of a positive work attitude. When we encountered a problem tinkering with an electronics box one day in the lab, he said "well somebody had to put it together", implying if somebody did it, we can too. Philip has always been there for me when I encountered problems which I had no immediate solutions for and always made sure that I would continue to make progress. Thank you for your continued encouragement, guidance, and direction!

The graduate students and postdocs that I have been privileged to work with have made my experience at Columbia unforgettable. Thank you to Meninder Purewal, who showed me the ropes around the lab when I first started and who I can always count on for a deep discussion of social issues. Thanks to Melinda Han, who introduced me to the sport of kayak polo, was contagious with her enthusiasm for renewable energy development, and with whom I exchanged many ideas about career goals as well as life in general. Thank you to Andrea Young, your enthusiasm for research is inspiring to me and everyone around. Thank you to Yue Zhao, I know I can always count on you for a smile. A big thanks to Mitsuhide Takekoshi, Dmitri Efetov, and Fereshte Ghahari for all of the small day to day favors we do for each other. Thanks to Pablo Jarillo-Herrero, who taught me to focus my attention on specific experimental goals. Thank you to Kirill Bolotin, who taught me that it is important to love the "carpentry" and not just the "table", meaning that enjoying the work is more important than the final product.

I would also like to acknowledge my scientific collaborators. Thank you to Vikram Deshpande for all of the discussions about carbon nanotubes. Thank you to Chenguang Lu for synthesis of the clean and ultra long carbon nanotubes which made possible the carbon nanotube project. Thank you to Willy Chang, who helped me tremendously with the graphene project and was awesome to backpack with in Chile. Thanks to Chul Ho Lee and Gyu Chul Yi in POSTECH University in Korea, for the ZnO nanowire synthesis and measurements. Chul Ho, I will never forget your work ethic and dedication to the project. Thanks to Josh Small, for his pioneering works in nanoscale thermoelectrics. Thank you very much to the two groups at Harvard with whom I collaborated with on the Si, Ge/Si and Sb_2Te_3 nanowire projects, Charles Lieber, Yongjie Hu, and Ying Fang as well as Hongkun Park and Jin Sook

Lee. Thank you to Seung Hyun Lee, Wooyoung Shim, and Wooyoung Lee at Yonsei University in Korea for the Bi nanowire synthesis and fabrication help. Thank you to Jim Hone for stimulating carbon nanotube discussions. Thank you to Matthew Foster and Igor Aleiner for contributing theoretical insight for the graphene project. Thanks to Irving Herman for guidance throughout graduate school. Thank you to Aron Pinczuk for getting me started at Columbia and continued support. Thank you to Chris Marianetti for valuable input for the final version of the thesis.

Lastly, my friends and family have provided me with the personal support with which I was able to focus on my research. Thank you to Andrew Ying, we started the same year in graduate school and went from taking the first class in Solid State Physics to proofreading each others PhD theses. Thank you to Braxton Osting, by explaining seemingly basic concepts in our own fields to each other we understood fundamental research issues on a deeper level. My sincere thank you to my mother and father, who have provided the care and inspiration that one can only dream of from parents. Your unwavering support in good times and in bad has made me a stronger person. Because of your guidance I now know that I can face any challenge that may come to me in the future! Thank you to my sister Julia and her husband Roman, for listening and always being there as well as preparing me for what lies ahead in life. Thank you to my fiance Sarah for your love and support in the final chapter of my graduate school adventure. You are my best friend and I cannot wait to start our life together!

Thank you everybody!

Chapter 1

Introduction

Energy is stored in many different forms in nature. To list a few, it can be stored in the form of chemical bonds, heat, electric fields, and radiation. Energy conversion between any two forms of energy requires a thermodynamic process. The direct conversion of heat energy to electrical energy and vice versa is described by the field of thermoelectricity. The thermoelectric coefficient is a basic property of every material. Many new materials, particularly nanoscale materials (materials whose dimensions are between 1 - 100 nm), have been synthesized in recent years. The effects of size confinement lead to many interesting phenomena that have not been observed before in bulk materials. While electronic characterization is studied extensively in these nanostructures, a thorough study of thermoelectric effects is scarce. The main question this thesis tries to address is what can be learned about a nanoscale material by studying its thermoelectric coefficient.

There are two main answers to this question. First, the thermal response of a material leads to a more fundamental understanding of its electronic structure. Second, the thermoelectric coefficient is central to commercial, industrial, and scientific application of thermoelectric devices, such as Peltier coolers and power generators. Therefore, if nanoscale materials are to be integrated into novel thermoelectric energy conversion devices, thermoelectric properties must be investigated in detail. The investigation of the thermoelectric coefficient leads to a deeper insight into a material's electronic structure as well as an understanding of its effectiveness in energy

conversion applications.

This chapter is organized in the following way. Section 1.1 will describe the basic principles of the thermoelectric effect. Section 1.2 will discuss the semiclassical formalism that will be used to analyze data throughout the thesis. Next, the applications of thermoelectricity will be addressed in section 1.3 discussing the thermoelectric figure of merit ZT (1.3.1), Peltier coolers (1.3.2), and power generation (1.3.3). Since this thesis analyzes close to 10 different materials, some background of nanoscale materials will be mentioned in section 1.4.

1.1 Thermoelectric effect

The electrical resistivity of a material is one of its most basic properties. A high resistivity makes the material an insulator while a low resistivity makes it a conductor. In the laboratory, this property can be measured by applying a voltage gradient across the material. This is the basis for Ohm's Law, $J = -\sigma\nabla V$, where J is the electrical current density, σ is the electrical conductivity, and ∇V is the applied voltage gradient. Applying a temperature gradient leads to several phenomena in the material. A thermal current flows through the material, analogous to the case when an electrical gradient was applied. A thermally induced voltage also appears across the material. Qualitatively this can be understood in the following way depicted in figure 1.1. Hot electrons diffuse from the hot reservoir to the cold reservoir. The diffusion of electrons creates an electric field which in turn creates a voltage built up across the material.

The thermoelectric effect was discovered in 1821 by Thomas Seebeck. It is not surprising that the thermoelectric coefficient is also called the Seebeck coefficient or S for short. It is also referred to as thermoelectric power, thermopower, or TEP for short. All of these names are referring to the same property of a material and they will be used interchangeably throughout the thesis. The thermopower, S, is defined as the thermally induced voltage, $\triangle V$, divided by the applied temperature difference,

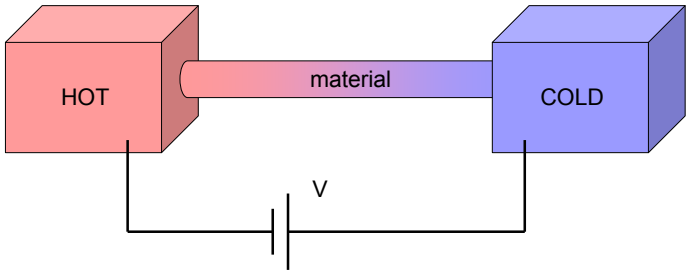

Figure 1.1: A thermally induced voltage appears across a material when it is connected to two temperature reservoirs.

$\triangle T$, when there is no electrical current flowing in a material:

$$S = -\frac{\Delta V}{\Delta T} \tag{1.1}$$

The units of thermopower are $\mu V/K$. SI units will be used throughout the thesis. We will now discuss how the transport coefficients are derived.

The electrical and thermal currents, J and Q, respectively, are related to the electrical and thermal gradients, ∇V and ∇T, respectively, by equation 1.2:

$$\begin{pmatrix} J \\ Q \end{pmatrix} = \begin{pmatrix} L_{11} & L_{12} \\ L_{21} & L_{22} \end{pmatrix} \begin{pmatrix} -\nabla V \\ \nabla T \end{pmatrix} \tag{1.2}$$

If there is no applied temperature gradient, $\nabla T = 0$, then $J = -L_{11}\nabla V = \sigma E$. This is just Ohm's Law and we have $L_{11} = \sigma$, where σ is the electrical conductivity. If no electrical current is allowed to flow in the system, $J = 0$, and $\nabla T \neq 0$ then we have $-\nabla V = \frac{-L_{12}\nabla T}{L_{11}} = S\nabla T$. The thermopower S is then defined as $S \equiv \frac{-L_{12}}{L_{11}}$ so that $L_{12} = -S\sigma$. Using the Onsager relations, $L_{21} = -L_{12}T$, we can immediately see that $L_{21} = S\sigma T = \Pi\sigma$ where Π is the Peltier coefficient. Another way to write the Onsager relations is:

$$\Pi = ST \tag{1.3}$$

We therefore have $L_{21} = ST\sigma$. Lastly, the L_{22} term is the electronic contribution to the thermal conductivity, κ_e. Rewriting equation 1.2 in the final form we have:

$$\begin{pmatrix} J \\ Q \end{pmatrix} = \begin{pmatrix} \sigma & -S\sigma \\ \Pi\sigma & \kappa_e \end{pmatrix} \begin{pmatrix} -\nabla V \\ \nabla T \end{pmatrix} \tag{1.4}$$

In this thesis we primarily focus our attention to investigating the electrical conductivity, σ, and the Seebeck coefficient, S, of a variety of nanoscale materials.

1.2 Thermoelectric generation

In the last section we derived the transport coefficients from general principles based on experimental observations. In this section, we will delve into the semiclassical description of transport using the Boltzmann formalism [1]. The semiclassical Mott relation predicts the expected thermoelectric response of a material based on the behavior of the energy dependence of the conductivity. We will also investigate another method of thermoelectric generation which involves a contribution from the phonons in a material.

1.2.1 Diffusive - semiclassical Mott Relation

When thermopower is generated only by the diffusion of electrons in a temperature gradient in a material, it is referred to as diffusive thermoelectric generation. The Peltier coefficient [2] can be defined as the ratio of the thermal current, Q, carried by the charge carriers to the electrical current, J:

$$\Pi = \frac{Q}{J} \tag{1.5}$$

Qualitatively, the Peltier coefficient can be understood as a measure of the energy carried per unit charge. In the same manner, the thermopower can be understood as a measure of entropy carried per unit charge, if equation 1.3 is considered. Using the semiclassical Boltzmann formalism and the relaxation time approximation, Q and J

are defined to be:

$$Q = \int_0^\infty (\varepsilon - \mu)\sigma(\varepsilon)\frac{df_0}{d\varepsilon}d\varepsilon \qquad J = -e\int_0^\infty \sigma(\varepsilon)\frac{df_0}{d\varepsilon}d\varepsilon \tag{1.6}$$

with the Fermi-Dirac distribution $f_0 = \frac{1}{e^{(\varepsilon-\mu)/k_BT}+1}$ where k_B is the Boltzmann constant, e is the charge of an electron, T is the temperature, ε is the energy, μ is the chemical potential, and $\sigma(\varepsilon)$ is the energy dependent electrical conductivity. Combining equations 1.3, 1.5, and 1.6 we have:

$$S = -\frac{1}{eT}\frac{\int_0^\infty (\varepsilon-\mu)\sigma(\varepsilon)\frac{df_0}{d\varepsilon}d\varepsilon}{\int_0^\infty \sigma(\varepsilon)\frac{df_0}{d\varepsilon}d\varepsilon} \tag{1.7}$$

In the temperature range of interest we have $\mu = \varepsilon_F$. We assume that the energy dependent conductivity is a smooth function of ε around the Fermi energy ε_F, so that we can expand $\sigma(\varepsilon)$:

$$\sigma(\varepsilon) = \sigma(\varepsilon_F) + (\varepsilon - \varepsilon_F)\left.\frac{d\sigma}{d\varepsilon}\right|_{\varepsilon=\varepsilon_F} + \frac{(\varepsilon-\varepsilon_F)^2}{2!}\left.\frac{d^2\sigma}{d\varepsilon^2}\right|_{\varepsilon=\varepsilon_F} + \ldots \tag{1.8}$$

If equation 1.8 is plugged into equation 1.7 we have a series of Fermi integrals. In order to evaluate integrals of this form it is easiest to make some substitutions. Let $x = \frac{(\varepsilon-\varepsilon_F)}{k_BT}$ and $x_0 = \frac{\varepsilon_F}{k_BT}$, so that $\frac{df_0}{d\varepsilon} = -\frac{1}{k_BT}\frac{e^x}{(e^x+1)^2}$. We introduce F_N to be:

$$F_N(x_0) = -\frac{1}{(k_BT)^N}\int_0^\infty (\varepsilon-\varepsilon_F)^N\frac{df_0}{d\varepsilon}d\varepsilon = \int_{-x_0}^\infty \frac{x^N e^x}{(e^x+1)^2}dx \tag{1.9}$$

The integrals in 1.9 can be evaluated numerically or analytically for appropriate values of x_0. The numerator and denominator of 1.7 turn into:

$$\int_0^\infty (\varepsilon-\varepsilon_F)\sigma(\varepsilon)\frac{df_0}{d\varepsilon}d\varepsilon = -(k_BT)F_1(x_0)\sigma_0 - (k_BT)^2F_2(x_0)\sigma_0' + \ldots \tag{1.10}$$

$$\int_0^\infty \sigma(\varepsilon)\frac{df_0}{d\varepsilon}d\varepsilon = -F_0(x_0)\sigma_0 - (k_BT)F_1(x_0)\sigma_0' + \ldots \tag{1.11}$$

where $\sigma_0 = \sigma(\varepsilon_F)$ and $\sigma_0' = \frac{d\sigma}{d\varepsilon}\big|_{\varepsilon=\varepsilon_F}$. Finally, putting it all together, equation 1.7 becomes:

$$S = -\frac{k_B}{e}\left[\frac{F_1\sigma_0 + k_BTF_2\sigma_0' + \ldots}{F_0\sigma_0 + k_BTF_1\sigma_0' + \ldots}\right] \tag{1.12}$$

In the degenerate limit, $\frac{\varepsilon_F}{k_BT} = x_0 \to \infty$, expression 1.12 is simplified, since for odd N, $F_N \to 0$ due to symmetry of the integrand in equation 1.9. The degenerate limit is appropriate in the temperature range of interest. Taking only the leading terms in $(\varepsilon - \varepsilon_F)\frac{d}{d\varepsilon}$ we have:

$$S = -\frac{k_B/e \cdot k_BT\sigma_0'}{\sigma_0}\frac{F_2}{F_0} \tag{1.13}$$

It is easy to show that in the degenerate limit $F_0 = 1$. We can evaluate F_2 analytically in the following way. We again use $x = \frac{(\varepsilon-\varepsilon_F)}{k_BT}$ and $dx = \frac{d\varepsilon}{k_BT}$ so that $f_0 = \frac{1}{e^x+1}$. Using the chain rule, we have $\frac{df_0}{d\varepsilon} = \frac{df_0}{dx}\frac{dx}{d\varepsilon}$. We define $a(x)$ so that $-a(x) = \frac{df_0}{dx} = \frac{-e^x}{(e^x+1)^2}$. Putting it together:

$$F_2 = -\frac{1}{(k_BT)^2}\int_{-\infty}^{\infty}(\varepsilon - \varepsilon_F)^2\frac{df_0}{d\varepsilon}d\varepsilon = \int_{-\infty}^{\infty}a(x)x^2dx \tag{1.14}$$

We note that $a(x)$ is an even function meaning that $a(-x) \equiv a(x)$. It can be expanded as

$$a(x) = \frac{d}{dx}(\frac{1}{1+e^{-x}}) = \frac{d}{dx}(1-e^{-x}+e^{-2x}-e^{-3x}+\ldots) = e^{-x}+2e^{-2x}-3e^{-3x}+\ldots \tag{1.15}$$

Equation 1.14 then becomes:

$$F_2 = 2\int_0^{\infty}x^2(e^{-x} + 2e^{-2x} - 3e^{-3x} + \ldots)dx \tag{1.16}$$

It is noted that the integral is in the following form $\int_0^{\infty}x^2e^{-nx}dx = \frac{d^2}{dn^2}\int_0^{\infty}e^{-nx}dx = \frac{d^2}{dn^2}\left(\frac{e^{-nx}}{-n}\Big|_0^{\infty}\right) = \frac{d^2}{dn^2}(\frac{1}{n}) = \frac{2}{n^3}$, so that equation 1.16 becomes:

$$F_2 = 4\left(1 - \frac{1}{4} + \frac{1}{9} + \ldots\right) = 4\sum_{n=1}^{\infty}\frac{(-1)^{n+1}}{n^2} = \frac{\pi^2}{3} \tag{1.17}$$

where we have summed the series [3] to $\frac{\pi^2}{12}$. We write equation 1.13 in its most familiar form, known as the Mott relation:

$$S = -\frac{\pi^2 k_B^2 T}{3e} \left. \frac{d \ln \sigma}{d\varepsilon} \right|_{\varepsilon=\varepsilon_F} \tag{1.18}$$

We can immediately notice several features of the calculated thermoelectric coefficient. First, it is noted that the diffusive thermopower is linearly proportional to temperature. Second, the thermopower is proportional to the derivative of the conductivity evaluated at the Fermi energy which means that the thermopower is much more sensitive to variations of the electronic structure than the conductivity itself. The sign of the thermopower is proportional to the sign of the charge majority carrier i.e. positive for holes and negative for electrons. In fact, experimentally the thermopower is often used to determine the carrier type in semiconducting materials with unknown doping. This can be qualitatively understood from the Drude conductivity $\sigma = \frac{ne^2\tau}{m^*}$, where n is the charge carrier density, e is the charge of an electron, m^* is the effective mass, and τ is the relaxation time, as well as the fact that the curvature of the bands is positive for electrons and negative for holes.

The Mott relation will be used extensively as an analysis tool throughout the thesis in order to ascertain the validity of semiclassical description of transport in many of the materials we study. Since single particle formalism was used in the derivation, the presence of electron-electron interactions in a material could affect the thermoelectric response in a way that is different from what is predicted by the Mott relation. By comparing the measured and predicted thermoelectric response, we gain a deeper understanding of scattering mechanisms and electronic structure of a material. We now turn our attention to the other method of thermopower generation, the phonon-drag term.

1.2.2 Phonon-drag TEP

The total thermopower of a material is the sum of the diffusive term and the phonon-drag term [4], $S_{\text{total}} = S_{\text{diffusive}} + S_{\text{phonon-drag}}$. Qualitatively, the phonon-drag TEP

results from the diffusion of phonons in the material due to the applied temperature gradient. The phonons themselves do not carry any charge, however, they do scatter with electrons and drag them along, adding to the total thermopower generated. The relative size of the phonon-drag term in comparison to the diffusive term is proportional to the strength of the electron-phonon coupling in a material. In degenerate electron systems ($\varepsilon_F \gg k_B T$), the phonon-drag TEP can be distinguished from the diffusive component by a non-linear temperature dependence of the TEP. At low temperatures, the thermal conductivity rises as T^3 in bulk materials until the onset of umklapp scattering. As a result, the TEP increases superlinearly until it reaches the unklapp scattering regime, and falls back down to the linearly increasing diffusive TEP value.

There is a caveat to this formalism in semiconductors. In highly doped semiconductors, the phonon thermal current is suppressed due to scattering with ionized impurities. Therefore only the diffusive TEP term will appear in highly doped semiconductors. The experimental observation of this effect in bulk Si can be seen in figure 1.2[1]. In the temperature dependence plot most of the lightly doped samples

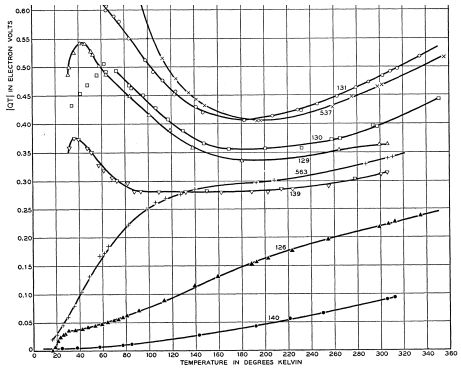

Figure 1.2: Temperature dependence of the thermoelectric response of bulk Si samples with different doping levels, reproduced from [5] with permission. The TEP$\cdot T$ $[eV]$ is plotted as a function of T[K].

show nonlinear contributions from the phonon-drag term, and only the very highly

[1]Reprinted figure 1 with permission from T. H. Geballe and G. W. Hull, Physical Review 98, 940 (1955) © 1955 by the American Physical Society.

doped sample, labeled 140, shows a purely diffusive contribution. In all of the materials studied in this thesis the observed thermopower is dominated by the diffusive contribution, however, it is still important to be aware of the alternative method of thermopower generation. Now that the basic principles of thermopower generation have been addressed, it is time to understand how the thermoelectric property of a material is useful in the real world.

1.3 Applications

The thermoelectric effect is used in several energy conversion applications, most notably solid state cooling and power generation. This section will explore the transport characteristics of various bulk materials which make them suitable thermoelectric devices [6]. The thermoelectric effect is also commonly used to measure temperature in a laboratory with the use of thermocouples. Since the thermoelectric coefficient is different in two dissimilar metals, the voltage that forms at the junction of the metals can be used to accurately determine the temperature in an experimental setup. In this section, we will first investigate the thermoelectric figure of merit, ZT, which is an important measure of efficiency of a thermoelectric device. Solid state cooling devices, such as Peltier coolers, will be discussed next. The last section will cover power generation applications.

1.3.1 Thermoelectric Figure of Merit, ZT

The efficiency of every thermodynamic energy conversion process is limited by the Carnot efficiency [7]. A thermoelectric energy conversion process is no different. The measure of efficiency in a thermoelectric device is the thermoelectric figure of merit, ZT, defined to be:

$$ZT = \frac{S^2 \sigma T}{\kappa} \tag{1.19}$$

where S is the thermopower, σ is the electrical conductivity, T is the absolute temperature, and κ is the thermal conductivity. In order to maximize ZT, it is clear

that both the thermopower and electrical conductivity have to be high while the thermal conductivity must be low. Most materials have either both high electrical and thermal conductivity or both poor electrical and thermal conductivity. However, there are a group of elements that have a moderately high electrical and Seebeck coefficients while having poor thermal conduction properties. A thermoelectric device works only if there is an appreciable temperature gradient across it. Therefore thermoelectric materials must have a low thermal conductivity, otherwise the device would be thermally shorted.

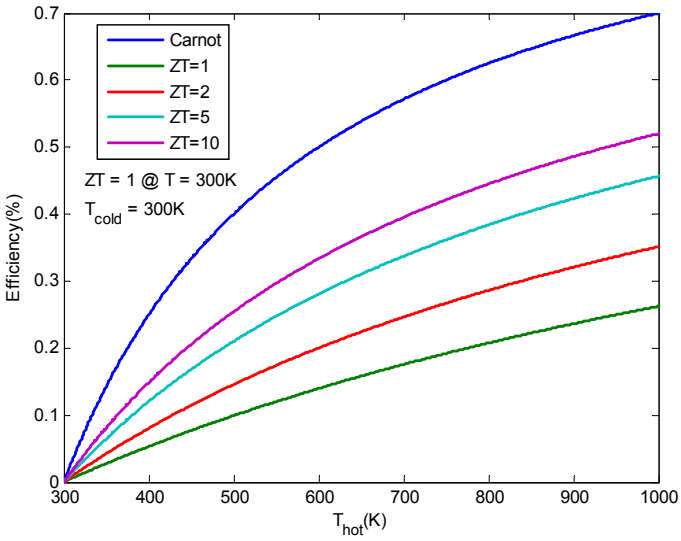

Figure 1.3: Values of the thermodynamic efficiency for several different ZT values.

Alloys of Antimony, Tellurium, Lead, and Bismuth are most commonly used in room temperature thermoelectric devices because the ZT of these materials is close to 1. In a thermoelectric power generation device the figure of merit ZT relates to the thermodynamic efficiency, η, by the following relationship [8]:

$$\eta = \frac{T_H - T_C}{T_H} \frac{\sqrt{1 + Z\bar{T}} - 1}{\sqrt{1 + Z\bar{T}} + \frac{T_C}{T_H}} \tag{1.20}$$

where T_H is the temperature of the hot side, T_C is the temperature of the cold side, and $\bar{T} = \frac{T_H + T_C}{2}$. The overall efficiency of a thermoelectric device is of coarse limited

by the Carnot term, $\frac{T_H - T_C}{T_H}$, in front. Figure 1.3 shows a comparison of the efficiencies using equation 1.20 with the cold side temperature set to $T_C = 300$ K. We can see that with $ZT = 1$, the efficiency of a thermoelectric power generator, with $T_H = 600$ K, is about 10%. Comparing that to the Carnot limit of 50%, thermoelectric energy converters are not very efficient. In order to make thermoelectric devices commercially competitive with vapor-compression systems, like refrigerators and air conditioners, materials with a $ZT > 3$ must be found.

Since the 1950's the maximum achievable room temperature ZT has been around 1 [9]. However, in the last two decades there have been breakthroughs in material synthesis that have lead to experimental observations of $ZT > 1$. There will be more discussion about recent developments in nanostructured materials in section 1.4 as this is one of the main motivations for the work in this thesis.

1.3.2 Peltier coolers

The Peltier cooler is a solid state cooling device [10]. Even though it was shown in the last section that the efficiency of thermoelectric devices is quite low, these devices have several advantages compared to traditional vapor-compression systems. There are no moving parts in a thermoelectric device which makes them extremely robust, very quite, and last for years. Modern microprocessors generate a tremendous amount of heat which has to be dissipated in order to maintain computational performance. The Peltier cooler's compact size, down to a few millimeters, makes them compatible with on-chip cooling applications where even microfluidic systems can not be implemented. Peltier coolers work on the bases of the Peltier effect, which is very similar to the Seebeck effect. It can be seen from equation 1.4 that there is a thermal current that flows in a material as a result of an applied voltage gradient, $Q = -\Pi\sigma\nabla V$. Since the Peltier coefficient is material dependent, there will be a discontinuity in the flow of the thermal current Q at a junction of two dissimilar materials. As a result of this discontinuity, some amount of heat is generated or absorbed at a junction of dissimilar materials. An example of the Peltier cooler operations is shown in figure 1.4. The yellow and orange legs depicted in the diagram represent n-type and

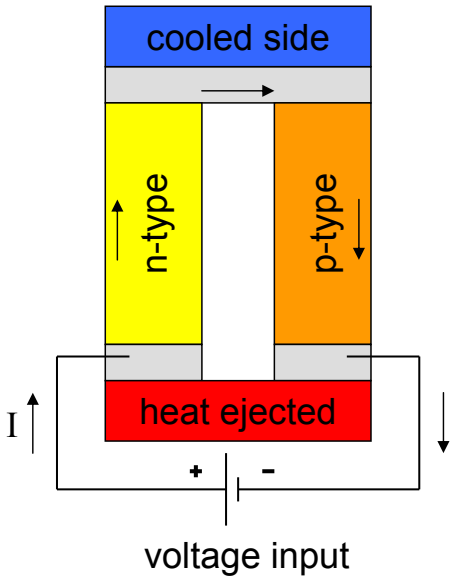

Figure 1.4: Schematic diagram of the operation of a Peltier cooler, showing the n-type and p-type semiconductor components typically used inside of devices. The arrows show the direction of the flow of electrical current.

p-type semiconducting materials, typically used in Peltier coolers.

1.3.3 Power generation

The majority of energy loss in thermodynamic energy conversion is dissipated as waste heat to the surrounding environment. There is a tremendous amount of waste heat generated in industrial manufacturing, car engines, as well as many other everyday energy conversion systems. If that heat could be recovered, there would an incredible savings of energy. This is precisely the goal of thermoelectric power generators. The hot side of a thermoelectric device would be coupled to a heat source, such as an engine, while the cold side would be coupled to a cooling reservoir. The voltage produced across the thermoelectric element is used to charge a battery, thus storing electrical energy. Both GM and BMW have recently demonstrated prototype thermoelectric generator units which employ skutterudite mineral materials as the active elements. The system couples the hot side of the thermoelectric device to the exhaust gas and the cold side to the radiator of a car. Since the exhaust gas

of a typical automobile is at approximately 800 K while the radiator is roughly at room temperature, there is a significant thermal gradient that can can be utilized by thermoelectric power generation devices. The BMW prototype improves the overall vehicle fuel efficiency by 5%. This may not seem like much, but considering the number of cars on the streets today, it would be a considerable amount of energy saving if implemented on a large scale.

There is another direct application of thermoelectric devices that is used in deep space probes. Deep space satellites, such as the Cassini probe that surveyed Saturn, are too far from the sun in order to use standard photovoltaic cells for power generation. The source of energy in such spacecraft is provided by a radioisotope thermoelectric generator which uses a radioactive material as a heat source. Alloys of Si and Ge have high ZT values [11] at elevated temperatures and are considered to be the best high temperature thermoelectric materials. These materials are used as the active thermoelectric elements in the radioisotope devices. Spacecraft with these power generators have operated without maintenance for decades, which exemplifies the robust nature of these power generators.

This section has focused on the applications of the thermoelectric property of bulk materials. The basic properties of these materials has been known for many years. There are many newly synthesized materials, such as nanotubes, nanowires, supperlattice arrays, etc., whose basic properties have not been studied. The next section will go over recent progress in materials design and how it pertains to the field of thermoelectrics.

1.4 Nanoscale materials

New nanoscale materials have been recently created due to advances in synthesis technology, namely molecular beam epitaxy (MBE), chemical vapor deposition (CVD), and the vapor-liquid-solid (VLS) technique. There are several very interesting review articles [6, 9, 11] that go through recent developments in nanomaterials for thermoelectric applications. Structures that are on the order of nanometers in size are

different than their bulk counterparts because their dimensions become comparable to other length scales in the system. For example, if a nanowire diameter becomes smaller than the phonon mean free path, then the phonon mean free path will be limited by boundary scattering. Indeed, limiting the mean free path of phonons by introducing additional scattering centers or boundaries is exactly what many researchers have done in order to improve the thermoelectric efficiency of materials. One strategy to improve ZT is to minimize the thermal conductivity term κ in the denominator, while another is to increase the power factor term $S^2\sigma$ in the numerator.

Since the dominant contribution to the thermal conductivity comes from the phonon contribution, scattering phonons more effectively is the primary method to decrease the thermal conductivity in a material. The groups from Berkeley [12] and Caltech [13] have introduced surface roughness to Si nanowires in order to suppress the thermal conductivity and enhance thermoelectric performance. It is very important to maintain the high level of electrical performance while suppressing the thermal contribution because suppressing both will not improve ZT. This is possible in Si nanowires because the electron mean free path is already much smaller than the phonon mean free, so increasing the boundary scattering will not suppress the electrical conductivity. These studies depict the proof-of-concept experiments that verify that indeed nanowires are more efficient than their bulk counterparts. However, in order to make commercial nanowire devices that perform better than existing thermoelectric devices, an ensemble of the nanowires with correct placement and orientation has to be produced. Whether this can be accomplished, and whether it can be accomplished in a cost effective manner, is still a wide open question [14, 15].

In order to avoid the problems of nanowire assembly a different strategy has been used by the MIT group. Hot pressing nanopowers that were ball milled from bulk bismuth antimony telluride produced nanocrystalline materials that have an enhanced ZT = 1.4 at $T = 100°C$ [16]. The grains in the nanopowders are crystalline which makes the material a good electrical conductor. However, grain boundaries and other defects scatter phonons more effectively reducing the thermal conductivity and increasing ZT. Another approach to increasing phonon scattering was used by

making a superlattice structure of alternating layers of bismuth telluride (Bi_2Te_3) and antimony telluride (Sb_2Te_3) [17]. This work has produced a material with the current world record ZT = 2.4 at $T = 300$ K. One advantage of a superlattice structure is that it could potentially be used to create an electronic structure with only specific allowable energy states. Manipulating the electronic structure in such a way could result in an enhancement of the power factor.

There are some theoretical prediction about what ZT values can ultimately be achievable by manipulation of the electronic structure of a material. If electronic transport is reversible the entropy of the system will not increase. Conditions that approach this limit are derived for a model of a quantum dot superlattice or a superlattice nanowire thermoelectric device [18]. The optimum electronic density of states is shown to be a delta function. Figure 1.5a[2] shows the predictions of room temperature ZT values for different superlattice parameters as a function of the lattice thermal conductivity. Quantum confinement effects in Bi nanowires have also

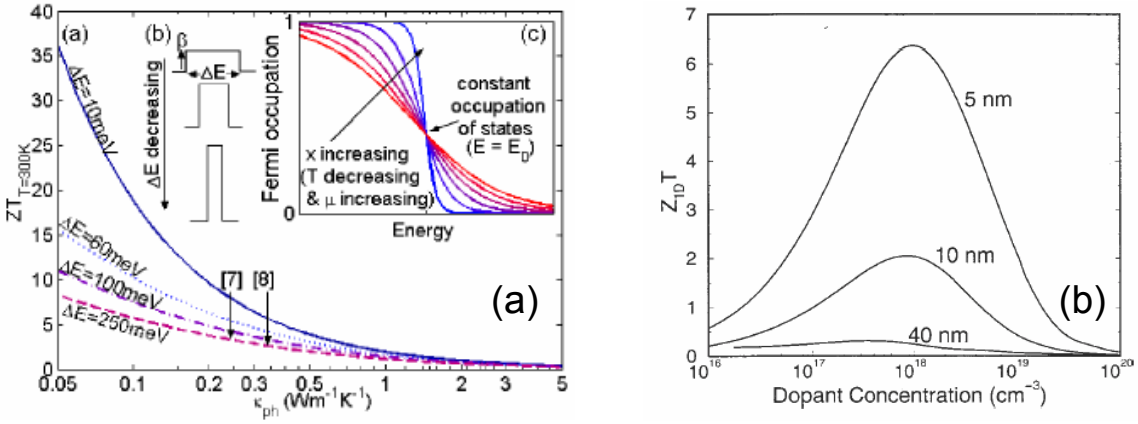

Figure 1.5: (a) Theoretical predictions of ZT values at $T = 300$ K of a thermoelectric superlattice device, reproduced from [18] with permission. (b) Theoretical predictions of ZT values at $T = 77$ K of Bi nanowires of different diameters, reproduced from [19] with permission.

been predicted to lead to enhancement of thermoelectric performance [19, 20]. As the

[2]Reprinted figure 2 with permission from T. E. Humphrey and H. Linke, Physical Review Letters 94, 096601 (2005) © 2005 by the American Physical Society.

wire diameter is decreased a semimetal-semiconductor transition occurs and a band gap is predicted to open in the band structure. Figure 1.5b[3] shows the theoretically predicted ZT values at $T = 77$ K for Bi nanowires of different diameters. It can be observed that the ZT depends sharply on the carrier concentration in the nanowire, therefore it is essential to be able control the carrier concentration in a nanowire.

A convenient and practical method to control the carrier concentration in nanoscale materials is by using a capacitively coupled gate electrode. The measurement technique used in references [12] and [13] allows the observation of the thermal conductivity because the nanowire is suspended. However, the carrier density in the nanowire is constant and cannot be adjusted by a gate voltage. One of the critical elements in the method that we use to investigate transport properties of materials is the ability to apply a gate voltage and thereby control the carrier density and in turn the Fermi energy of the material. This allows us to investigate many interesting phenomenon in nanoscale materials.

1.5 Organization of thesis

This thesis is organized by material type. Every chapter will discuss the properties of a single material or a group of related materials. In order to understand how to measure the electronic and thermoelectric properties of a nanoscale material, chapter 2 will showcase the details of the novel measurement technique by presenting the measurements taken on GeSi core-shell heterostructure nanowires. We will investigate how to determine the carrier density in semiconducting ZnO and Si nanowires with temperature dependent TEP measurements in chapter 3. Chapter 4 will examine the transport properties of Bi nanowires and chalcogenide Sb_2Te_3 nanowires and how they scale with nanowire diameter. Next we turn our attention to two low dimensional carbon materials, graphene and carbon nanotubes. In chapter 5, we investigate

[3]Reprinted figure 5 with permission from Y. Lin, X. Sun, and M. S. Dresselhaus, Physical Review B 62, 4610 (2000) © 2000 by the American Physical Society.

the thermoelectric response of graphene and how it compares to the calculated thermoelectric response using semiclassical formalism. We also observe the Nernst effect and the quantum Hall effect in this 2-dimensional carbon sheet. Chapter 6 will focus on the transport properties of highly conducting carbon nanotubes as we cool them down to observe the Fabry-Perot interference regime. The last chapter will make some conclusions. There is a lack of understanding of basic properties of newly synthesized nanoscale materials. We address this issue and try to fill the gap in the works of this thesis.

Chapter 2

Mesoscopic Measurement technique

In order to measure the transport properties of nanoscale materials many fabrication and measurement techniques have been developed. Measuring electrical conductance is relatively straight forward. It requires contacting the material with metal electrodes, applying a bias voltage, and measuring a current. Applying a voltage gradient across a material is trivial. However, applying a calibrated thermal gradient across a material requires some experimental savvy. Samples containing a distributed mesh of carbon nanotubes (called "mat" samples) can be measured using a traditional experimental techniques [21]. It is difficult to observe the intrinsic transport properties of individual nanostructures using such techniques, however, because numerous tube-tube junctions often dominate the measured signal. Gate control of the carrier density in the nanostructures is also needed in order to study many phenomena. In order to study the thermal transport properties of individual nanostructures the capability to measure temperature with a spatial resolution on the order of hundreds of nanometers is needed. This chapter will discuss the measurement technique developed to simultaneously measure electrical conductance and thermopower of nanoscale materials. We will discuss the thermometry method that is used to estimate the temperature difference across a material in section 2.1. Section 2.2 will compare the measurement methods using DC and AC sources. Section 2.3 will discuss the background of the GeSi heterostructure nanowire system which is used to demonstrate the capability of the measurement technique. Lastly, we will discuss the role of input impedance of

the measurement apparatus on the measured TEP values in section 2.4.

2.1 Temperature calibration, on-chip thermometry

In order to measure the Seebeck coefficient, a controlled temperature gradient must be applied across a material. Maintaining a temperature gradient requires a heat source and a heat sink. The heat source can be provided by a metal wire which produces a power output because of Joule heating [2]. The heat sink is a large thermal reservoir maintained at a constant temperature. For bulk materials, traditional techniques employing small 36 gauge wires and thermocouples are used [22]. Although this method is effective for measuring macroscopic size samples, it is inadequate for measuring nanowires and nanotubes. What is needed is an on-chip thermometry technique with a spatial resolution of $\sim$100 nm.

Thermometry can be performed using several different techniques [23]. Most commonly, the resistance of a pre-calibrated resistor or a Si diode is used to measure the temperature of a sample. These thermometers are calibrated with respect to known temperature reference points such as the boiling point of liquid nitrogen or liquid helium. Commercially available temperature calibrated resistors are rarely smaller than 1 mm in diameter and would be incompatible with the requirement to measure the temperature difference at two points on a wafer that are separated by 1 μm. We employ microfabricated metal thermometers with widths of 100 nm to measure local temperature variations. Details of the fabrication procedures will be discussed later in section 4.3. Resistance of a metal, R, is linearly proportional to temperature, T, due to phonon scattering [1], so by carefully measuring the resistance of a metal electrode the temperature can be attained. Figure 2.1 shows a diagram of the 10 electrode device used to measure local temperature variations. The 2-probe electrode near the top is the heater electrode, while the two 4-probe electrodes are used as thermometers and as electrodes. Although a nanowire (shown in green) is depicted here, this technique is applicable to a wide variety of molecular nanostructures.

The substrate that is used for our measurements is a degenerately doped Si with a

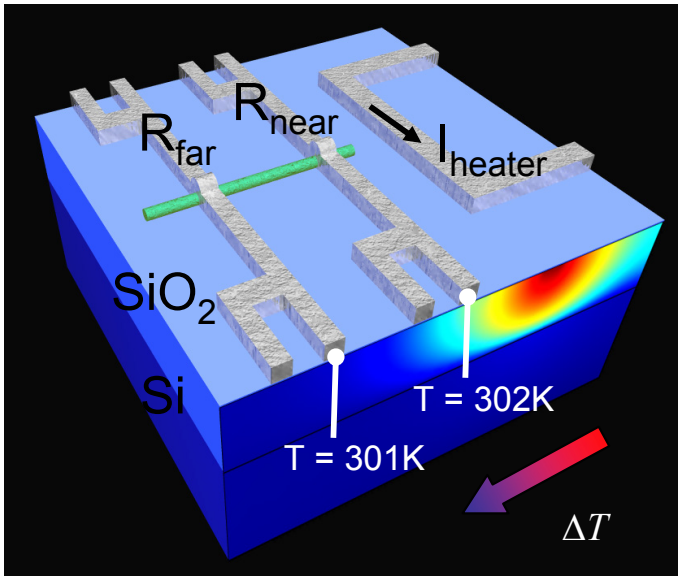

Figure 2.1: Diagram of the device setup showing the heater and 2 microthermometer electrodes. The cross section view shows a finite element simulation of the temperature distribution profile in the substrate that was made using the COMSOL software package.

thermally grown SiO_2 layer. The oxide thickness is an important parameter because it determines the device geometry. The separation between the heater and the near electrode should be on the order of the oxide thickness. A finite element simulation, made using the COMSOL software package, of the cross section of the substrate along the central axis of the device can be seen in figure 2.1. In can be seen that the majority of the heat is dissipated into the substrate, however, there is still a lateral temperature gradient because the thermal conductivity of Si is ∼100 times greater than that of SiO_2. Table 2.1 shows a comparison of the thermal conductivities of several materials at $T = 300$ K [1, 24]. If the dielectric substrate is more thermally

Table 2.1: Thermal conductivities of several materials at $T = 300$K [1, 24].

material	air	SiO_2	HfO_2	BN	Si	Cu	Ag
thermal conductivity [W/mK]	.025	1.5	23	30	150	400	430

conductive, such as in the case of hafnium oxide (HfO_2) or boron nitride (BN), the

resulting lateral temperature gradient will be larger. The majority of the thermal current flows in the dielectric layer because the thermal conductance of the nanoscale material studied is incomparably small, except for the case of graphene. Graphene samples have a significant thermal conductance and slightly alter the heat flow path in the devices at high temperatures close to $T = 300$ K. It is assumed that the nanoscale material and the thermometer electrodes are at the same temperature as the substrate (also confirmed by the simulations) because the thermalization takes place on a much faster timescale than the measurement frequency. For all materials investigated in this thesis a 950 nm thick SiO_2 substrate was used, except for graphene where a 300 nm thick SiO_2 substrate was used. The following boundary conditions were used in the simulations. The heater is set to a constant temperature, which is appropriate in steady state conditions. The bottom of the Si substrate acts as a reservoir and is set to the base temperature because it has a tremendous thermal mass, compared to the nanowire device, and is being kept at a constant temperature by the cryostat. All of the other exterior surfaces are set to insulating because the sample is maintained at a vacuum level of 10^{-6} Torr in the Janis continuous flow cryostat so that there are no convective heat losses and radiation losses are negligible.

To carefully measure the resistance of the metal thermometers we use an equivalent of an AC bridge [25]. The 4-terminal geometry is used in order to eliminate the resistance of the leads and only measure the resistance of the small length of the thermometer line near the heater. This is done because the heating is done locally, and the change in the 2-terminal resistance is below detectable levels. Figure 2.2a shows the circuit diagram used to measure the resistance changes employing a DC voltage source and 2 lock-in amplifiers. We typically use Stanford Research Systems (SRS) model SR830 lock-in amplifiers for ease of use and excellent signal-to-noise ratio. A current limiting resistor, $R_h = 1$ kΩ, is typically used with the DC source that supplies the power to the heater electrode. For each 4-terminal measurement, we convert an AC voltage source (lock-in signal generator) to a constant AC current source by using a large resistor, $R_0 = 100$ kΩ typically, such that $R_0 \gg R_{\text{thermometer}}$. Its best to perform the resistance measurement simultaneously using 2 lock-in amplifiers in

order to improve reproducibility. Two frequencies that are not harmonics of each other, $\omega_1 = 17$ Hz and $\omega_2 = 91$ Hz typically, must be used in order eliminate cross-talk between the near and far electrodes. The typical excitation current that is

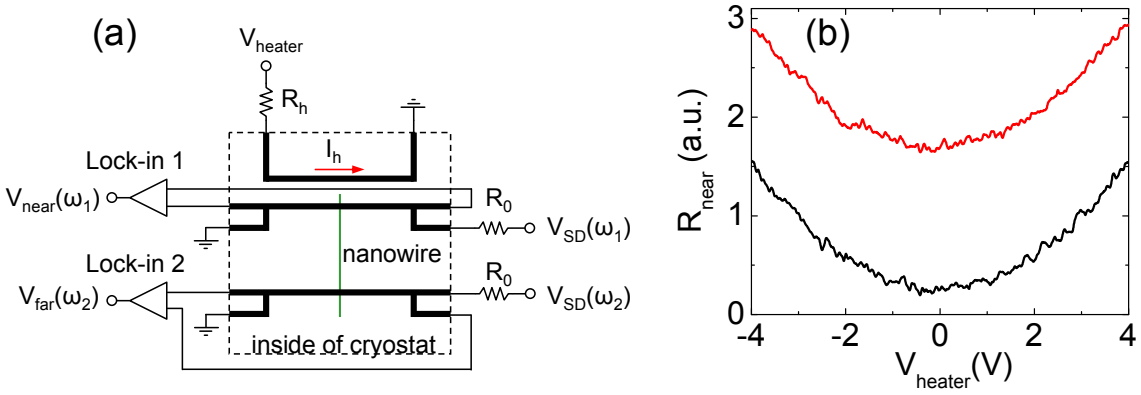

Figure 2.2: (a) Circuit diagram of the bridge method used to accurately measure the resistance of the metal thermometers. (b) Microthermometer resistance as a function of heater voltage for two different cryostat base temperatures.

used is $I_{\mathrm{AC}} = 5\ \mu$A. We use the "Offset" and "Expand" functions on the lock-in amplifier in order to digitally enhance the small changes in resistance produced by the temperature gradient. The value that has been empirically observed for the temperature coefficient of resistance of Ni electrodes is $\sim$1 Ω/K. Considering that the heater electrode can induce only a few degrees K temperature difference, the bridge method is indispensable to measure the small changes in resistance.

Typical resistance versus heater voltage curves are shown in figure 2.2b for two different cryostat temperatures. The change in resistance is proportional to the change in temperature which in turn is proportional to the power $\mathrm{P} = \mathrm{V}^2_{\mathrm{heater}}/\mathrm{R}$ produced in the heater electrode. Since $R_{\mathrm{thermometer}} \propto V^2_{\mathrm{heater}}$, we fit the curves with second order polynomials. We take the difference of the two parabolas to get a relationship between resistance and temperature of each thermometer. In order to get reproducible temperature calibration curves, it is necessary to sweep $\mathrm{V}_{\mathrm{heater}}$ slowly and take an average of multiple traces. Since the resistance of the heater and the microthermeters as well as the thermal conductivity of the Si/SiO_2 substrate varies as a function of

temperature, the calibration measurement has to be performed at every individual temperature point.

The largest source of error in determining the TEP in any material results from the calibration measurement. The majority of the error results from systematic fluctuations of background temperature in the cryostat and not from the statistical error during the parabolic fitting. It is critical to maintain the background cryostat temperature at a stable setpoint. For temperatures above 15 K the error in calibration is less than 5%. Temperature calibration is difficult and can be unreliable below 15 K. Below 15 K the signal-to-noise ratio becomes quite poor because resistance as a function of temperature in metals goes to a minimum and even starts to increase as a function of decreasing temperatures presumably due to Kondo impurity scattering in the Au thermometers [1]. If the the signal-to-noise ratio is poor and noise levels cannot be reduced, then the natural course of action is to increase the signal strength. However, there are 2 problems with increasing V_{heater} too much. First, since we are interested in the linear response regime when studying the transport coefficient of a material, the relationship $\Delta T \ll T$ must be maintained. Second, if the heater resistance is too low, increasing V_{heater} leads to a large I_{heater}. Electromigration typically occurs in Cu and Al lines at current densities on the order of 10^7 A/cm^2 [26]. Electromigration in our 200 nm wide heater lines occurs between 10^7 A/cm^2 and 10^8 A/cm^2, depending on the metal used, so it is recommended to keep $J_{heater} < 3{\times}10^7$ A/cm^2 to not break the heater electrode. In order to acquire a reliable temperature calibration measurement it is important to keep the signal larger than the noise floor but smaller than the electromigration limit.

Now that we understand how to apply a controlled temperature gradient on the micrometer scale, we turn our attention to the technique used to measure the quantity we are ultimately interested in, the thermopower.

2.2 DC method vs. AC method

In order to measure the thermally induced voltage across the material the thermometer electrodes are used as voltage probes. We utilize a DC method as well as an AC method to increase the rate of data acquisition. Figure 2.3a shows the circuit diagram of the DC method. The voltage probes used have a high input impedance so that no electrical current flows through the sample. The heater voltage is swept in the identical configuration as in the calibration measurement. A DC voltage amplifier, SR560 typically, is used to measure the thermally induced voltage in the nanoscale material. Since the resulting curves are parabolic in shape, taking the difference of the highest and lowest point of the second order fit produces the thermoelectric voltage. The thermopower is calculated using $S_{DC} = -\frac{\Delta V}{\Delta T}$. It is noted that the temperature gradient in the SiO_2 substrate is not-linear. The voltage difference that is measured can be defined [8] as the sum of the voltages produced along each segment of the material $\Delta V = \int_0^L S(x)\frac{dT}{dx}dx$. It is assumed that the Seebeck coefficient is approximately constant throughout the material, $S(x) \approx S$, so it does not matter that the exact temperature profile $T(x)$ is not known. As long as the total ΔT is known, the measured ΔV can be used deduce the intrinsic S of the material. By applying a gate

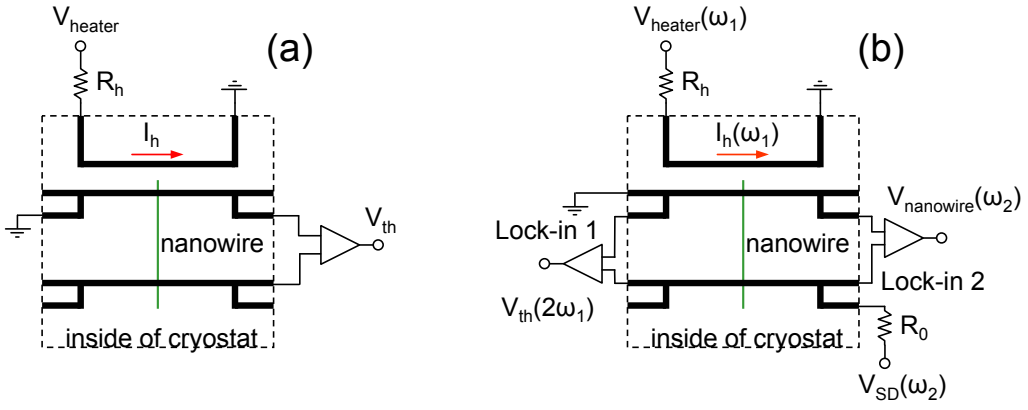

Figure 2.3: (a) Circuit diagram of the DC method. (b) Circuit diagram of the AC method showing simultaneous measurements of conductance at ω_2 and TEP at $2\omega_1$.

voltage, V_g, the carrier density and therefore the Fermi energy in a material can be

adjusted. In order to measure TEP as a function of V_g using the DC configuration, the heater voltage must be swept through the full range at every gate voltage point. The so called megasweep can take 10 hours and is susceptible to several sources of error including temperature fluctuations as well as gate hysteresis. The AC method is an alternative solution to many of these problems.

Applying an AC voltage at frequency ω_1 to the heater electrode produces a thermal gradient along the substrate at frequency $2\omega_1$. Figure 2.3b shows the circuit diagram of the AC method, showing simultaneous measurements of conductance and TEP. With the sine output, the lock-in amplifier produces a waveform with an amplitude, V_0, but displays the root-mean-squared (RMS) value $V_{\text{lock-in}}$:

$$V_0 = \sqrt{2} V_{\text{lock-in}} \cos(\omega_1 t) \tag{2.1}$$

Following the same method of reasoning as in the previous section, the temperature gradient can be written in the following way:

$$\Delta T_{AC} = \beta P = \beta \frac{V_0^2}{R_{\text{heater}}} = 2\alpha V_{\text{lock-in}}^2 \cos^2(\omega_1 t) = \alpha V_{\text{lock-in}}^2 \cos(2\omega_1 t) + \alpha V_{\text{lock-in}}^2 \tag{2.2}$$

where β and $\alpha = \beta / R_{\text{heater}}$ are unknown constants, the first term on the right hand side is the AC component and the second term is the DC component. The amplitude of the oscillating part of the temperature gradient is then $\Delta T_{AC} = \alpha V_{\text{lock-in}}^2$ where α is acquired empirically during the calibration measurement. Since the lock-in amplifier also detects the RMS value of the signal, $\Delta V_{th}(2\omega_1)$, the final thermopower can be acquired using the following relationship:

$$S_{AC} = -\frac{\sqrt{2}\Delta V_{th}(2\omega_1)}{\Delta T} \tag{2.3}$$

It should be noted that there is a 90° phase shift in the signal due to the lock-in electronics, so that $V_{th}(2\omega_1)$ should be measured on the Y channel of the lock-in amplifier. In every material studied, the S value obtained using the AC method is always cross checked with the value obtained by the DC method such that $S_{AC} \approx$

S_{DC} in order to eliminate any potential systematic error. The AC method allows to measure the TEP as a function of gate voltage in a matter of minutes. It should be noted that the measured thermopower is the difference of the thermopower generated by the material and the thermopower generated by the electrical leads. However, the thermopower in metals is generally very small, typically a few $\mu V/K$ [4], and is not gate voltage dependent, which means that there is a small offset in the TEP that is subtracted in order to obtain intrinsic TEP values.

The AC method also allows the simultaneous measurement of conductance and TEP, which is critical in order to compare the measured thermoelectric response to that predicted by the Mott relation (equation 1.18). This is something that is unique in our device geometry and measurement method. It is difficult to uniformly change the carrier density in a bulk material due to electronic screening. However, in materials such as carbon nanotubes and graphene, with a thickness on the order of 1nm, a capacitively coupled gate electrode changes the carrier density throughout the material. Therefore, the AC method allows us to directly check the validity of the semiclassical Mott relation in these materials. Section 2.4 will go over some details of the measurement technique by showing data taken on GeSi heterostructure nanowires.

2.3 GeSi heterostructure nanowires

The semiconducting Ge/Si heterostructure nanowire (NW) system is an ideal material to test out the limits of the AC method. This section will briefly discuss the basic transport properties of the material. The electronic properties of Ge/Si heterostructure NWs have attracted substantial attention for use in next generation field effect transistors (FET) [27–30]. The nanowires were synthesized in collaboration with the Lieber group at Harvard University. The details of the VLS synthesis of the core/shell Ge/Si heterostructure nanowires, with diameters in the range of 12±2 nm, have been described in reference [27]. There is a ∼500 meV band offset between Ge and Si,

shown in figure 2.4a[1]. The quantum well that is formed at the interface of the Ge

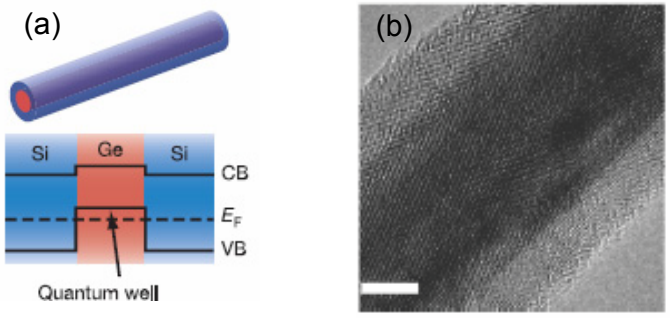

Figure 2.4: (a) Schematic and band diagram of the Ge (core) and Si (shell) heterostructure which forms a 1D hole gas at the interface, reproduced from [28] with permission. (b) TEM image of a cross section of the nanowire with the scale bar of 5 nm, reproduced from [27] with permission.

and Si produces a 1D hole gas. FET devices were fabricated with 50nm Ni electrodes because this metal easily diffuses through the Si outer shell and makes contact to the 1-dimensional hole gas. Ohmic contact was achieved by rapid thermal annealing (RTA) essential for the elimination of a Schottky barrier between the electrode and the semiconducting nanowire. We used a Heatpulse 610 RTA system and annealed the devices at 300°C for 15 s in forming gas (N_2/H_2, 90/10%). Figure 2.4b[2] presents a cross sectional transmission electron microscope (TEM) image of the Ge/Si nanowires showing good crystallinity of the synthesized heterostructure.

Conduction in this p-type semiconducting material can be adjusted by a capacitively coupled gate electrode to be high when the device is in the "on" regime and low when it is in the "off" regime. As positive gate voltage is applied, the device turns off and the current drops to levels below the noise floor. The impedance of the device in this regime becomes exceedingly high, $Z > 100$ MΩ, and measuring TEP becomes problematic using the AC method. Since the impedance of Ge/Si devices can

[1]Reprinted by permission from Macmillan Publishers Ltd: Nature (J. Xiang, W. Lu, Y. Hu, Y. Wu, H. Yan, and C. M. Lieber, Nature 441, 489 (2006)) © (2006).

[2]Reprinted by permission from W. Lu, J. Xiang, B. P. Timko, Y. Wu, and C. M. Lieber, Proceedings of the National Academy of Sciences of the United States of America 102, 10046 (2005) © 2005 National Academy of Sciences, U.S.A.

be adjusted above and below the input impedance of the measurement instruments, this material is used to investigate the range of applicability of the AC measurement method.

2.4 Input impedance and frequency dependence

A typical room temperature, $T = 300$ K, conductance and TEP measurement of a Ge/Si NW is shown in figure 2.5. A scanning electron microscope (SEM) image of a typical device is shown in the inset of figure 2.5a. For negative gate voltages the thermopower saturates to a constant value $\sim 120\mu V/K$. As this FET device turns off the thermopower begins to rise with a peak value of $\sim 350\mu V/K$. The lower panel in figure 2.5a shows the difference that instrument input impedance makes on measuring thermopower when the Fermi level is near or inside the gap of a semiconductor. For the DC measurement we used a SRS SR560 voltage amplifier (input impedance (Z_{DC}) is 0.1 GΩ), while for the AC measurement we used a SR830 lock-in amplifier (input impedance (Z_{AC}) is 0.01 GΩ) along with an Ithaco 1201 voltage preamplifer (Z_{AC} is 0.1 GΩ and 1 GΩ) in order to boost Z_{AC}. Experimentally, the ratio of X/Y components of the lock-in amplifier should be $< 5\%$ (this is analogous to minimizing the phase angle in a standard resistance measurement). When the resistance R, $R = 1/G$, of the nanowire is on the same order as the input impedance of the measurement instrument, the values of the thermopower become unreliable, meaning X/Y $\geq 20\%$. It can be seen that as Z_{AC} is increased the TEP values become more consistent with the DC TEP values, and do not simply drop to zero inside the gap.

In the degenerate regime, when the Fermi level is far away from a band edge, thermal equilibrium is established quickly on the timescale of measurement frequency. However, near the band edge very few carriers participate in transport and the conductance is exponentially suppressed. Thermopower rises when the Fermi level is in the gap, however, the absence of adequate equilibration between the electrodes limits accurate measurement. In order to increase thermoelectric efficiency both G and TEP have to be increased simultaneously, however, quite often the two parameters,

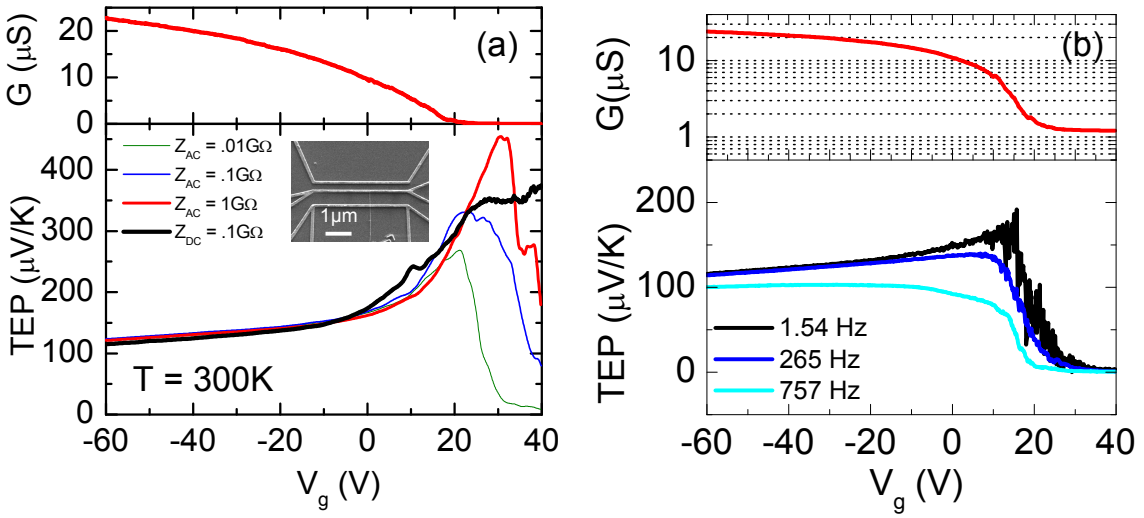

Figure 2.5: (a) P-type conductance and TEP values as a function of gate voltage for a 12 nm Ge/Si NW measured at T=300 K. The SEM image in the inset shows a typical device. The bottom panel shows TEP measured using the DC and AC methods using instruments with different input impedances. (b) Conductance and TEP for a different Ge/Si NW device. The lower panel shows the frequency dependence of the measured TEP.

as observed in our NWs, are inversely related [4].

It was found that the measured thermopower was independent of measurement frequency below 100Hz. For frequencies below 2Hz, the data becomes quite noisy (due to $1/f$ noise) and a slow sweep rate along with a long averaging time is required for accurate measurement. As the frequency is increased to a few hundred Hz the capacitive coupling (impedance of a capacitor is $Z_C = \frac{1}{j\omega C}$) between the electrical wires begins to change and the measured values are altered. The bottom panel of figure 2.5b shows how the measured TEP values change when a high measurement frequency is used. Now that we have fully explored all aspects of the TEP measurement technique, we will learn how to use it in order to acquire the carrier density inside semiconducting materials such as ZnO nanowires.

Chapter 3

Carrier density in semiconducting nanowires

Semiconducting materials have provided the basis for the technological and information revolutions of the 20th century. The ability to use the electric field effect (EFE) to modulate the carrier density by many orders of magnitude in Si enabled the modern integrated circuit [26]. Scaling of microelectronic components has lead to intense research into nanoscale materials, such as ZnO and Si nanowires, that are not simply patterned in the top-down lithographic approach. Chemical synthesis of nanowires for later self-assembly into nanowire arrays forms the basis of the alternative bottom-up approach to semiconductor technology fabrication. There has been considerable research effort into Si nanowires [31–35] as potential active channel replacement in future FET devices because of their compatibility with current complementary metal oxide semiconductor (CMOS) technology. Wide bandgap zinc oxide (direct band gap $\sim$ 3.3 eV) nanowires are used in the industry as UV blockers and have applications in optoelectronics [36, 37]. There are many other nanowire systems, but we focus on understanding the transport properties of the two mentioned systems. Parts of this chapter are published in [38] while other parts are written in a manuscript, Y. M. Zuev *et al.* [39].

A critical attribute of device channel characterization is the ability to measure the carrier density. It is often difficult to know the density of dopants incorporated in the

nanowires during the synthesis procedure [36, 40]. Typically for bulk materials, the carrier density is acquired using a Hall measurement, however, for the 1-dimensional cylindrical nanowire geometry the measurement is ineffective for two reasons. Lithographically it is very difficult to define a Hall bar with a separation of 5nm in order to make transverse contact to a small diameter nanowire. Also, since the nanowire is typically cylindrical and not rectangular in cross section, estimating the effective width of the channel is difficult. In this chapter, we present a method to estimate the carrier density in semiconducting nanowires by measuring the temperature dependence of the thermoelectric power. Section 3.1 will present the standard Hall measurement method. Section 3.2 will present conductance and thermopower measurements of Si nanowires. We will discuss the method to measure carrier density in semiconducting Si and ZnO nanowires using TEP measurements in section 3.3. An analysis of the carrier density in ZnO NWs acquired using the EFE method will be made in section 3.4.

3.1 Hall measurement

The Hall bar measurement is commonly used to measure magnetoresistance and carrier density in a material. The typical experimental setup is shown in figure 3.1. Qualitatively, as an electric field, E_x, is applied to the sample, a current, I, flows from the left to the right electrode. As a transverse magnetic field, $\vec{B} = B_z = B$, is applied to the sample the Lorentz force bends the electrons down, creating a buildup of negative charge at the bottom of the sample and positive charge at the top. This buildup of charge induces a transverse electric field, E_y, to counteract the effect. The equilibrium transverse voltage, V_{Hall}, is proportional to the carrier density in the sample.

In order to understand this effect in detail we use the Drude model to derive the Hall coefficient [1]. Starting from the equations of motion:

$$\left(\frac{d}{dt} + \frac{1}{\tau}\right)\vec{p} = -e\left(\vec{E} + \frac{\vec{p}}{m} \times \vec{B}\right) \tag{3.1}$$

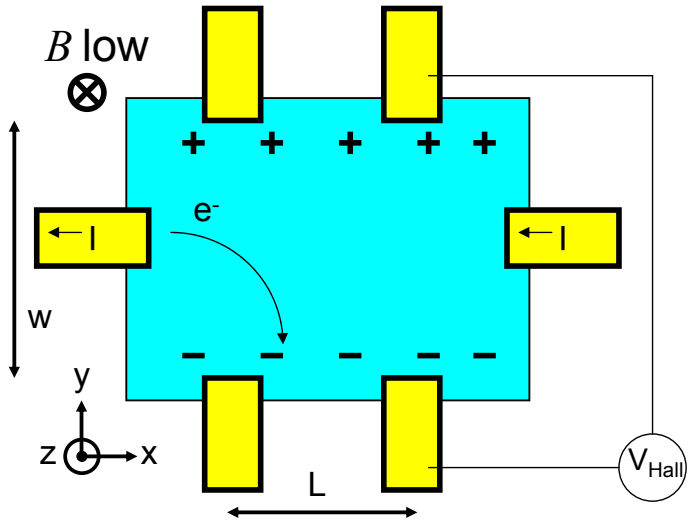

Figure 3.1: Diagram of a typical Hall bar configuration used to measure the carrier density of a material. Electrical leads are shown in yellow and the material is shown in blue.

where $\vec{p}$ is the momentum of an electron, τ is the scattering time, e is the charge of an electron, and m is the mass of an electron. We are interested in the $\vec{y}$ components in order to obtain the transverse field. We use $\vec{p} = m\vec{v}$ where $\vec{v}$ is the velocity of the electron.

$$\left(\frac{d}{dt} + \frac{1}{\tau}\right) mv_y = -e\left(E_y + v_x B\right) \tag{3.2}$$

In equilibrium, there is no motion of carriers in the $\vec{y}$ direction, so $v_y = 0$. We rearrange equation 3.2 and use $j_x = -nev_x$, where j_x is the current density in the $\vec{x}$ direction and n is the carrier density, to get:

$$E_y = \frac{-B}{ne} j_x \tag{3.3}$$

The Hall coefficient is defined as the ratio of transverse electric field to the longitudinal current density and transverse magnetic field, $R_H = \frac{E_y}{Bj_x} = -\frac{1}{ne}$, and is dependent on the carrier density. Plugging in the definition of the current density, $j_x = \frac{I}{Wd}$ where

W is the width of the sample and d is its thickness, to equation 3.4 we have

$$V_{\text{Hall}} = \frac{B}{ned} I \tag{3.4}$$

By measuring the slope of the resistance as a function of magnetic field, the carrier density of a material is acquired. The geometric constraints of small diameter cylindrical nanowires limit the use of this technique to evaluate the carrier density in these materials.

3.2 Conductance and TEP in semiconducting Si nanowires

We now turn our attention to the measurements of the basic transport properties of Si nanowires. The mesoscopic measurement technique described in the previous chapter is used to measure the conductance and thermoelectric power in Si nanowires as a function of temperature and gate voltage. Silicon nanowires in the diameter range of 20±5nm were synthesized using the VLS method in collaboration with the Lieber group at Harvard. Silane (SiH_4) gas was used as the vapor phase reactant and 10nm Au nanoparticles were used as the catalyst in the reaction [31, 34]. Diborane (B_2H_6) gas was used to dope the nanowires during the growth procedure with a nominal Si:B ratio of 8000:1. The nanowire TEP devices with 2/40 nm Ti/Pd electrodes were fabricated with standard electron beam lithography techniques. A brief 5 second HF dip was performed on nanowire device samples immediately prior to metallization in order to remove the native oxide.

The gate dependence of the conductance of a typical Si NW is shown in Figure 3.2a in the temperature range of 80 - 300 K [41]. The device behaves as a FET and is in the "on" regime for higher negative gate voltages. The model that best describes the conductance is Schottky barrier mediated transport (the lower inset in Figure 3.2b depicts the energy band diagram of the system). The height, E_{SD}, of the Schottky barrier that forms between the Si NW and the metal electrode interface is adjusted by the applied gate voltage. In the subthreshold regime, the conductance is drastically

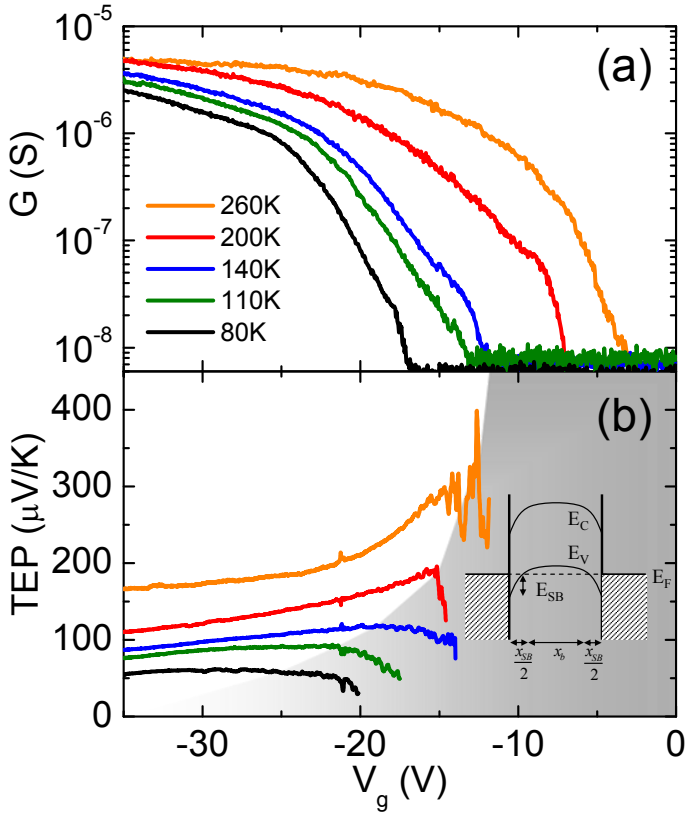

Figure 3.2: Conductance (a) and thermopower (b) of a 20 nm Si nanowire plotted as a function of gate voltage at (top to bottom) 260 K, 200 K, 140 K, 110 K, and 80 K. The shaded grey region in (b) is where the FET is "off" and the measured TEP values are not reliable. The lower inset of (b) shows an energy band diagram of the formation of a Schottky barrier in the Si NW - electrode system.

decreasing but still finite. The FET will be turned "off" at positive V_g where the Schottky barriers deplete all available itinerant states in the valence band.

The TEP of the device is plotted as a function of gate voltage in figure 3.2b. The total TEP measured is the sum of the contribution coming from the bulk of the nanowire as well as from the Schottky barrier. At higher negative gate voltages, the Schottky barrier becomes very thin and contributes negligibly to the total TEP. In this "on" regime, the TEP signal represents the intrinsic thermopower value of the nanowire and decreases slightly for decreasing gate voltages. The temperature dependence of TEP can be used to approximate the carrier density in the nanowires.

3.3 Measuring carrier density using TEP in Si and ZnO NWs

The temperature dependent TEP data of Si and ZnO nanowires is analyzed using semiclassical formalism in order to learn more about the basic properties of the nanowire systems. Figure 3.3a shows the TEP of Si nanowires plotted as a function of temperature in the range of 80K $< T <$ 300K measured at a single gate voltage point for several samples represented by the different color markers. We fit the data from all of the samples, which roughly falls along a straight line, to extract the slope of $dS/dT = .67\mu\text{V/K}^2$. The TEP is positive which indicates that the dominant charge carriers are holes, which is appropriate for our B doped nanowires.

Zinc oxide nanowires in the 80 nm to 120 nm diameter range were synthesized using a catalyst-free metal-organic vapor-phase epitaxy (MOVPE) [42] in collaboration with the Yi group at POSTECH University in Korea. Ohmic contact to the wires was made by a CF_4/O_2 plasma etching step prior to metallization in order to minimize the Schottky barrier between the nanowire and the 80/100nm Ti/Au electrodes. Figure 3.3b shows TEP measurements of ZnO nanowires as a function of tempera-

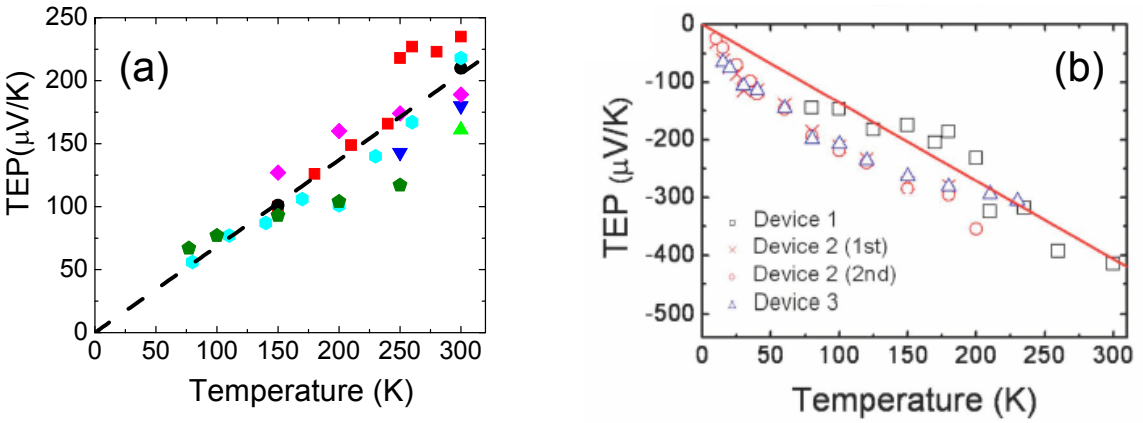

Figure 3.3: (a) Temperature dependence of the TEP of Si nanowires taken from several samples. (b) Temperature dependence of the TEP of ZnO nanowires. The slope of the linear fits is used to estimate the carrier density in the nanowires.

ture for three samples. The peak value at room temperature is -400μV/K and the dominant charge carriers are electrons. We again fit the data in order to extract the

linear slope of -1.36μV/K^2.

Since the TEP is linear as a function of temperature, we attribute the thermoelectric response to diffusive thermoelectric generation and use the Mott relation, equation 1.18, to derive the carrier density in the nanowires [43, 44]. We assume a parabolic energy band dispersion in each material

$$E_F = \frac{\hbar^2 k_F^2}{2m^*} \tag{3.5}$$

with the bulk effective mass m^* and Plank's constant $\hbar$. We assume a 3D density of states (DOS) for our nanowire materials written in terms of carrier density, n:

$$E_F = \frac{(3\pi^2)^{2/3}\hbar^2}{2m^*} n^{2/3} \tag{3.6}$$

We use the Drude conductivity $\sigma = \frac{n(E)e^2\tau}{m^*}$ to rewrite equation 1.18 in the following form:

$$\frac{S}{T} = -\frac{\pi^2 k_B^2 m^*}{(3\pi^2)^{2/3}\hbar^2 e} \frac{1}{n^{2/3}} \tag{3.7}$$

A bulk effective mass of $m^* = .39m_e$ for Si [35] and $m^* = .28m_e$ for ZnO [45] is used to calculate the carrier density from the TEP measurements of $1.4\times10^{19}/cm^3$ and $3.1\times10^{18}/cm^3$ for each material, respectively. For nominal boron doping in Si NWs the density would be $9\times10^{20}/cm^3$, however, considering that not all of the B is converted into singly ionized impurities, the density acquired with our method is reasonable.

It is noted that both Si and ZnO nanowires are highly doped and that the temperature dependence of the TEP is linear, even though both bulk materials have a large phonon-drag component contributing to the total thermoelectric signal [5, 46]. The phonon-drag component would manifest as a non-linear temperature dependence of the TEP. The phonon-drag term is not observed in our nanowires most likely because the phonon thermal current is suppressed. Both surface specular phonon scattering in the nanowire and ionized impurity scattering due to the high doping level significantly limit phonon conduction. Since lightly doped bulk silicon has a large phonon-drag

TEP component (see figure 1.2), in future experiments, it would be interesting to identify the reduction of the thermal current by looking at the linearity of the TEP temperature dependence for a range of Si nanowire diameters and doping levels in a future study.

3.4 ZnO nanowire field effect carrier density

In this section, we compare the carrier density of ZnO nanowires acquired using the TEP technique to the value that is predicted by the EFE method. Using basic electrostatics calculations the induced charge density can be estimated from the gate dependence of the conductance. In order to make this calculation we employ the method of images and make the assumption that the nanowire is surrounded by a material that has an effective dielectric constant of the average between the oxide layer and the vacuum layer. Figure 3.4a shows a diagram of the cylinder-on-plane model used to derive the capacitance per unit length between the nanowire and the gate [27], $C_L = \frac{2\pi\varepsilon\varepsilon_0}{\cosh^{-1}(h/r)}$, where ε is the relative dielectric constant of the oxide layer, h is the oxide thickness, and r is the nanowire radius. In many cases the $r \ll h$ limit is satisfied, so the result is simplified to

$$C_L = \frac{2\pi\varepsilon\varepsilon_0}{\ln(2h/r)} \tag{3.8}$$

For an SiO_2 thickness of 500 nm and a nanowire diameter of 120 nm, the capacitive coupling per unit length is C_L=43 pF/m. Continuing the derivation of the cylindrical capacitor on a plane, we can acquire the density from the following relationship:

$$n = \frac{C_L(V_g - V_T)}{e\pi r^2} \tag{3.9}$$

Here V_g is the applied gate voltage and V_T is the threshold voltage where a semiconductor transistor device turns off. This method has several shortcomings. Due to electric field screening effects, the gate capacitive coupling term in equation 3.8 does not represent the true capacitance of the nanowire and gate electrode system. Also,

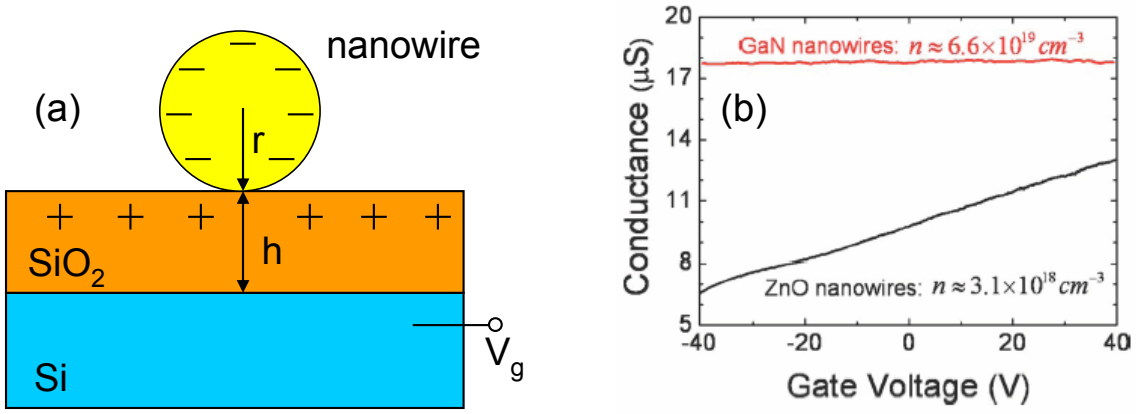

Figure 3.4: (a) Diagram of the cylinder-on-plane model used to determine the capacitive coupling between the nanowire and the gate. (b) Gate dependence of the conductance of ZnO nanowires.

there are numerous surface charge traps in the amorphous dielectric layer which lowers the induced carrier density value in a nanowire [47]. It is often difficult to induce enough charge with the gate in order to modulate the conductivity of highly doped semiconducting nanowires. As a result of this limitation the value of V_T is not always well defined. The gate voltage can be increased only as long as the electric field is below the dielectric breakdown limit.

In figure 3.4b, the conductance of ZnO nanowires is plotted as a function of gate voltage that is applied to the degenerately doped Si substrate. The threshold voltage was not observed but is extrapolated to be -130 V. The carrier density calculated using the EFE method is $5.7\times10^{18}/cm^3$ in ZnO nanowires. The EFE method predicts a larger carrier density than the TEP method most likely due to the existence of surface charge trap states. The high level of n-type doping in ZnO nanowires is presumably due to the incorporation of hydrogen during the growth process. Improvements to the experiment can be done by depositing a conformal dielectric material around the nanowires thereby enhancing the capacitive coupling. This would improve the accuracy of the EFE method, further validating the TEP technique of carrier density acquisition.

3.5 Summary

It been shown that temperature dependent TEP measurements can be used to acquire the carrier density of semiconducting nanowires where other methods such as the Hall measurement and EFE measurement do not provide accurate results. We have measured the carrier density of Si and ZnO nanowire systems using this method. The TEP measurement technique can be used to accurately determine the carrier density in nanowire systems in order to characterize synthesis parameters and nanowire FET devices.

Chapter 4

Diameter dependence of the transport coefficients in chalcogenide nanowires

Chalcogenide materials are compounds that contain elements in group 16 of the periodic table. Chalcogens, semimetals, and small bandgap semiconductors are often used in thermoelectric applications because of their high electrical performance and low thermal conductivity [8]. It is interesting to experimentally investigate how the transport coefficients are altered when the diameter of the material is decreased. Even though Bi is not a chalcogenide material, we start this chapter by discussing Bi nanowires because they have many similar properties to the chalcogenide antimony telluride and because their transport properties as a function of nanowire diameter have been studied extensively theoretically. Bismuth nanowires have attracted attention because several predictions have been made about the enhancement of ZT in this material as a function of decreasing diameter [19, 20]. The majority of experiments performed on Bi nanowires have used porous anodic alumina templates which measure many nanowires at the same time [48–51]. We have performed experiments on individual Bi nanowires using our mesoscopic measurement technique in order to investigate the semimetal-semiconductor transition predicted to occur in this material (section 4.1). We want to understand to what degree the electronic part of ZT, the power factor $S^2\sigma$, is enhanced as the nanowire diameter is decreased. We investigate how the power factor of antimony telluride (Sb_2Te_3) NWs scales as a function

of nanowire diameter. Section 4.2 will talk about basic properties of bulk Sb_2Te_3, the nanowire synthesis method, as well as TEP device fabrication details. We will discuss diameter dependence of the Sb_2Te_3 resistivity and TEP in sections 4.4. Section 4.5 will cover the temperature dependence of the transport coefficients. Lastly, we will investigate magnetoresistance properties of Sb_2Te_3 nanowires to try to uncover signatures of the topological insulator nature of this material in section 4.6.

4.1 Bismuth nanowires

Bulk bismuth is a semimetal with the top of the valence band above the bottom of the conduction band. Since it is a semimetal, the electrical resistivity, $\rho = 1.07$ $\mu\Omega m$, is higher than that of a typical metal [1]. Its Fermi surface is highly anisotropic and contains ellipsoidal electron and hole pockets. The high atomic mass of Bi, 209 amu, results in effective phonon scattering and a low thermal conductivity, $\kappa = 8$ W/Km . These characteristics make Bi very attractive for thermoelectric applications. However, experimentally Bi is very difficult to handle because it has a very low melting temperature, 272°C. Bismuth has a rhombohedral lattice structure, with the binary, bisectrix, and trigonal taken as the primary axes of symmetry. Bi nanowires have the same crystalline structure as bulk Bi, but quantum confinement effects alter the electronic structure.

4.1.1 Theoretical predictions

A theoretical investigation of the transport properties of Bi nanowires has shown enhancement of ZT along certain crystallographic orientations [19, 20]. The electronic structure of the nanowire system was modelled with the assumption that electrons were confined in a cylindrical potential. Using the $\vec{k} \cdot \vec{p}$ approximation for L-point electrons the anisotropic effective mass tensor is calculated numerically. The semiclassical Boltzmann formalism is then used to calculate the transport coefficients for

wires of different diameters. The position of the energy subbands is plotted as a function of nanowire diameter in figure 4.1a[1]. For large nanowire diameters, the band structure approaches that of semimetallic bulk Bi with a band overlap of 38 meV at 77 K. The calculations show that as the nanowire diameter decreases, a semimetal to

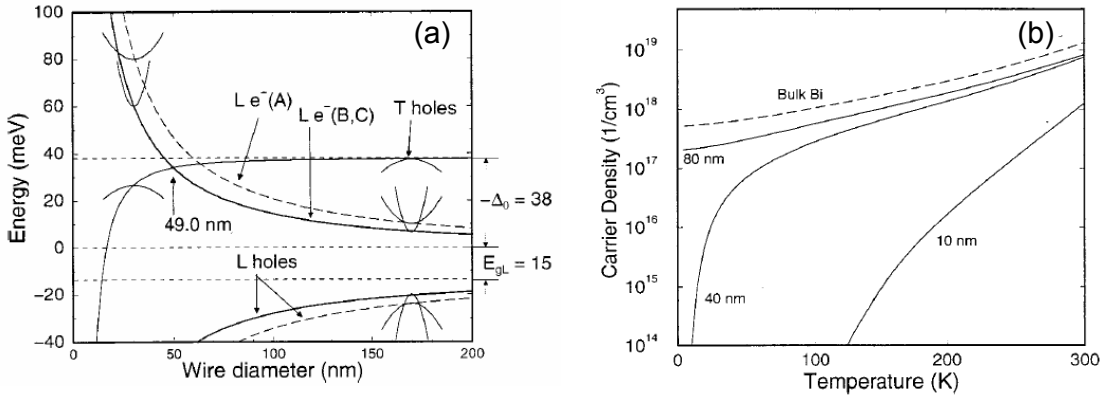

Figure 4.1: (a) Energy band structurer for Bi NWs at 77 K oriented in the $[01\bar{1}2]$ direction. (b) Carrier concentration as a function of temperature in Bi NWs for several nanowire diameters. Both (a) and (b) were reproduced from [19] with permission.

semiconductor transition occurs and a band gap opens up. This can be seen in figure 4.1a as the conduction subband moves up and the valence subband moves down. For a nanowire with axis in the $[01\bar{1}2]$ direction at $T = 77$ K the critical diameter is $d_c = 49$ nm. For nanowires with different orientations the critical diameter at $T = 77$ K can be in the range of 40 nm $< d_c <$ 57 nm [19].

The total carrier density at the energy level where the number of electrons equal the number of holes is plotted as a function of temperature in figure 4.1b for nanowires with different diameters. It can be seen that the temperature dependence of the carrier density of the large diameter 80 nm nanowire is similar to that of bulk semimetallic Bi. The smaller diameter 10nm nanowire is semiconducting in the entire temperature range, so that its carrier density rises exponentially as a function of temperature. The 40nm nanowire undergoes a semimetal-semiconductor transition around $T =$

[1]Reprinted figure 2 and 4 with permission from Y. Lin, X. Sun, and M. S. Dresselhaus, Physical Review B 62, 4610 (2000) © 2000 by the American Physical Society.

170 K, so that below $T = 170$ K the nanowire exhibits semiconducting behavior [19]. The resistance of an intrinsic semiconductor should rise exponentially as a function of decreasing temperature. Therefore the experimental signature of a semimetal-semiconductor transition in a small diameter Bi nanowire should be a significant increase in resistance below a certain temperature.

4.1.2 Experimental values

We have performed transport experiments on single crystal Bi nanowires that were synthesized in collaboration with the Lee group at Yonsei University in Korea [52, 53]. Nanowires were dispersed from ethanol solution onto a SiO_2 substrate with prepatterned alignment marks. The diameters of the nanowires were in the range of 30 nm - 50 nm which was confirmed with an atomic force microscope (AFM). Ohmic contact to the nanowires was made using an Ar plasma etching procedure before the metallization step in order to remove the native oxide. An etching rate of ∼1nm/second was achieved in our Oxford ICP etching system with the plasma "Forward Power" = 70 W. We used 4-terminal resistance measurements in order to acquire the intrinsic properties of the nanowires as a function of gate voltage, temperature, and magnetic field.

At room temperature, no gate voltage dependence is observed which means that the carrier density in the nanowire is much higher than what can be induced by the capacitively coupled gate. At low temperature below $T = 30$ K, we observe quasi-periodic oscillations in the conductance that are less than 2% of the main conductance signal. Such Universal Conductance Oscillations (UCF) are expected in sufficiently clean mesoscopic samples with small diameter and channel lengths at low temperatures (diameter = ∼40 nm and length = 1 μm for our NWs). Figure 4.2a shows the temperature dependence of the normalized 4-terminal resistance for several different nanowire diameters. Very weak temperature variation is observed for all 4 nanowires studied, less than 30% change from the room temperature value. Even though the 2 samples, d = 33 nm and d = 39 nm, have a diameter smaller than the theoretically predicted critical diameter, the nanowires do not show strong semiconducting

behavior.

There could be several explanations of why we do not observe the semimetal-semiconductor transition in our Bi nanowires in the diameter range studied. Due to several fabrication processing steps and the fact that Bi is thermodynamically unstable the nanowires could have become polycrystalline which would alter the transport properties. However, this might be unlikely because the room temperature resistivity in our 33nm nanowires is still quite low, $\rho \approx 3.5\ \mu\Omega m$, which would signify crystallinity. Nominally, the nanowire axis is in the [001] direction, however, the actual

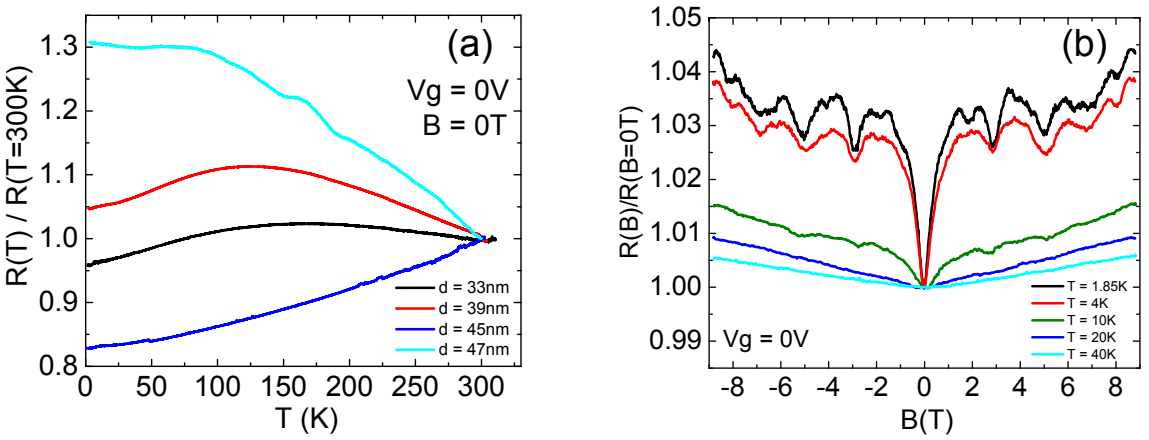

Figure 4.2: (a) Normalized 4-terminal resistance of individual single crystal Bi nanowires as a function of temperature for several nanowire diameters. (b) Magnetoresistance measurements as a function of temperature for a 33 nm Bi NW. At low temperatures a weak antilocalization peak along with UCF oscillations can be observed.

orientation could be in a different direction. Since d_c is orientation dependent, perhaps our nanowires have an orientation that has a smaller critical diameter, $d_c <$ 33 nm. Nanowire characterization with TEM should be performed in order to verify the crystallinity and orientation of the nanowires studied. The Fermi level of the nanowire could be far away from the band overlap region, where the bandgap is predicted to open, due to high doping levels. This would also correlate with the fact that there was no gate dependence in our Bi nanowire devices. Lastly, its also possible that the assumptions of the theory described above did not capture the intrinsic band

structure of small diameter Bi nanowires.

We have studied magnetoresistance effects in Bi nanowires under the influence of a magnetic field applied perpendicular to the nanowire axis. Figure 4.2b shows normalized magnetoresistance data taken on the 33nm Bi nanowire as a function of temperature. At low temperatures a weak antilocalization peak can be observed near $B = 0$ T, which is common for heavier elements like Bi [54]. Oscillation as a function of magnetic field are most likely not Shubnikov de Haas oscillations because they are not periodic in $1/B$. When a small gate voltage is applied, the period of the oscillations changes significantly which indicates that a slight perturbation of the carrier density will change the interference pattern. We attribute this behavior to the presence of UCF oscillations. The TEP was also measured in a 46 nm Bi nanowire with a low room temperature value of -22 μV/K. In future studies, it would be interesting to measure the temperature dependence of the resistivity and the TEP of smaller diameter nanowires down to 5 nm.

Experimentally, it does not appear that the electronic contribution to the ZT is particularly enhanced in small diameter Bi nanowires. Most likely the ZT enhancement in the theory was due to a decrease of the thermal conductivity as a result of diameter reduction, similar to the experimental observations in Si nanowires [12, 13]. The next section investigates the diameter dependence of the transport properties of the chalcogenide material antimony telluride.

4.2 Antimony telluride

In order to interpret our Sb_2Te_3 nanowire results, we must first understand the basic properties of the bulk material. Antimony telluride is a small bandgap semiconductor with a gap of 0.28 eV [24, 55], although several recent calculations [56, 57] predict that the gap is closer to ~ 0.1 eV. Due to antistructural defects in the rhombohedral crystal structure, Sb_2Te_3 is generally p-type with the Fermi level deep in the double valence band. The Fermi surface consists of six ellipsoidal hole pockets tilted to the basal plane [58]. Chalcogenides are part of a class of phase changing materials which

can undergo a reversible transition from amorphous to crystalline structure with an accompanying change in resistance by several orders of magnitude. These materials are considered as candidates in phase changing memory because of fast access times and low power consumption [59]. The room temperature transport coefficients [24, 60, 61] (electrical resistivity, $\rho = 250\ \mu\Omega cm$, thermopower, S = 90 μV/K, and thermal conductivity, $\kappa = 5$ W/Km) combine to make a ZT = 0.2. It is calculated that when uniaxial stress is applied perpendicular to the layered antimony telluride structure the power factor is significantly enhanced [55]. It is common to alloy Sb_2Te_3 with Bi_2Te_3 and other compounds containing Pb, Bi, Te, and Sn, in order to improve thermoelectric performance in the bulk [16, 61, 62]. We investigate how nanowire diameter influences the electronic contribution to the thermoelectric figure of merit in single crystal chalcogenide Sb_2Te_3 nanowires. The rest of this chapter will describe work from Y. M. Zuev *et al.* [63].

Antimony telluride is also known to be a topological insulator with a bulk energy gap and topologically protected surface states [56, 57]. It has been reported [57] that the application of a magnetic field parallel to the topologically insulating nanowires (Bi_2Se_3 NWs) produces Aharonov-Bohm oscillations in the magnetoresistance which stems from the surface states. Although the surface states of Sb_2Te_3 are more difficult to access than those in Bi_2Se_3 due to the smaller energy gap, we nevertheless investigate both parallel and perpendicular magnetoresistance effects, thereby testing the possibility of observing galvanomagnetic quantum interference effects in Sb_2Te_3.

4.3 Nanowire synthesis and device fabrication

Single crystal Sb_2Te_3 nanowire samples were synthesized by the Park group at Harvard using the vapor-liquid-solid method described in [64]. Gold nanoparticles were used to catalyze the growth of the nanowires starting from commercially bought Sb and Te powders. The crystallographic orientation of the nanowire axis was measured to be in the [110] direction with TEM. Energy-dispersive X-ray (EDX) spectroscopy was performed in order to ensure that the atomic ratio of Sb to Te was constant

throughout the nanowires (see figure S1 in the Supporting Information section in reference [63]). The resistance of the nanowires was varied by several orders of magnitude by the application of voltage pulses displaying the phase changing nature of this material [64]. An SEM image of a typical Si/SiO_2 growth substrates is shown in figure 4.3a. Many faceted single crystal Sb_2Te_3 platelets can be seen along with a nanowire in the center of the image. The inset of figure 4.3a shows a TEM image of a typical nanowire showing good crystallinity and the lack of native oxide on the surface.

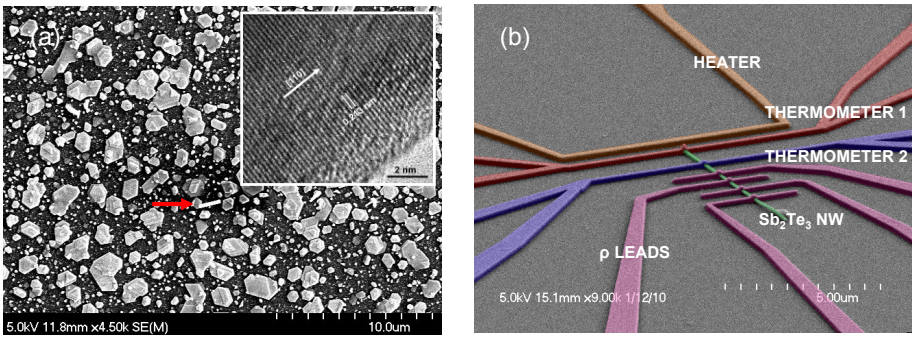

Figure 4.3: (a) SEM image of the growth substrate containing faceted single crystal Sb_2Te_3 platelets and a nanowire (red arrow). The inset shows a TEM image of a typical nanowire. (b) A false color tilted SEM image of a typical nanowire (green) TEP device.

A target 950 nm SiO_2/Si substrate is first cleaned with the "piranha" solution (3:1 sulfuric acid:hydrogen peroxide) in order to remove all organics and contaminating compounds. Patterns are written on the wafer using electron beam (e-beam) lithography (FEI e-beam writer). We use a 950 K molecular weight polymethyl methacrylate (PMMA) A5 positive resist, which is formulated in anisole, as the masking layer. The resist is spun on to the substrate using a commercial spinner at 4000 rpm for 45 seconds. A soft bake is performed after the spin on a hot plate at 180°C for 2 minutes in order to remove the remaining solvent. After the e-beam writing the sample is developed in 3:1 isopropyl alcohol:methyl isobutyl ketone (MIBK) solution for 2 minutes. The metallization is done with either a Edwards thermal evaporator or a Semicore e-beam evaporator. Titanium or chromium is used as a sticking layer

between the SiO_2 and the main metal material. In order to dissolve the PMMA mask and liftoff the metal layer, the sample is kept in acetone for 10 or more hours at room temperature. Alignment marks using 2/50 nm of Cr/Au are patterned on the target substrate in order to be able to image the nanowire locations in an optical microscope.

Substrates containing nanowires were mildly sonicated in isopropyl alcohol solution and deposited onto a pre-patterned wafer using a microliter pipette. A subsequent nitrogen blow drying evaporates the solvent and leaves only nanowires on the surface. Alternatively, the nanowire solution can be spun onto the target substrate using the spinner. The nanowires can also be transferred from the growth substrate to the target substrate by a polydimethylsiloxane (PDMS) stamp. The quantity of nanowires transferred using this method is considerably larger, however, it is not clear if the if the PDMS leaves a residue on the target substrate because the metal electrodes did not stick to the surface after a subsequent metallization step. The nanowires on the target substrates were imaged with respect to alignment marks using a Nikon confocal microscope in dark field mode for better contrast resolution.

Ohmic contact to the NWs was made with a subsequent e-beam lithography step followed by an evaporation of Ti/Ni (2/200 nm) and a lift-off procedure. It is important to align the TEP device pattern so that there is no electrical connection between the heater and the near electrodes. No etching step was required prior to metal evaporation to make ohmic contact. AFM was used to measure the NW diameter with accuracy to within 1 nm. The carrier density inside the nanowires was adjusted by applying a gate voltage (V_g) to the degenerately doped Si substrate. Figure 4.3b shows a false colored tilted SEM image of a typical finished Sb_2Te_3 TEP device. The purple electrodes are used to measure the intrinsic resistivity in the 4-terminal geometry.

4.4 Diameter dependence

Because the diameter distribution of Sb_2Te_3 nanowires is much larger than that of other nanowire materials studied in earlier chapters, we are able to investigate how

nanowire transport properties scale with diameter. A histogram of the diameter distribution of nanowires found on the target substrates is shown in the inset of figure 4.4a, with a peak around 75nm. Figure 4.4 shows the electronic and thermoelectric proper-

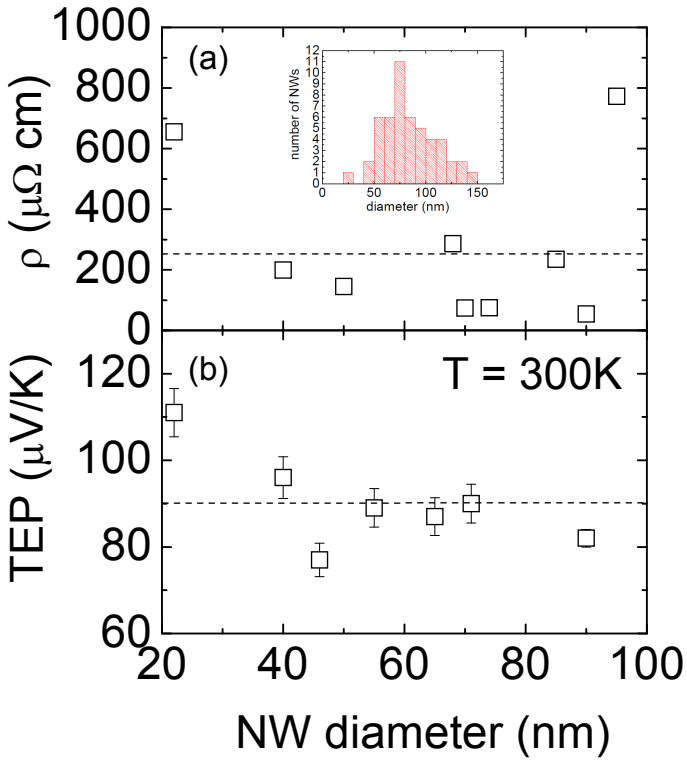

Figure 4.4: (a) Resistivity as a function of Sb_2Te_3 nanowire diameter. The inset shows a histogram of the diameter distribution of nanowires found on target substrates. (b) TEP as a function of nanowire diameter, showing enhancement in smaller diameter nanowires. The dashed lines in (a) and (b) are bulk values taken from [24, 60, 61].

ties of the nanowires measured at room temperature, as a function of NW diameter. Bulk values [24, 60, 61] for Sb_2Te_3 resistivity $\rho = 250$ $\mu\Omega$cm and TEP $= 90$ μV/K are plotted as dashed lines in figure 4.4a,b, respectively. Error in the resistivity measurement is less than the data points plotted. The typical resistivity for Sb_2Te_3 NWs is comparable to the bulk value and does not exhibit strong diameter dependence. Since the resistivity depends on the carrier density as well as on the scattering time, without an independent measure of the carrier density it is difficult to understand

the trend in resistivity. Figure 4.4b shows that the thermoelectric power is enhanced in smaller diameter NWs. TEP of a 22 nm NW is measured to be 111 μV/K while that of a 95 nm NW is 81 μV/K, indicating more than 30% TEP enhancement in the smallest NWs we measured. Error in the TEP is the result of error during the calibration measurement and is typically $\sim 5\%$. The enhancement of TEP in smaller diameter wires could be a result of an increase in the doping level or a change of the band structure and correspondingly the position of the Fermi energy due to quantum size effects. It is difficult to fabricate devices out of nanowires with diameters < 20 nm because they tend to be shorter than the required 1 μm channel length, are less structurally stable during the sonication step when the nanowires are transferred to the target substrate, and making Ohmic contact is challenging. However, it would be very interesting to study if the observed trend in TEP enhancement would continue in smaller diameter nanowires.

4.5 Temperature dependence

The temperature dependence of the resistivity and TEP exhibits clear changes in the transport behavior as a function of NW diameter. Figure 4.5a shows the normalized four-terminal resistance plotted as a function of temperature on a semilog plot from $T = 300$ K to $T = 5$ K. Error bars are taken as the standard deviation of consecutive measurements and are smaller than the data markers where they are not seen. Between 300 K and $\sim$50 K the resistance decreases linearly as a function of decreasing temperature due to a decreasing phonon population, similar to bulk metals [1]. Below $\sim$50 K, NWs with diameters larger than 45 nm exhibit resistance saturation because the scattering is dominated by boundary and impurity scattering. For NWs smaller than 45 nm the resistance increases to several times the room temperature value. We note that there are some sample to sample variations due to mesoscopic fluctuations of the defect arrangement. The exact nature of this low temperature non-metallic behavior of small diameter NWs is not clear presently. We note, however, that Sb_2Te_3 can undergo reversible phase change between an amorphous and a crystalline phase

by the application of a voltage pulse [64]. For small diameter NWs it was often necessary to anneal the devices by flowing large current in order to improve the overall conductance (figure 4.5a inset). One potential scenario for resistance increase is that some small number of amorphous grain boundaries remain in small diameter NWs and contribute to resistance increase at low temperature. If one grain became highly resistive at low temperatures, the overall resistance of the nanowire will become high.

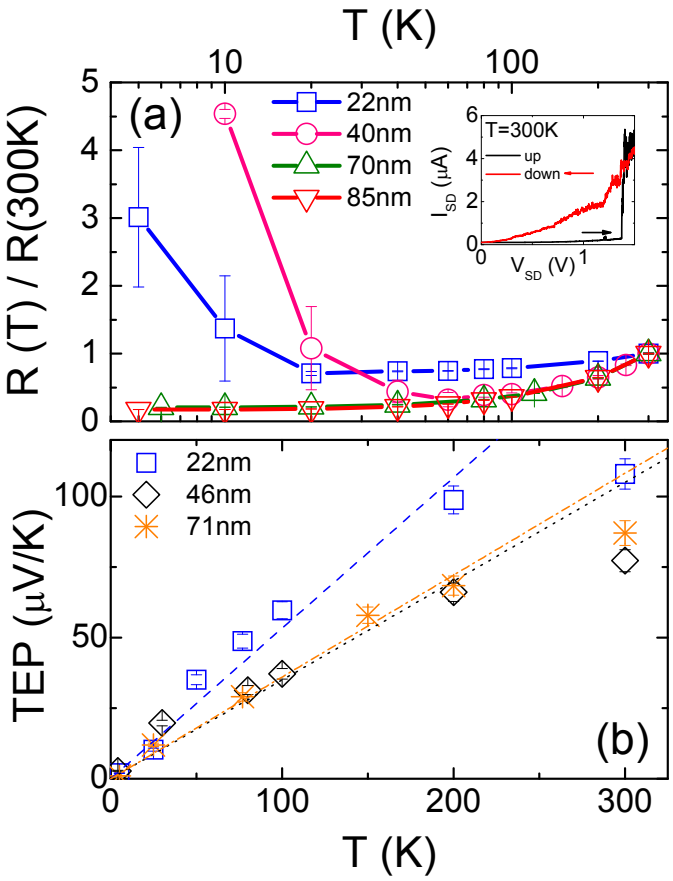

Figure 4.5: (a) Normalized 4-terminal resistance and (b) thermopower as a function of temperature for several NWs. The same 22 nm diameter NW is seen in (a) as in (b). The inset in (a) shows the current versus bias voltage characteristics before and after crystallization of the 22 nm NW by application of a high bias. The linear fits in (b) correspond to diffusive thermopower generation, and are discussed in the text.

We now turn our attention to the temperature dependence of TEP. For all NWs

we measured, the profile of the TEP is linear to sublinear as a function of temperature (figure 4.5b). The semiclassical Mott relation for diffusive thermopower is given by equation 1.18 and predicts a linear temperature dependence for the TEP. Consequently, the positive linear temperature dependence below $T = 200$ K in Sb_2Te_3 NWs signifies hole dominant diffusive thermoelectric generation. Similar to the derivation in the previous chapter, the slope of the linear fit can be used to extract the carrier density in the nanowires [38, 39, 44]. Provided that bulk hole effective mass [24] of $m^* = 0.78m_e$ (m_e is the electron rest mass) can still be used for holes in nanowires, we estimate a hole carrier density on the order of 10^{20} cm^{-3} in our 70nm nanowires and a corresponding mobility of $\sim$800 cm^2/Vs. This carrier density values are comparable to values published for bulk Sb_2Te_3 [24, 58, 65]. The carrier density decreases linearly as a function of decreasing diameter, and is smaller by a factor of 2 or so in the 22 nm diameter NWs. It is possible that the decreasing TEP is the result of the decreasing dopant density in the smaller diameter nanowires. It is noted that the measured TEP values at $T = 300$ K are identical before and after the recrystallization process, even thought the resistance changes by two orders of magnitude. In a bulk sample a Hall measurement can be used to determine the carrier density. In nanowires, however, such a measurement cannot be performed due to their 1-dimensionality. This leads us into our discussion of magnetoresistance of the nanowires.

4.6 Magnetoresistance measurements

Antimony telluride has a non-spherical Fermi surface consisting of 6 ellipsoids tilted at an angle to the basal plane, where two valence bands, upper and lower, are responsible for conduction [24, 58]. The dependence of the perpendicular magnetoresistance up to $B = \pm 10$ T of a 70 nm NW is parabolic at all temperatures (figure 4.6a). In order to understand the magnetoresistance behavior, we must understand how the many band model works. The total electric current, $\vec{J}$, is the sum of contributions from several bands, $\vec{J_n} = \hat{\rho}^{-1}\vec{E}$, due to an applied electric field, $\vec{E}$, so that we have

$\vec{J} = \sum_n \vec{J}_n = \sum_n \hat{\rho}_n^{-1} \vec{E}$. If we consider the resistivity tensor of one band, given by

$$\hat{\rho}_1 = \begin{pmatrix} \rho_1 & -R_1 B \\ R_1 B & \rho_1 \end{pmatrix} \tag{4.1}$$

and restrict ourselves to the simplest case of two bands, the total magnetoresistance,

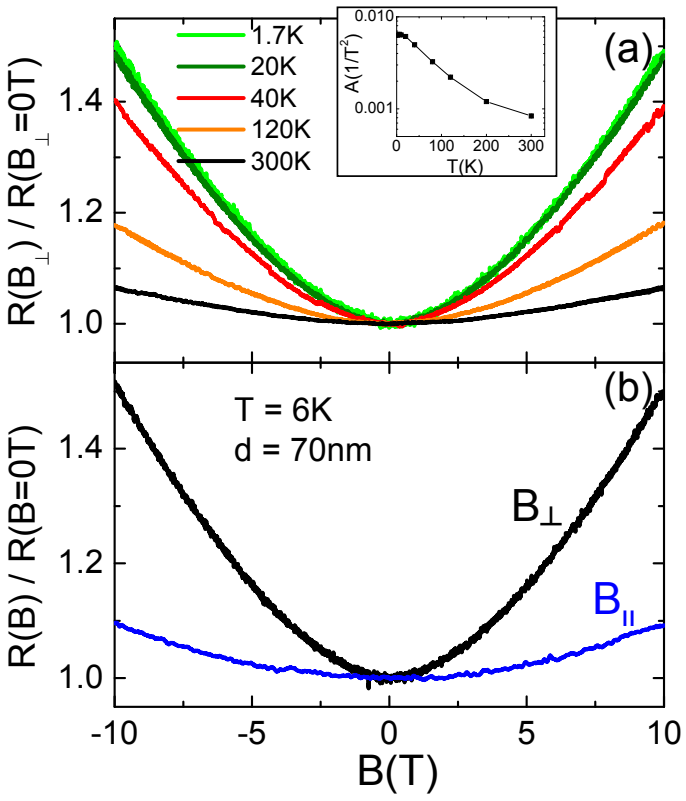

Figure 4.6: (a) Temperature dependence of normalized magnetoresistance in a perpendicular magnetic field of a 70 nm diameter NW. The parabolic behavior is attributed to the contribution of holes from two valence bands to the magnetoresistance. The inset shows the decrease of the curvature as the temperature increases. (b) Comparison of the magnetoresistance for a magnetic field applied parallel and perpendicular to the NW [110] axis at $T = 6$ K.

$\rho(B)$, will be given by:

$$\rho(B) = \frac{\rho_1\rho_2(\rho_1+\rho_2) + (\rho_1 R_2^2 + \rho_2 R_1^2)B^2}{(\rho_1+\rho_2)^2 + (R_1+R_2)^2B^2} \tag{4.2}$$

where $\rho_{1,2}$ and $R_{1,2}$ are the magnetoresistance and Hall coefficients of each band, respectively, and B is the magnetic field. The second term in the denominator of equation 4.2 will tend to zero if the bands are compensated or if the first term in the denominator is much bigger than the second. In those cases, we can therefore simplify equation 4.2 to the following compact form:

$$\rho(B) = \rho_{B=0}(1 + AB^2) \tag{4.3}$$

where A is a unknown constant acquired empirically from the experiment. In the inset to figure 4.6a we fit the data from B = -5 to 5 T with a second order polynomial, extracting the parameter A that decreases with increasing temperature. Similar magnetoresistance dependence has been observed in Bi NW [50] and bulk Sb_2Te_3 [58, 66]. The magnetoresistance is slightly subparabolic for $B > 5$ T. For larger (d > 50 nm) nanowires, the carrier mobility decreases (as signified by the resistance increase) as the temperature is raised because of increased phonon scattering. As the mobility decreases, the mean free path also decreases and the magnetoresistance changes less as a function of magnetic field. As discussed in the previous chapter, it is impossible to measure the Hall coefficient in the nanowire geometry. Without knowing the Hall coefficients in equation 4.2, it is difficult to make conclusions that are more quantitative than the statements above.

We note that the nanowire samples do not exhibit Shubnikov-de Hass oscillations, most likely due to low mobility. Signatures of topological surface states are not observed because the Fermi level is deep in the bulk valence band away from the gap. Figure 4.6b shows a comparison between the magnetoresistance for a 70 nm NW at 6 K when the magnetic field is in the direction perpendicular and parallel to the NW [110] axis. While the perpendicular magnetoresistance increases by 50% at B = 10 T

the parallel magnetoresistance increases by only 10%, signifying the anisotropy of the Fermi surface in Sb_2Te_3 [67]. If the electron orbits are closed, the magnetoresistance should saturate at high fields [1]. The absence of saturation in our nanowires in both parallel and perpendicular fields suggests that electrons are traversing open orbits along the Fermi surface. The effective mass of the upper and lower valence bands in Sb_2Te_3 varies from $m^* = .034m_e$ to $m^* = 1.24m_e$ due to the anisotropy of the ellipsoidal hole pockets [24]. The anisotropy of the effective mass tensor might be responsible for the magnetoresistance variations in parallel and perpendicular fields. More detailed studies of the cyclotron resonances along different directions of the crystal axes, similar to the experiment done in [68], is needed to provide a more detailed understanding of the nanowire Fermi surface.

4.7 Summary

The diameter dependence of the transport coefficients of Bi nanowires and chacogenide Sb_2Te_3 nanowires has been measured in the diameter range of 30 nm $< d_{\mathrm{Bi}} <$ 50 nm and 20 nm $< d_{\mathrm{Sb_2Te_3}} <$ 100 nm, respectively. Although we found an increase in the TEP of Sb_2Te_3 nanowires with decreasing nanowire diameter, the electronic power factor was not greatly enhanced. We believe the predicted ZT enhancement is the result of a decrease of the thermal conductivity due to the decreased diameter in smaller nanowires. The lack of experimental capability to acquire the temperature dependence of the carrier density in our nanowires limit the amount of quantitative information we can extract about the materials. In future studies, it would be interesting to explore the transport properties of Bi and Sb_2Te_3 nanowires with even smaller diameters to probe the ultimate limit of scaling in these materials.

Chapter 5

Thermoelectric transport in graphene

The next two chapters will discuss the transport properties of low dimensional carbon materials, graphene and carbon nanotubes. Although the crystalline 3-dimensional carbon materials, graphite and diamond, have been around for centuries, low dimensional allotropes have only been discovered recently. In 1985, the buckyball C_{60} was discovered in Rice University as the first member of the 0D fullerene family [69]. In 1991, even though Sumio Iijima of the NEC Corporation in Japan was trying to synthesize fullerenes, he stumbled upon the first 1D carbon nanotubes [70]. Finally in 2004, researchers at Manchester University in England have isolated single sheets of 2D graphene [71]. Interest in graphene's unique electronic structure was sparked by the observation of the peculiar quantum Hall effect (QHE) in Columbia University [72] and Manchester University [73]. There has been tremendous research effort focusing on graphene [74] and its electronic properties [75] in recent years which has led to the 2010 Noble prize in physics.

Graphite is made of many weakly bonded sheets of graphene, while carbon nanotubes can be considered as rolled up sheets of graphene, therefore studying the basic properties of graphene leads to a more fundamental understanding to many members of this carbon family. In this chapter, we focus on the electronic, thermoelectric, and magnetothermoelectric transport properties of graphene based largely on the work published by Y. M. Zuev *et al.* [76]. It should be noted that two works with similar results were published soon after ours [77, 78]. Because graphene has one of the

highest thermal conductivities of any known material [79, 80] its use in thermoelectric energy conversion device applications is limited. However, we investigate how the measured thermoelectric response corresponds to what is predicted by the Boltzmann semiclassical theory in order to ascertain the appropriate transport model in this 2-dimensional material.

We will discuss the electronic structure and the linear dispersion relation of graphene in section 5.1. Section 5.2 will present the experimental procedures that lead to the observation of single layer graphene. We will analyze how the TEP scales as a function of temperature and induced carrier density in section 5.3. Recent theoretical predictions as well as our analysis of the thermoelectric transport in graphene will be discussed in section 5.4. The peculiar quantum Hall effect in graphene is presented in section 5.5. Section 5.6 will discuss graphene's magnetothermoelectric response in the high magnetic field limit. We will finish this chapter with an investigation of the generalized Mott relation and how it compares to our data in section 5.7.

5.1 Linear band structure

The peculiar electronic structure of graphene, which has a thickness of only 0.34nm [81], is the result of the particular arrangement of carbon atoms. Graphene has a hexagonal lattice with a unit cell that contains two carbon atoms separated by 0.142 nm [81]. The electronic states of carbon in this arrangement hybridize to form 3 in-plane σ bonds, one to each of the nearest atoms, in the sp^2 configuration and a perpendicular π bond. The delocalized π states provide the leading contribute to the electronic structure in graphene. The tight binding method is used to calculate the energy dispersion relation and was originally derived in 1947 by P. R. Wallace [82]. The primitive translation vectors of the hexagonal lattice, shown in figure 5.1a, are $\vec{a}_1 = \frac{a}{2}(\sqrt{3}/2, 1/2)$ and $\vec{a}_2 = \frac{a}{2}(\sqrt{3}/2, -1/2)$ where the lattice constant $a = |\vec{a}_1| = |\vec{a}_2| = .142\text{nm}\times\sqrt{3} = .246\text{nm}$. The reciprocal lattice of graphene is a hexagonal lattice, that is rotated by 90° from the real space lattice, with reciprocal lattice vectors $\vec{b}_1 = \frac{2\pi}{a}(1/\sqrt{3}, 1)$ and $\vec{b}_2 = \frac{2\pi}{a}(1/\sqrt{3}, -1)$ shown in figure 5.1b. The

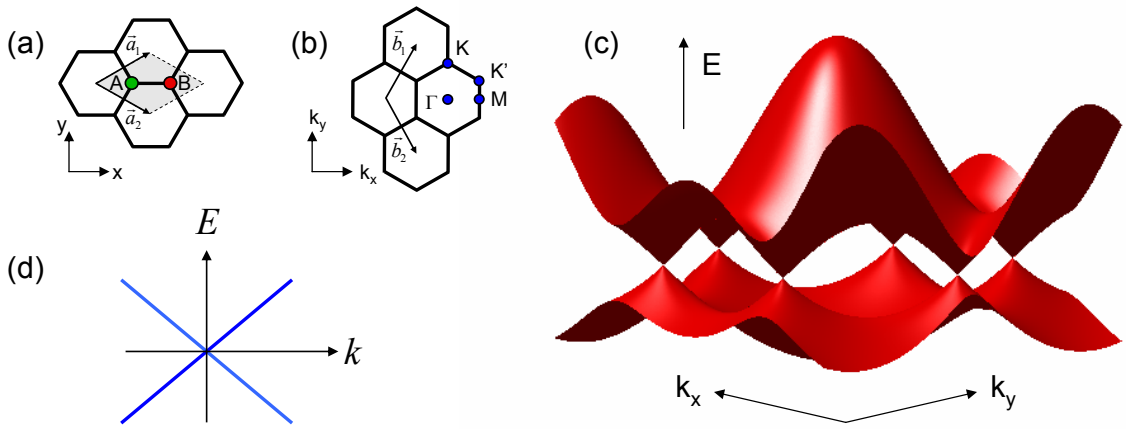

Figure 5.1: (a) Real space 2D hexagonal lattice of graphene, showing the primitive vectors $\vec{a}_1$ and $\vec{a}_2$ and the unit cell shaded in grey with 2 carbon atoms, marked A and B. (b) Reciprocal hexagonal lattice with the reciprocal lattice vectors $\vec{b}_1$ and $\vec{b}_2$ and high symmetry points. (c) Tight binding calculation of the graphene band structure using equation 5.1 with $E_{2p} = 0$, $t = -3.033$ eV, and $s = .129$ eV. (d) Linear energy band dispersion near the K points.

high symmetry points (Γ - zone center, K - zone corner, and M - zone edge) of the Brillouin zone are also shown. Considering only nearest-neighbor interactions, the spectrum is shown to be [81]:

$$E(\vec{k}) = \frac{E_{2p} \pm tw(\vec{k})}{1 \pm sw(\vec{k})} \tag{5.1}$$

where E_{2p} is the energy of the $2p_z$ orbital, t is the nearest-neighbor transfer integral, s is the overlap integral between the nearest A and B atoms, and $w(\vec{k}) = \sqrt{1 + 4\cos\frac{\sqrt{3}k_x a}{2}\cos\frac{k_y a}{2} + 4\cos^2\frac{k_y a}{2}}$. Using the values of $E_{2p} = 0$, $t = -3.033$ eV, and $s = .129$ eV, equation 5.1 is plotted in figure 5.1c and shows band crossings at the six K points. It can be immediately observed that graphene is a zero bandgap semiconductor. In order to simplify equation 5.1, $s = 0$ is often used to form a symmetric expression around E_{2p}, which is also set to zero.

$$E(k_x, k_y) = \pm t\sqrt{1 + 4\cos\frac{\sqrt{3}k_x a}{2}\cos\frac{k_y a}{2} + 4\cos^2\frac{k_y a}{2}} \tag{5.2}$$

It is peculiar that the dispersion relation near the crossing points at the bottom of the conduction band and top of the valence band is linear:

$$E = \hbar v_F |\vec{k}| \tag{5.3}$$

where the Fermi velocity is estimated from the tight binding parameters to be $v_F = 10^6$ m/s. Figure 5.1d shows a plot of the dispersion relation. The states are degenerate due to the inequivalent K and K' points in the band structure. This is referred to as the sub-lattice degeneracy. It is interesting to note that in graphene, unlike in most materials with a parabolic dispersion relation, the Fermi velocity is constant and independent of momentum, while the effective mass vanishes. Graphene is ambipolar, which means that by varying the Fermi level, the majority carrier can be either electron or hole. It is important to learn the experimental techniques necessary to investigate the consequences of graphene's unique band structure and dispersion relation.

5.2 Device fabrication

Graphene samples were fabricated using the mechanical exfoliation technique [83] that made many different experiments on this 2-dimensional material possible. The fabrication process is started with a clean thermally grown 300 nm SiO_2/Si wafer and a piece of Kish graphite. Graphite consists of many planes of graphene that are weakly bonded in the out of plane direction. The graphite is rubbed onto regular everyday Scotch tape (this method is also commonly called "the Scotch tape method") in order to separate the individual planes of graphene. The tape is folded several times, making the number of graphene layers smaller every time, and then put into contact with the SiO_2 substrate. There is a chance that individual graphene sheets will cleave off and will be bonded to the oxide surface through Van der Waals forces. A high contrast confocal microscope is used to image the wafer in order to find single and multi-layer graphene pieces. Figure 5.2a shows a typical optical microscope image

of a single and bilayer graphene piece on a 300 nm SiO_2 surface. Even though the thickness of single layer graphene is much smaller than the wavelength of light, the thin film interference pattern that is set up in the SiO_2 layer makes the contrast of graphene slightly different than the surrounding oxide, making it visible [84].

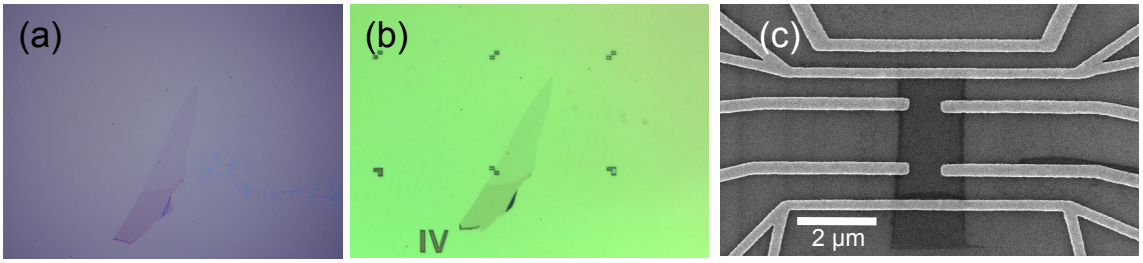

Figure 5.2: (a) Optical microscope image (100x) of single and bilayer graphene on a 300 nm SiO_2 surface. (b) Optical microscope image of the same sample as in (a) with a PMMA layer and alignment marks written using e-beam lithography. The distance between the centers of the alignment marks is 50 μm. (c) SEM image of a finished 14-probe graphene TEP device that is used to measure thermoelectric and magnetothermoelectric properties.

Standard e-beam lithography techniques, see section 4.3, are used to make the 3/30 nm Ti/Au electrodes. Figure 5.2b shows the graphene with a developed PMMA layer and alignment marks. Making Ohmic contact to the graphene is generally quite easy because graphene is essentially a metal so no Schottky barrier is formed at the graphene-electrode interface. The graphene piece is electrically isolated from the heater electrode after an oxygen plasma etching step. We use a Technics 800 Reactive Ion Etching (RIE) system with plasma power of 50 W, oxygen pressure of 200 mTorr, and etching time of 10 seconds, in order to completely cut a single layer graphene piece. Often the channel resistance of the graphene increases from 1 kΩ to 1 MΩ after the plasma etching step. Due to the geometric restrictions of our TEP measurement (see section 2.1) relatively small pieces of graphene have to be used. It is possible that the oxygen plasma degrades the graphene contacts by a lateral etching process underneath the PMMA mask layer. Figure 5.2c shows an SEM image of a typical finished 14-probe graphene TEP device on a SiO_2 surface. The Hall

bar electrodes are used to study the QHE, Nernst effect, and magnetothermoelectric transport properties of graphene. Raman spectroscopy [85] and the QHE [72] are used to verify that our samples are indeed single layer graphene. The degenerately doped Si acts as a back gate in order to modulate the carrier density and therefore the Fermi energy of the graphene sheet.

5.3 Gate dependence

Devices were measured in a vacuum cryostat with pressure in the 10^{-6} Torr range and temperature between 4 K and 300 K. In order to improve mobility and electron-hole symmetry, the devices were first annealed in vacuum at 400 K. Figure 5.3a shows the gate dependence of conductivity of a graphene sample taken at several temperatures. As the Fermi level passes through the charge neutrality point (CNP), also called the Dirac point where $E_F = 0$, the conductivity passes through a minimum. Even though the density of states of graphene vanishes at the charge neutrality point, the conductivity does not vanish because of the existence of inhomogeneous electron-hole puddles [86]. It can be seen that the conductivity varies linearly as a function of applied gate voltage, $\sigma \propto V_g$. This is generally attributed to the fact that the dominant carrier scattering mechanism is charged impurity scattering [87]. There are several sources of charged impurities for substrate supported graphene devices which include charge traps in the oxide, residues of the lithography fabrication process, and adsorbed molecules such as water or hydrocarbons. The linear slope of the conductivity as a function of gate voltage is used to extract the mobility, μ, of the graphene samples. We can relate the Drude conductivity, $\sigma = ne\mu$, and the definition of the 2D conductivity, $\sigma = \frac{GL}{W}$, where G is the conductance, L is the width, and W is the width of a sample, to the expression of the capacitively coupled induced carrier density:

$$n = (V_g - V_D)\frac{C_g}{e} \tag{5.4}$$

where V_D is the back gate voltage of the Dirac point and $C_g = 115\ aF/\mu m^2$ is the capacitive coupling to the gate acquired from QHE measurements [72]. Due to

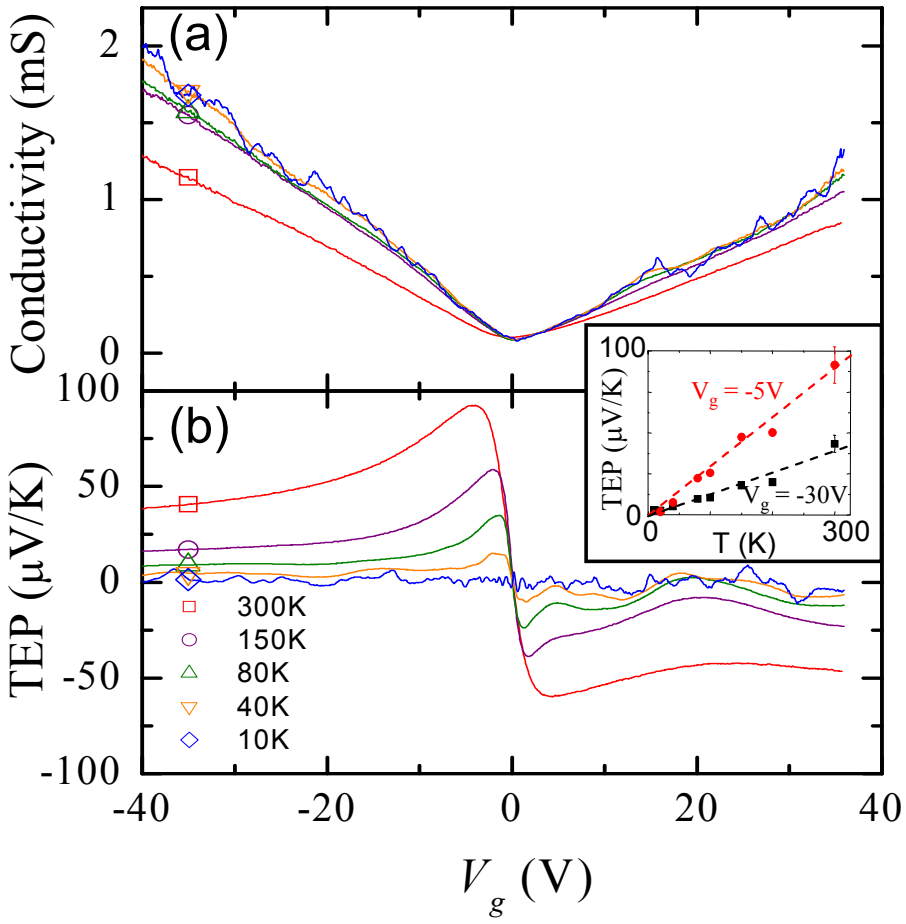

Figure 5.3: (a) Conductivity and (b) TEP of graphene as a function of applied gate voltage for several temperatures. Graphene exhibits both positive and negative values of TEP and has a TEP = 0 at the charge neutrality point. The inset shows the temperature dependence of the TEP taken at 2 gate voltage points, where the dashed lines are linear fits to the data.

adsorbate doping the V_D can be nonzero. The mobility is therefore

$$\mu = \frac{GL}{W\Delta V_g C_g} \tag{5.5}$$

where $\Delta V_g = (V_g - V_D)$. The mobility of the sample in figure 5.3 is 7,000 cm^2/Vs. Typical mobilities of our substrate supported samples are in the range of 1,000 to

7,000 cm^2/Vs. In suspended graphene, as well as in most bulk metals, the conductivity has a strong temperature dependence because the dominant scattering source is the temperature activated distribution of acoustic phonons [88]. There is little temperature dependence in the conductivity in our SiO_2 supported graphene because the intensity of charged impurity scattering does not change very much as a function of temperature. At low temperatures, $T < 30$ K, universal conductance fluctuations are observed in the conductance, and are quantitatively correlated to the oscillations observed in the TEP, as we will show later.

The thermoelectric response of graphene, which was measured simultaneously as the conductivity using our AC measurement technique, is plotted as a function of gate voltage for several different temperatures in figure 5.3b. Graphene exhibits a peak value of the TEP of $\sim$80 μV/K, which is fairly high for a metallic system. Since graphene can have both positive and negative majority carriers, both positive and negative values of the TEP can be observed. At the charge neutrality point the TEP tends to zero. The electron-hole asymmetry observed in the TEP mirrors that observed in the conductivity. It is not intrinsic to graphene and is most likely due to charged impurities [87] or the formation of a p-n junction at the electrode contacts [89]. Unlike the conductivity, the magnitude of the TEP has a linear temperature dependence. The inset of figure 5.3 shows TEP plotted as a function of temperature at two gate voltage points, where the dotted lines are linear fits to the data. At low temperature, mesoscopic oscillations in the TEP are observed. As we have seen with other material systems, the linearity of TEP as a function of temperature suggests that the mechanism for thermoelectric generation is diffusive thermopower. Phonon-drag components of the TEP are not observed, which is consistent with weak electron-phonon coupling in graphene [88, 90] compared to other systems.

5.4 Semiclassical formalism

We continue our analysis of the measured TEP by considering the Boltzmann semiclassical formalism. Because of screening effects and/or high carrier concentrations,

it is very difficult to uniformly adjust the Fermi energy of a bulk material throughout its volume. One of the unique features of our measurement method is the ability to uniformly tune the Fermi energy in our 0.34 nm thick graphene with the applied gate voltage. This allows us to quantitatively check the capability of the semiclassical Boltzmann formalism to predict the thermoelectric response in graphene.

Graphene provides an interesting platform to test models of transport in both the degenerate ($E_F \gg k_B T$) and non-degenerate ($E_F \ll k_B T$) limits since we can vary the temperature and Fermi energy to the appropriate values. The TEP is equivalent to the entropy carried per unit charge. Away from the CNP, the electronic system is highly degenerate and the entropy transported in the channel is proportional to the number of thermally activated carriers over the degenerate Fermi Sea, leading to TEP $\propto T/E_F$. Close to the charge neutrality point, however, the electron gas becomes non-degenerate and both electrons and holes are thermally populated. Here the TEP gains opposite contributions from electrons and holes, so $|S|$ decreases as $|n|$ decreases. However, the true non-degenerate limit is difficult to achieve in the experiment because electron-hole puddles near the CNP produce a finite local density $> 10^{11}/cm^2$ [86]. In order to understand the measured thermoelectric response in more detail, we investigate the predictions made by recent theoretical investigations.

From equation 5.3 it can be seen that the electronic density of graphene is given by

$$n = \frac{1}{\pi}\left(\frac{E_F}{\hbar v_f}\right)^2 \tag{5.6}$$

If only Coulomb scattering from the charged impurities is considered, the conductivity would scale as $\sigma \propto V_G \propto E_F^2$ [87]. The predicted thermopower would then only depend on the position of Fermi energy:

$$S = -\frac{\pi^2 k_B^2 T}{3e}\frac{2}{E_F} \tag{5.7}$$

This approach captures the $1/E_F$ trend of the TEP in the degenerate regime, but is off by roughly a factor of 2 from the measured data. Clearly in the non-degenerate

regime, as $E_F \to 0$, the TEP diverges and this formalism breaks down. When screening and the contribution of electrons and holes near the CMP is considered, the predictions are closer to the experimental data [91]. The appropriate treatment of vacancies, cracks, and boundaries in the graphene sheet lead to an additional term in the thermopower [92]:

$$S = -\frac{\pi^2 k_B^2 T}{3e}\frac{2}{E_F}(1 + (\ln E_F/\tilde{v}_0)^{-1}) \tag{5.8}$$

where $\tilde{v}_0 = \hbar v_F/R_0$ and R_0 is the vacancy radius. This model also breaks down in the region close to the charge neutrality point. In order to investigate the non-degenerate regime more closely, the effects of electron-electron interactions are considered in [93, 94], where a relativistic hydrodynamic model of transport is used. In the highly interacting regime, deviations of the TEP from the semiclassical results are predicted in the non-degenerate regime. In the disorder limited regime, however, the thermopower is predicted to follow the Mott relation [94].

We consider an empirical approach in order to understand our measured data. It has been shown that the two terminal conductance, G, of a mesoscopic system which includes the contact resistance can be used in the Mott relation [95]. From equation 1.18 we have:

$$S = -\frac{\pi^2 k_B^2 T}{3e}\frac{1}{G}\frac{dG}{dV_g}\left.\frac{dV_g}{dE}\right|_{E=E_F} \tag{5.9}$$

Considering equation 5.4 and 5.6, it is clear that $dV_g = \frac{e}{C_g\pi}\frac{2E_F}{(\hbar v_F)^2}dE_F$ and $E_F = \sqrt{C_g\pi(\hbar v_F)^2|\Delta V_g|/e}$. The last term in equation 5.9 is therefore equal to

$$\frac{dV_g}{dE_F}(V_g) = \frac{\sqrt{e}}{C_g\pi}\frac{2}{\hbar v_F}\sqrt{|\Delta V_g|} \tag{5.10}$$

which is simply proportional to the square root of the applied gate voltage difference. We numerically differentiate the measured conductance data and plug the results into equation 5.9. Figure 5.4 shows excellent agreement between the measured TEP

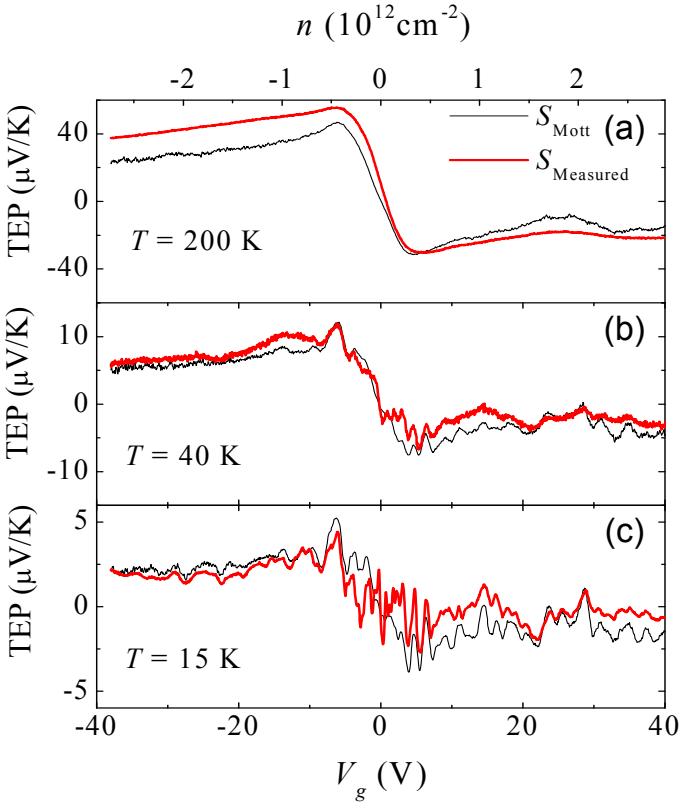

Figure 5.4: Measured TEP (thick red lines) and calculated TEP (thin black lines) using the equation 5.9 plotted as a function of gate voltage, or equivalently carrier density, for $T = 200$ K (a), 40 K (b), and 15 K (c).

and the calculated TEP using equation 5.9 for three temperatures. It is noted that there are no fitting parameters used to calculate the thermopower, and that we are simply comparing two individual sets of data, one for the thermopower and one for the conductance. Even though the Mott relation should not be used close to the CNP because the degenerate condition is violated, we can see that there is still good agreement between the measured and calculated TEP in this regime. It is difficult to quantify deviations from the Mott formula in the non-degenerate regime due to electron-electron interactions [94] in part because the TEP tends to zero at the CNP. It is also possible that the mobilities of our substrate supported samples are too low in the temperature range studied in order to observe the effects of electron-electron

interactions.

We have shown that the semiclassical formalism is able to predict the thermoelectric response in graphene quite well, both qualitatively and quantitatively. Another way to put this that the thermoelectric response of a graphene sheet can be acquired by simply measuring the conductance and using equation 5.9. Now that we have understood graphene's thermoelectric response in the absence of a magnetic field, it is time to look at magnetic field effects.

5.5 Quantum Hall effect in graphene

The measurement of the peculiar quantum Hall (QH) effect was one of the critical experiments that ignited the field of research in graphene [72, 73]. The quantum Hall effect occurs in 2-dimensional electron systems in the presence of a high magnetic field. As discussed in section 3.1, in the low field limit, the usual Hall effect can be used to measure the carrier concentration of a material. In fact, the Hall effect was used in graphene to measure the back gate induced sheet carrier density in order to obtain the parameter C_g used above [72]. Classically, the cyclotron radius is defined as $r_c = \frac{vm}{eB}$, while the frequency is $\omega_c = \frac{eB}{m}$. Therefore as the field is increased the cyclotron orbits of the electrons become smaller. As the field becomes large, the orbits close in on themselves and the only non-zero current that propagates through the sample is along the edge, in the so called skipping states or edge states [54]. The diagram in figure 5.5a shows the effects of high magnetic field on the electron orbits as well as formation of edge states in a 2-dimensional electron gas (2DEG).

The exact spectrum of a 2DEG in the quantum Hall regime can be derived using the free electron Hamiltonian in the presence of a magnetic field and using the Landau gauge [96]. The energy is quantized $E_N = (N+1)\hbar\omega_c$ around integer values of the cyclotron frequency, called Landau levels, in a 2DEG. The number of occupied Landau levels (LLs) corresponds to the number of edge states. In graphene, due to the inequivalent K and K' points in the band structure as well as the linear spectrum, the quantization condition is different [72] and described by $E_N = sgn(N)\sqrt{2e\hbar v_F^2|N|B}$,

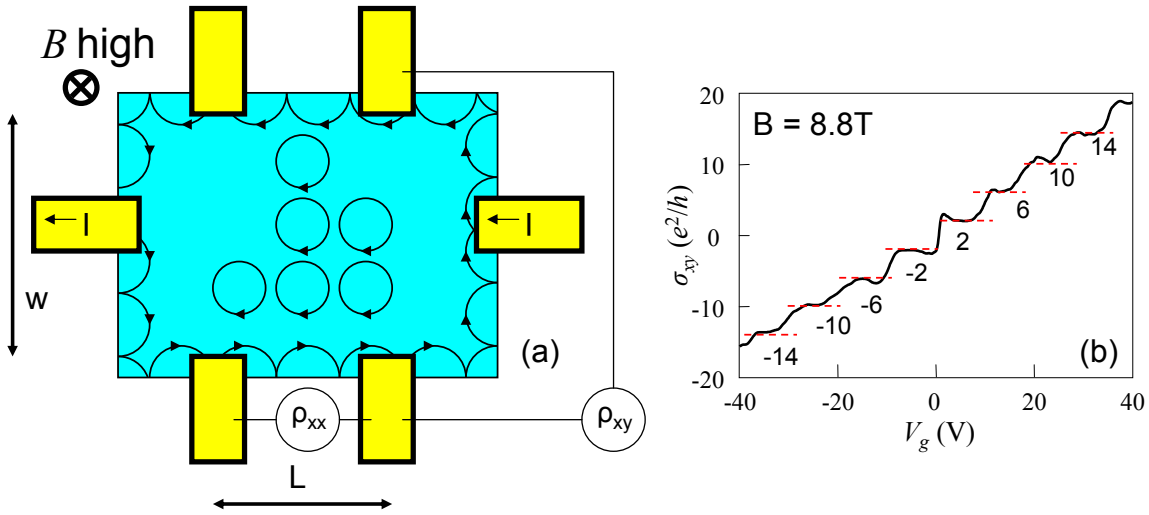

Figure 5.5: (a) Diagram of the the Hall bar geometry used to measure the tensor components of the resistivity in the high field regime in order to investigate the quantum Hall effect in a 2DEG system. (b) Transverse conductivity of a graphene sample taken at $T = 10$ K and $B = 8.8$ T showing quantized plateaus at filling factors $\nu = \pm 2, \pm 6, \pm 10, \pm 14$.

where N is the Landau level index including both positive and negative intergers, the $sgn(N)$ is positive for hole LLs and negative for electron LLs. The formation of quantized Landau levels at specific energies leads to the observation of interesting phenomena in the magnetoresistance, R_{xx}, and Hall resistance, R_{xy}, in graphene.

The Hall bar electrodes are used to measure the components of the resistivity, $\hat{\rho}$, and conductivity, $\hat{\sigma}$, tensors [97]:

$$\hat{\rho} = \begin{pmatrix} \rho_{xx} & \rho_{xy} \\ -\rho_{xy} & \rho_{xx} \end{pmatrix} \qquad \hat{\sigma} = \hat{\rho}^{-1} = \frac{1}{\rho_{xx}^2 + \rho_{xy}^2} \begin{pmatrix} \rho_{xx} & -\rho_{xy} \\ \rho_{xy} & \rho_{xx} \end{pmatrix} \tag{5.11}$$

where $\rho_{xx} = R_{xx}\frac{W}{L}$, $\rho_{xy} = R_{xy}$, $\rho_{xy} = -\rho_{yx}$, $\rho_{xx} = \rho_{yy}$, and W and L are the width and length of the Hall bar, respectively, shown in figure 5.5a. The transverse conductivity, $\sigma_{xy} = \frac{-R_{xy}}{(R_{xx}W/L)^2 + R_{xy}^2}$, in graphene is found to be quantized in units of the conductance quantum, e^2/h, where h is Planck's constant. The quantization condition depends on the filling factor, $\nu = g(N + 1/2)$, where $g = 4$ is the degeneracy (2 for spin and 2 for

sub-lattice) in graphene. Figure 5.5b shows that the observed transverse conductivity in graphene follows the quantization condition:

$$\sigma_{xy} = \pm(N + 1/2)\frac{4e^2}{h} \tag{5.12}$$

From equations 5.4 and 5.6, we know that gate voltage induces a linear change in the density but a quadratic change in the Fermi energy. Unlike in a 2DEG, the Landau levels in graphene are not spaced equidistantly in energy but rather as the square of the energy, $E_N \propto \sqrt{N}$. As a result, it is clear why the centers of the plateaus in σ_{xy} are spaced equidistantly in gate voltage. Now that we understand the basics of the QHE, is it time look at the detailed measurement of the magnetothermoelectric response of graphene.

5.6 Magnetothermoelectric transport in graphene

If a perpendicular magnetic field is present, thermally diffusing electrons will experience a Lorentz force that will bend their trajectories. The measured thermopower will then consist of both a longitudinal component, S_{xx}, and a transverse component, S_{yx}, also referred to as the Nernst coefficient [8]. Using the Hall bar geometry we measure both the resistivity and thermoelectric tensors as a function of gate voltage and magnetic field to produce 2-dimensional color plots called "megasweeps". The megasweep in figure 5.6a shows a linear growth of the oscillations of $\sigma_{xy}(V_g)$ with increasing magnetic field. This behavior clearly indicates that Shubnikov-de Hass oscillations are present in graphene as previously observed [72, 73]. The inset of figure 5.6a shows an optical microscope image of the device measured.

At high field, $B \sim 9$ T, fully developed quantum Hall effect is observed. Figure 5.6d,e show single traces of R_{xx} and R_{xy} at $B = 8.8$ T and $T = 10$ K. The dotted lines indicate the filling factors $\nu = \pm 2, \pm 6, \pm 10, \pm 14$ in between Landau levels where the DOS of the electronic system vanishes. As a result, R_{xx} also vanishes, while $R_{xy} = \sigma_{xy}^{-1}$ exhibits the characteristic plateaus for the graphene system. Observing

the quantized Hall resistance plateaus at $R_{xy} = \pm\frac{1}{2}\frac{h}{e^2}, \pm\frac{1}{6}\frac{h}{e^2}, \pm\frac{1}{10}\frac{h}{e^2}, \ldots$ is a method to validate that a sample is single layer graphene, and can also be used as a resistance standard [98] because the values only depend on the universal constants of the charge of an electron and Planck's constant.

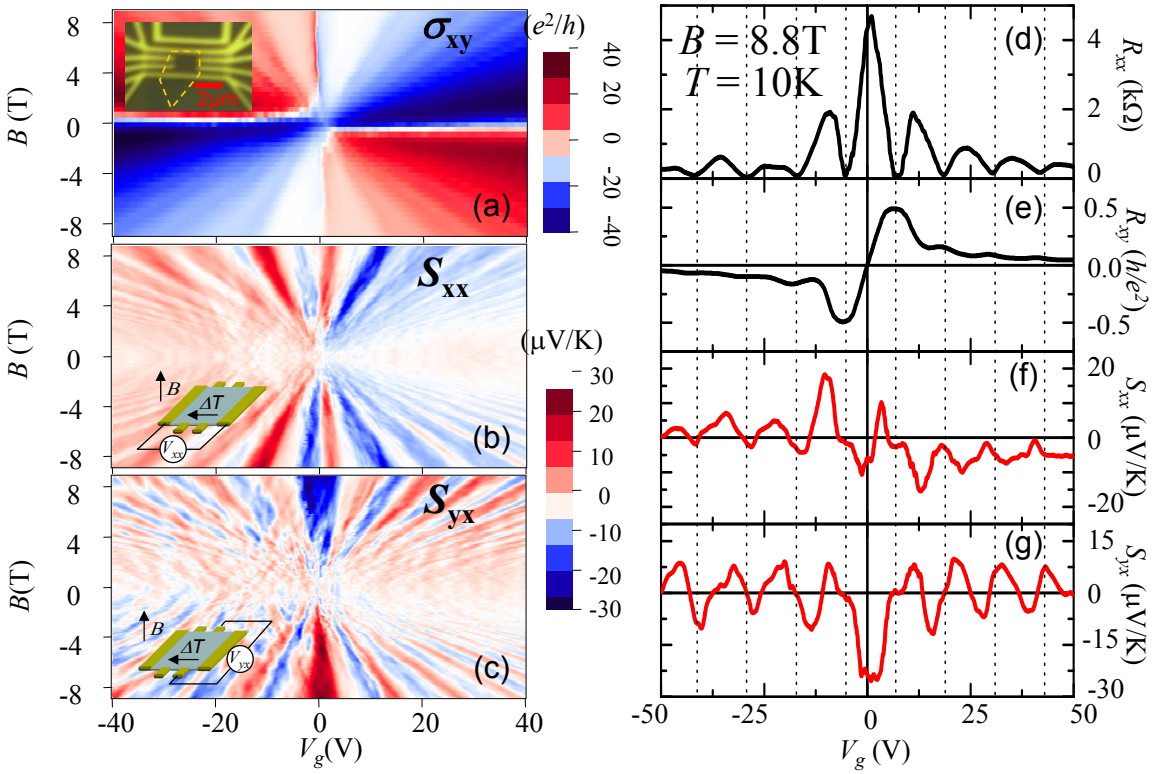

Figure 5.6: (a) Hall conductance, (b) longitudinal TEP S_{xx}, and (c) transverse TEP S_{yx}, as a function of V_g and B field at $T = 10$ K. The inset in (a) shows an optical microscope image of the device measured. The insets in (b) and (c) show the electrode configurations for the S_{xx} and S_{yx} measurements, respectively. Single trances of (d) R_{xx} (e) R_{xy} (f) S_{xx} and (g) S_{yx} as a function of V_g at a fixed magnetic field $B = 8.8$ T and $T = 10$ K. The vertical dashed lines indicate filling factors corresponding to $\nu = \pm 2, \pm 6, \pm 10, \pm 14$. All of the data is averaged with respect to positive and negative values of the magnetic field in order to remove mixing between the longitudinal and transverse components.

The thermopower was recorded as $S_{xx} = -\frac{E_x}{\partial_x T} = \frac{\sqrt{2}V_{xx}(2\omega)}{\Delta T}$ and $S_{yx} = -\frac{E_y}{\partial_x T} = \frac{\sqrt{2}V_{yx}(2\omega)\frac{l}{W}}{\Delta T}$ where $E_{x(y)}$ is the electric field along the $x(y)$ direction. We scale the

transverse voltage by the ratio of l/W, where l is the separation between the near and far electrodes, in order to measure the appropriate transverse field. The megasweeps shown in figure 5.6b,c depict S_{xx} and S_{yx} that were measured in the geometry shown in the insets of each figure, respectively. It can be seen that S_{xx} is anti-symmetric in V_g and symmetric in B field while S_{yx} is symmetric in V_g and anti-symmetric in B field. Like we saw in the zero field measurement, the longitudinal component of the thermopower is proportional to the charge majority carrier, being positive on the hole side and negative on the electron side. Figure 5.6f,g show single trances of S_{xx} and S_{yx} at $B = 8.8$ T, taken from the megasweeps. In order to avoid error associated with non-symmetric Hall bar electrodes, we symmetrize all of the data with respect to positive and negative magnetic field. When the Fermi level is between LLs, along the dashed lines in figure 5.6, the DOS vanishes so there are no carriers that are able to participate in diffusion and both S_{xx} and S_{yx} tend to zero. The magnetothermoelectric response of graphene in the QH regime is similar to that predicted [99–102] and observed [103, 104] in 2DEGs.

We observe that $|S_{xx}|$ is peaked around the Landau level centers and decreases as the Landau level index, N, increases. In 2DEGs in the QH regime, the $|S_{xx}|$ is predicted to vanish in the zero temperature limit if $E_F > |E_N - k_B T|$, where E_N is the energy of the Nth LL [101, 102], with the peaks approaching $S_{xx} = -\frac{k_B}{e}\frac{\ln 2}{N+1/2}$ in the disorder free limit. It can be seen that these predicted values are independent of temperature. In graphene, the additional phase shift associated with the Berry phase changes the quantization condition to:

$$S_{xx} = -\frac{k_B}{e}\frac{\ln 2}{N} \tag{5.13}$$

for $N \neq 0$. The same argument leads to the familiar correction of the quantization condition of the Hall conductance in the QH regime, $\sigma_{xy} = gN\frac{e^2}{h}$ for 2DEGs as opposed to $\sigma_{xy} = g(N + 1/2)\frac{e^2}{h}$ for graphene that we have seen earlier. The observed peak values of S_{xx} follow the $1/N$ trend although they are smaller than the predicted

values and are broadened around the LL centers. This is most likely due to temperature and disorder broadening in our graphene samples. It is interesting that the quantized behavior of S_{xx} are similar to what is observed not only in 2DEGs [103] but also for quantum point contacts (QPCs) in 2DEGs [105] where the number of modes of the QPC replaces the Landau level index.

5.7 Generalized Mott relation

We further analyze the measured S_{xx} and S_{yx} data by considering the semiclassical analysis that we used for the zero B field case. However, now we have to consider the tensor components of the conductivity and the TEP, so we employ the generalized Mott relation that holds for all temperatures and can be applied to the QH regime [100, 101]:

$$S_{ij} = -\frac{\pi^2 k_B^2 T}{3e} \sum_k (\sigma^{-1})_{ik} \left(\frac{\partial \sigma}{\partial E_F} \right)_{kj} \tag{5.14}$$

where σ_{ij} is the conductivity tensor and i, j represent the x, y components. According to equation 5.14, we expect that S_{xx}/T becomes temperature independent in the QH limit where σ_{ij} is temperature independent. Indeed, figure 5.7a shows that the measured S_{xx}/T is rather temperature independent for T < 20 K. Above this temperature, however, the oscillation amplitude of S_{xx}/T becomes smaller since thermal activation across the disorder broadened LLs becomes appreciable and the QH effects disappear. Figure 5.7b shows good agreement between the measured S_{xx} (S_{yx}) and the calculated thermoelectric components using equation 5.14, indicating that the semiclassical Mott relation, extended into the QH regime, works well for both holes ($N < 0$) and electrons ($N > 0$). Near the zeroth LL ($N = 0$) at the CNP ($V_g \approx V_D$), however, the measured S_{xx} exhibits a pair of anomalous oscillation that shows a distinct deviation from equation 5.14. We remark that this pair of S_{xx} peaks near the zeroth Landau level shows opposite TEP polarity, i.e., positive peak on the electron side ($V_g > V_D$) and negative peak on the hole side ($V_g < V_D$). This pair of opposite polarity oscillations could be indicative of a peculiar QH state stemming from the $N = 0$ LL. It

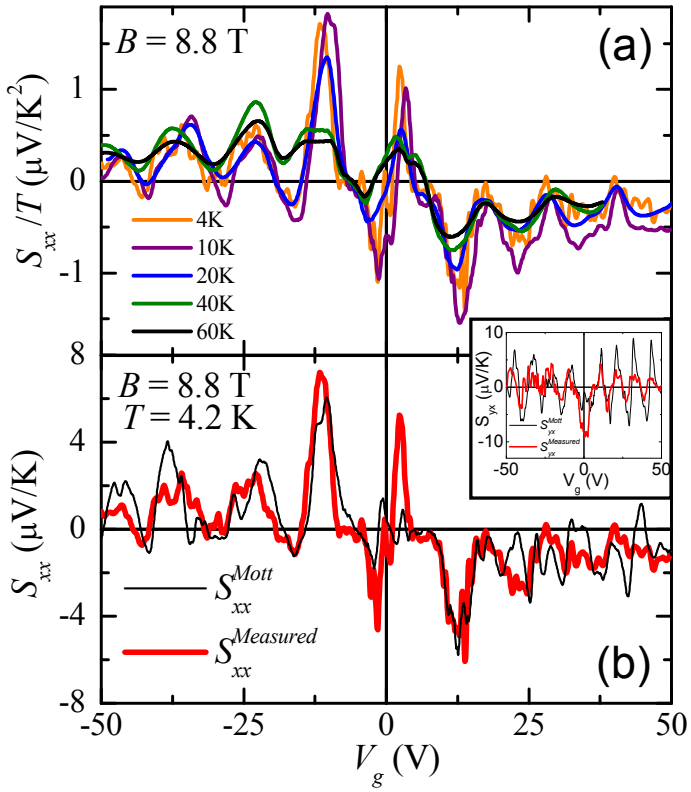

Figure 5.7: (a) Temperature dependence of S_{xx}/T as a function of V_g at $B = 8.8$ T. (b) Measured S_{xx} (thick red) and the S_{xx} predicted by the generalized Mott relation (thin black) at $B = 8.8$ T and $T = 4.2$ K showing deviations near the N = 0 LL. The inset of (b) shows the corresponding measured S_{yx} and calculated S_{yx}.

has been speculated that this LL produces a pair of counter propagating edge states when the Fermi level is at the CNP [106]. In this scenario, the polarity of the inner edge state is opposite to the sign of the bulk majority carrier, which may generate the anomalous TEP observed. We also note that since the aspect ratio of the sample has $W > L$ where W and L are the width and length of the graphene flake, respectively, the two-terminal QH conductance is predicted to exhibit a peak near the CNP arising due to partially overlapping LLs [107, 108]. It is possible that the anomalous oscillations of S_{xx} are a result of this geometry dependent finite longitudinal conductivity. In addition, a large enhancement of S_{yx} (inset of figure 5.7b) is observed near the CNP, which also deviates strongly from the calculated S_{yx}. Such enhancement of the

Nernst signal is predicted in conventional 2D electron systems, where the magnitude of S_{yx} strongly depends on the disorder strength [100, 101].

We have shown that the measured tensor components of the thermopower in graphene behave in a similar manner to those observed in 2DEGs in the quantum Hall regime. The semiclassical generalized Mott relation predicts the thermoelectric response quite well in the degenerate regime. Further investigation into the origin of the TEP features near the zeroth Landau level is needed.

5.8 Summary

The electronic and thermoelectric response of single layer graphene has been measured as a function of temperature, carrier density, and magnetic field. The linear temperature dependence of the TEP confirms that the electron-phonon coupling in graphene is weak compared to other materials. We have shown that the carrier density dependent behaviors of the conductivity and TEP are well correlated with each other through the semiclassical Mott relation. In the high field limit, when graphene is in the quantum Hall regime, the quantized values of the tensor components of the TEP are similar to those studied in conventional 2-dimensional electronic systems.

In order to understand the interesting features of the TEP near the charge neutrality point in more detail, in both the zero magnetic field and high magnetic field limits, samples with much higher mobilities need to be investigated. Perhaps with the use of a boron nitride substrate, instead of silicon oxide, as the graphene supporting layer, high mobility samples can be attained [109]. It would also be interesting to observe how the TEP scales as the number of graphene layers is increased from one to bulk graphite.

Chapter 6

Thermoelectric transport in single walled carbon nanotubes

In this chapter, we will investigate the transport properties of single walled carbon nanotubes (SWNTs). Carbon nanotubes (CNTs) provide an excellent platform to study low dimensional physics because the electrons are intrinsically confined to a 1-dimensional channel. The electronic transport of individual SWNTs can be studied by contacting them with metallic electrodes with varying degree of transparency. If the electrode contacts are electronically transparent, Fabry-Perot (FP) oscillations in the conductance are observed at low temperatures[110] due to the constructive and destructive interference of the electron wavefunctions. On the other end of the spectrum if resistive contacts are used, the Coulomb blockade (CB) regime dominates the low temperature electronic behavior as the CNT becomes a 0-dimensional quantum dot [111–113]. If the coupling of the CNT QD to the electrode reservoirs is not too high and not too low, the Kondo regime can be observed [114].

By using local gates and quantum point contacts in 2DEG materials, electronic transport in QDs has been extensively studied [54]. Although the 2DEG layer is isolated electrically from the surrounding heterostructure, it is still couple thermally. Because of the experimental difficulty of thermally isolating 2DEG QDs, there have been far fewer thermal transport experiments on these materials. Nonetheless, an experiment investigating the thermopower of a 2DEG QD in the Kondo spin-correlated

regime has been performed [115]. Interestingly, in the presence of spin interactions between the tunneling electrons and the electrode reservoir, deviation of the measured thermal voltage signal and that predicted by the semiclassical Mott formula is observed. However, a temperature calibration measurement could not be performed with the experimental setup used, therefore a quantitative comparison could not be made. We were motivated by these results on 2DEG quantum dots to study the interaction behavior in individual single walled carbon nanotubes in the Fabry-Perot and Kondo regimes. Using our measurement technique, we try to correlate the behavior of the conductance and thermopower using the Mott relation at low temperatures.

The amplitude of the quantum oscillations in carbon nanotubes is enhanced at low temperatures. Although carbon nanotubes, like graphene, are highly thermally conductive [116, 117], only 4 acoustic phonon branches are occupied below $T = 30$ K [81], so the thermal conductance is constant and equal to $G = 8g_0^{\text{th}}$, where g_0^{th} is the quantum of thermal conductance [118]. The observed high values of the TEP in SWNTs in the CB regime [119, 120] have provided additional motivation to study SWNTs in the high conductance Fabry-Perot regime to see if a $ZT > 1$ can be achieved at low temperature in this material.

We will discuss the electronic band structure of SWNTs in section 6.1. An overview of device fabrication presented with a discussion of CNT synthesis and SWNT verification techniques will take place in section 6.2. We will present the results of our measurements of the conductance and TEP in highly transparent metallic SWNTs in the FP regime in section 6.3. We analyze out TEP data with the help of the Mott relation in section 6.4.

6.1 Band structure

In order to understand electronic transport of single walled carbon nanotubes, their band structure must be considered. A carbon nanotube is essentially a rolled up sheet of graphene, therefore we can use the tight binding band structure of graphene, derived in section 5.1, as the starting point. The SWNT can be rolled up in many

different ways depending on the chiral indices (n,m) which define the chirality of the nanotube. The periodic boundary conditions in the circumferential direction of the nanotube quantize the reciprocal lattice vector that is perpendicular to the nanotube axis. The reciprocal lattice vectors for a SWNT are defined to be [81]:

$$\vec{k}_1 = \frac{1}{N}(-t_2\vec{b}_1 + t_1\vec{b}_2) \qquad \vec{k}_2 = \frac{1}{N}(m\vec{b}_1 - n\vec{b}_2) \tag{6.1}$$

where $\vec{b}_1$ and $\vec{b}_1$ are the reciprocal lattice vector of graphene defined in section 5.1, $t_1 = \frac{2m+n}{d_R}$, $t_2 = -\frac{2n+m}{d_R}$, $N = \frac{2(n^2+m^2+nm)}{d_R}$ is the number of hexagons in the CNT unit cell, and d_R is the greatest common devisor of n and m. By taking cross sectional

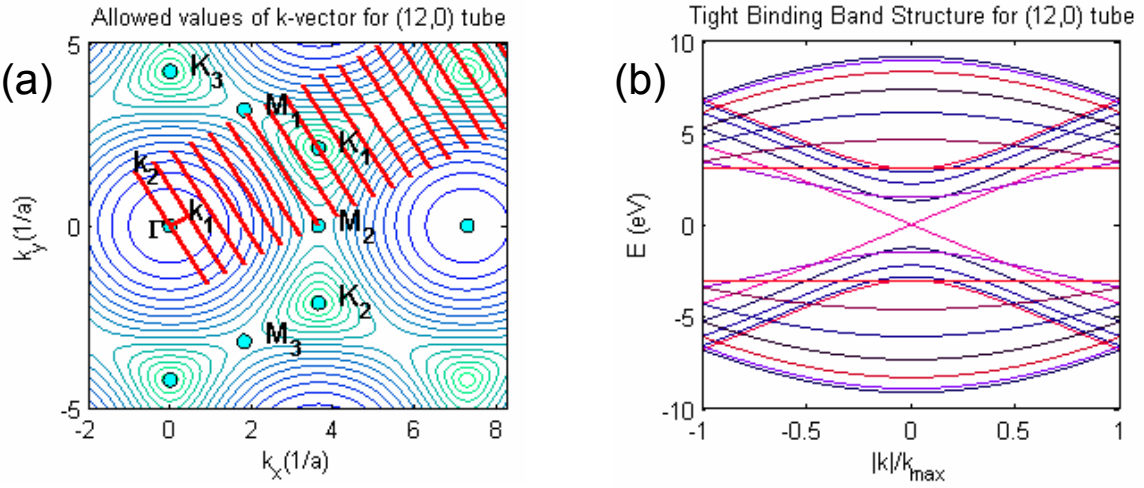

Figure 6.1: (a) Contour plot of the 2D graphene band structure showing the high symmetry points. The red lines show the quantized vector $\vec{k}_2$ of a metallic (12,0) SWNT along which the cross section cuts of the 1D band dispersions are plotted in (b).

cuts along $\vec{k}_2$ of the full graphene tight binding structure along the quantized wave vectors the 1-dimensional energy dispersion of carbon nanotubes is acquired. This method is commonly referred to as the "zone folding technique". Figure 6.1a shows a contour plot of the band structure of graphene in reciprocal space along with the high symmetry points. If the cross sectional line passes though the K point, the SWNT will be metallic, otherwise it will be semiconducting. The quantization condition for

metallic nanotubes is $n - m = 3s$ where s is an integer. Therefore, approximately 1/3 of tubes synthesized will be metallic, if a random distribution is considered.

Figure 6.1b shows the 1D energy band dispersions plotted along the vectors $\vec{k}_2$, shown as the red lines in figure 6.1a, for a (12,0) metallic single walled carbon nanotube. Like in graphene, the dispersion relation is linear in metallic SWNTs. The tight binding method predicts that the density of states near the Fermi energy is constant, however, a small gap is commonly observed in transport [121]. Because dielectric breakdown limits the change of Fermi energy by the gate voltage by more than a few hundred meV in our SiO_2 substrate supported SWNTs, only the energy range near $E_F = 0$ is explored in our transport experiments.

6.2 Device fabrication

In order to experimentally access the highly conducting Fabry-Perot regimes, high quality carbon nanotube devices with transparent contacts have to be fabricated. In order to measure the low conducting Coulomb blockade regime, it is sufficient to simply make contact to the nanotube with a metal electrode. It has been shown that using specifically Pd as the electrode metal [122] produces reliable transparent contact to SWNTs, most likely due to excellent wetting properties of Pd. We use .5/40 nm Ti/Pd electrodes to make transparent contact to our single walled carbon nanotubes, with typical resistances in the range of 10 kΩ to 100 kΩ. A RIE O_2 plasma etching procedure, similar to the step in the graphene device fabrication, is used to isolate the main channel of the CNT device and the heater electrode. We will now discuss the method used to synthesize our carbon nanotubes.

6.2.1 CNT Synthesis

Carbon nanotube growth procedure is extremely important to reproducibly make clean devices, which is required to observe quantum interference effects at low temperature. We utilize a chemical vapor deposition (CVD) technique optimized for a yield of ultra-long single walled carbon nanotubes [123]. The 950 nm SiO_2 growth

substrate is prepared by applying CoMo-doped mesoporous silica as the catalyst material with the use of a toothpick. The 2 nm - 6 nm diameter pores in the silica act to prevent aggregation of the metal nanoparticles. This is important since there is a correlation between the nanoparticle size and the diameter of the CNT that grows from it. We are interested to synthesize individual SWNTs (diameter < 2 nm) and not multi-walled carbon nanotubes (MWNTs) or bundles of SWNTs. In order to improve growth reproducibility, we anneal the samples at 400°C in air to stabilize the catalyst and remove the organic residues. We flow Ar gas through an ethanol bubbler to supply the carbon feedstock gas in the CVD reaction. Ethanol (C_2H_5OH) is used, instead of the more standard acetylene (C_2H_2) or methane (CH_4), because it has a lower activation energy for decomposition and it is safer to handle since it is a liquid at room temperature. We use a tube furnace that is situated on rails in order to rapidly move it into the growth position at 900°C. This "fast-heating" approach is designed for growth of ultra-long highly aligned tubes. The resultant nanotubes are in the diameter range of 0.8 nm to 1.8 nm and grow up to a length of 1 mm. Although the ratio of semiconducting to metallic tubes in our growths is the standard 2:1, CVD methods exist that produce 90% semiconducting tubes [124] or 91% metallic tubes [125]. We will now explain exactly how we verify that our CNTs are indeed metallic SWNT and not MWNTs or bundles.

6.2.2 SWNT verification

It is no easy task to assertion the properties of a material that has a diameter that is 50,000 smaller than a human hair. However, there are several techniques used in order to select the appropriate SWNTs for device fabrication. After the CVD growth, alignment marks are placed upstream of the catalyst islands using an e-beam lithography/metalization step. The sample is imaged using an SEM in order to acquire its position with respect to alignment marks. An SEM image of a long SWNT is shown in figure 6.2a. MWNTs tend to have a large bending radius and charge up brightly, while SWNTs tend to be more curly and more difficult to make out. It is important that the catalyst islands are charged up in the SEM, because the

CNT will not be visible otherwise. The catalyst particles can diffuse near the CNT, thereby contaminating the device channel and provide additional scattering centers. Another reason to grow long tubes, $l > 200\mu m$, is to avoid this issue. Since our

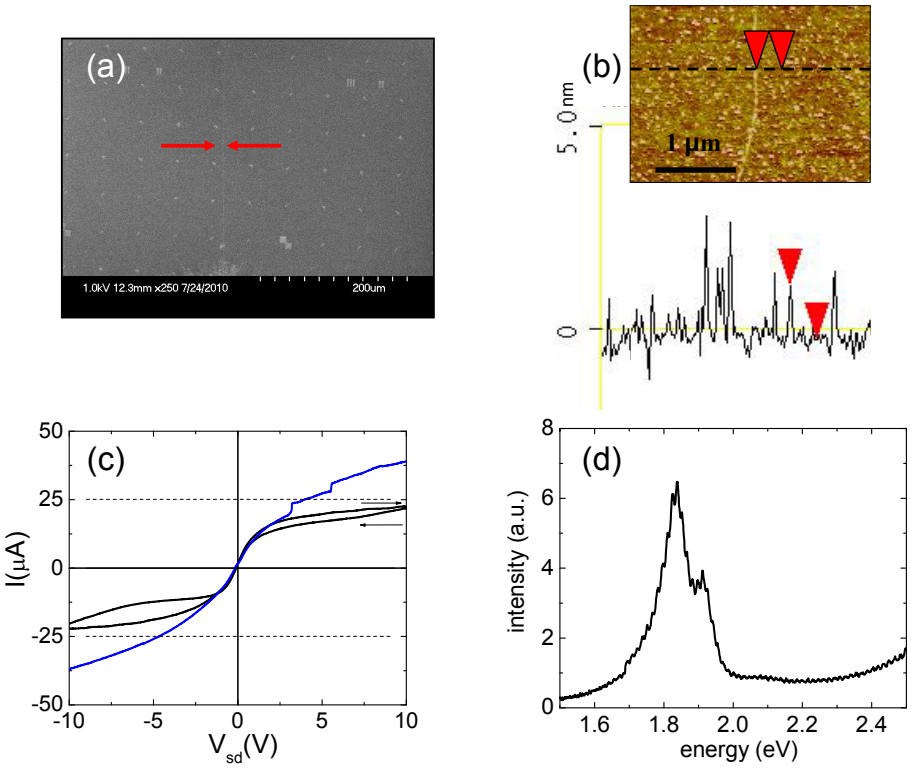

Figure 6.2: (a) SEM image (250kx) of a single walled carbon nanotube (red arrows) with alignment marks. (b) AFM topographical image and linescan, showing the diameter of the SWNT to be 1.5 nm. (c) "High bias test" plotting IV curves for a MWNT (blue) and a SWNT (black) showing current saturation at 25 μA. (d) Rayleigh spectrum of a suspended metallic SWNT.

SEM is not reliable to measure diameters on the order of nanometers (in general a TEM is used to verify atomic scale distances), we use an AFM to confirm that the diameter of our CNT is $\leq$2 nm. Figure 6.2b shows a typical topographical image and a linescan of a SWNT with a diameter of 1.5 nm. Having verified that the CNT is most likely a SWNT, we deposit electrodes and measure the transport properties to further screen the samples. Adjusting the Fermi energy by sweeping the gate voltage allows us to quickly check if the CNT is semiconducting (conductance shows "on" and

"off" regimes) or metallic (conductance is flat). Nanotubes with a gate dependence that shows neither behavior represents either a bundle or a MWNT, where transport from several types of conductors is present.

Due to an efficient optical phonon emission process, the current of a metallic SWNT is predicted to saturate under high bias conditions [126]. The so called "high bias test" is performed on devices in order to see if the current saturates to $\leq 25\mu A$. Figure 6.2c shows IV curves for a SWNT and a MWNT or bundle. The SWNT current saturates at the predicted value, while the MWNT does not, moreover the jumps observed in the current most likely signify the onset of conduction through different shells of the material. If the CNT is grown over a slit, optical characterization, such as Rayleigh and/or Raman spectroscopy, can be used to obtain the chirality of the tube from the precise positions of the energy transitions. Figure 6.2d shows a typical Rayleigh spectrum of a metallic SWNT. After the optical characterization, the CNT can be transferred to a target substrate for transport measurements [127]. This method can be used to measure how the TEP changes as a function of nanotube chirality.

6.3 Transport in the Fabry-Perot regime

We measure verified high quality metallic single walled carbon nanotube devices in a vacuum cryostat between $T = 300$ K and $T = 5$ K. The channel length of 300 nm for our CNT devices was chosen to be as small as lithographically possible for our TEP devices. We are interested in observing coherent quantum interference effects, so the length scale of the channel must be smaller than the coherence length at low temperatures. In order to observe these effects, the 2-terminal conductance, G, should be close to the ballistic limit of $\frac{4e^2}{h}$, where the current is carried by two spin-degenerate modes. The transmission probability at each contact is near unity, however, there is still a finite chance of an incoming electron to scatter and as a result interfere coherently with other electrons in the 1-dimensional electron waveguide [110]. The phenomenon takes its name from the Fabry-Perot optical interferometer where the

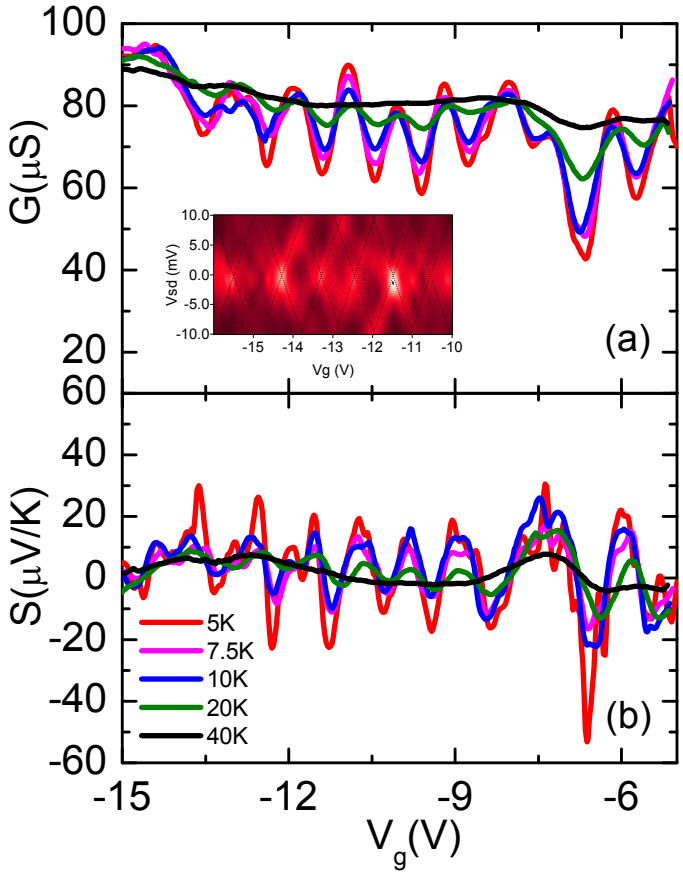

Figure 6.3: Gate dependence of the 2-terminal (a) conductance and (b) TEP of a metallic SWNT with a channel length of 300 nm plotted for several temperatures, showing the onset of Fabry-Perot oscillations. The inset in (a) is a stability diagram of the differential conductance taken at $T = 5$ K, showing higher conductance in black and lower conductance in red. The dashed lines are guides for the eye. The TEP increases as coherent interference effects become larger at low temperatures.

effect was originally observed for light.

Below approximately $T = 30$ K, the electron mean free path [128] and more importantly the coherence length of the SWNT becomes larger than the channel length so quantum interference effects start to dominate the behavior of both the conductance and the TEP. Figure 6.3a plots the gate dependence of the conductance of a metallic SWNT, showing the onset of Fabry-Perot oscillations as the nanotube is cooled down. The amplitude of the conductance oscillations grow as a function of

decreasing temperature and exhibit a constant period in gate voltage. A conductance map (stability diagram) of the zero bias differential conductance, dI/dV, in the V_g - V_{SD} plane is often used to understand the relationship between the applied gate voltage and source drain voltage. The inset of figure 6.3a depicts a stability diagram for the same device taken at $T = 5$ K, showing the crisscrossing pattern that is typically observed in the presence of Fabry-Perot oscillations. Similar to the case of QDs [119], the slope of the lines of constant conductance (shown as dashed lines in the figure as a guide for the eye) can be used to extract the gate coupling term, α.

$$\alpha = \frac{dE_F}{dV_g} = \frac{e\Delta V_{SD}}{2\Delta V_g} \tag{6.2}$$

where the factor of 2 appears because the Fermi energy in a ballistic sample is the average of Fermi energies of the two leads [97, 129]. From the stability diagram we extract $\alpha = .01eV/V$ for the particular device studied. Since this is a relatively short channel length (300 nm) device with a thick gate oxide (950 nm), the gate coupling is relatively weak.

Figure 6.3b shows that the thermopower is fairly smooth and close to zero at $T = 40$ K. As the amplitude of the Fabry-Perot oscillations start to increase at lower temperature, the TEP becomes larger. However, with peak values on the order of only tens of μV/K, the efficiency values are quite small at low temperatures. To calculate the low temperature ZT, we use:

$$ZT = \frac{S^2 T\sigma}{\kappa} = \frac{S^2 N\frac{2e^2}{h}}{(2N+4)g_0^{\text{th}}} = \frac{S^2}{L_0}\frac{2N}{2N+4} \tag{6.3}$$

where N is the number of electronic modes, $(2N+4)g_0^{\text{th}} = (2N+4)\frac{\pi^2 k_B^2 T}{3h}$ is the maximum thermal conductance, and $L_0 = \frac{\pi^2 k_B^2}{3e^2}$ is the Lorenz number. The maximum efficiency is found to be ZT $< .006$ at $T = 5$ K in the Fabry-Perot regime. In single walled carbon nanotubes, as in most materials, the electrical conductivity and the TEP are intrinsically inversely related so achieving a high ZT is not trivial. We continue our analysis of the TEP by examining the expected thermoelectric response

in this coherent 1-dimensional electron waveguide.

6.4 Analysis of TEP in the Fabry-Perot regime

The electronic interactions in a clean metallic single walled carbon nanotube can be modeled by a 1D Luttinger-Liquid. The thermopower of a Luttinger-Liquid is

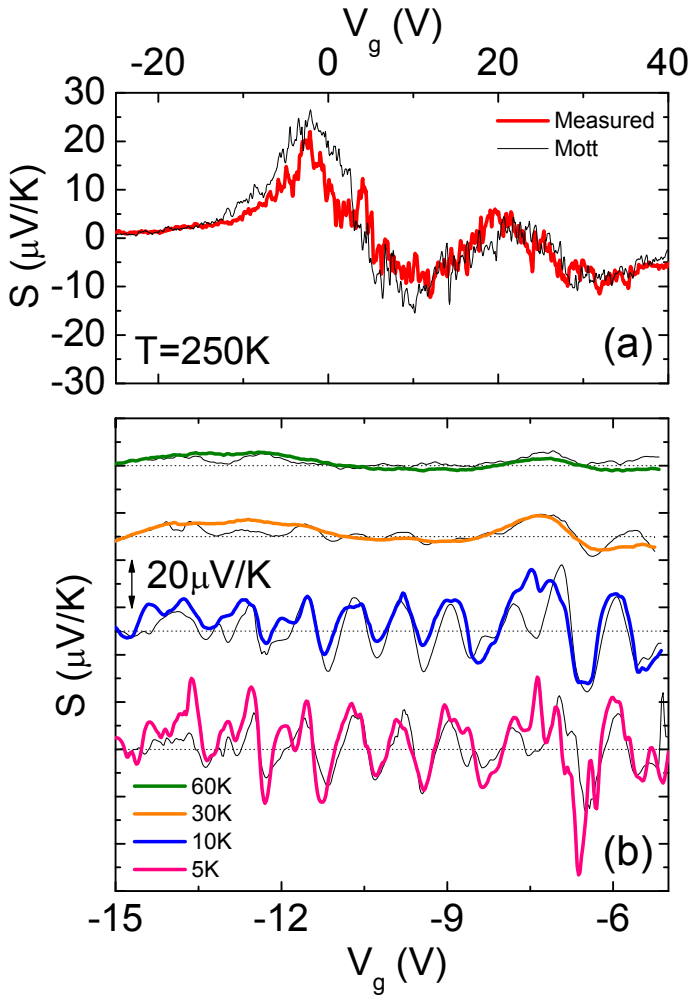

Figure 6.4: The measured (thick colored lines) and calculated (thin black lines) TEP using equation 5.9 as a function of gate voltage for $T = 250$ K (a) and $T = 60$ K, 30 K, 10 K, 5 K (b). The measured data follows the Mott relation well at high temperatures and also at low temperatures in the presence of Fabry-Perot oscillations.

predicted to follow the Mott relation for $T \ll T_L$ where $T_L = \frac{\hbar v_p}{k_B L}$, v_p is the plasmon velocity, and L is the device length [130]. Assuming that for single walled carbon nanotubes $v_p \approx v_F/g$ [131] and $g \approx .28$ [132] being the Luttinger-Liquid parameter characterizing the electron-electron interaction strength, we calculate $T_L \approx 80$ K in our 300 nm samples. For $T \gg T_L$ the magnitude of the thermopower should be renormalized by g to be larger than what is predicted by the Mott relation.

In order to test out the validity of this theory, we calculate the predicted thermopower using the Mott relation written down earlier in equation 5.9. In graphene, due to the 2D density of states, the gate coupling term, $\frac{dV_g}{dE_F}$, is simply dependent on the applied gate voltage. In single walled carbon nanotubes, however, the gate coupling term is determined by the conductance stability diagram at low temperatures. The gate coupling term is measured to be $\alpha = .01eV/V$ from equation 6.2 and the stability diagram in figure 6.3a. Figure 6.4a shows good agreement between the measured and calculated thermoelectric signal of a SWNT plotted as a function of gate voltage at $T = 250$ K. The Mott formula holds just as well in the low temperature Fabry-Perot regime, plotted in figure 6.4b. We are not observing signatures of the interactions predicted for Luttinger-Liquids most likely because the finite size energy scale is too large and we are not in the appropriate regime at the measurement temperature. Perhaps a very long nanotube ($L > 10$ μm) is a better model for the Luttinger-Liquid described by the above theory. Since $T_L \propto 1/L$, perhaps measuring the TEP of very long SWNTs would demonstrate signs of electron-electron interaction behavior. The semiclassical formalism predicts the observed TEP in this 1-dimensional material.

We were not able to experimentally probe the TEP in the Kondo transport regime in SWNTs. Since measuring the TEP requires a 10-terminal device and not a simple 2-terminal device, improving the yield of clean SWNT, required to observe the Kondo effect, is challenging but provides opportunity for further investigation of interaction physics in low dimensional carbon systems.

6.5 Summary

We have measured the conductance and thermopower of SWNT in the presence of Fabry-Perot oscillations at low temperatures. We used the Mott formula to confirm that the semiclassical formalism accurately predicts the thermoelectric response in highly conducting single walled carbon nanotubes. The TEP increases with decreasing temperature below $T = 30$ K due to the presence of quantum interference effects. In future experiments, it would be interesting to probe the thermopower in long ultra clean single walled carbon nanotubes in order to observe signatures of the 1-dimensional Luttinger-Liquid as well as the Kondo regime in carbon nanotube quantum dots where spin interactions are present.

Chapter 7

Conclusion

The dependence of the electronic and thermoelectric responses of several different nanoscale materials has been measured as a function of applied carrier density, temperature, diameter, and magnetic field. We have shown that we can reliably extract the carrier density of semiconducting nanowires, including Si nanowires and wide bandgap ZnO nanowires, using temperature dependent thermopower measurements where other methods produced inaccurate results. It has been observed that in the diameter range studied, the electronic power factor in chalcogenide Sb_2Te_3 nanowires is not appreciably enhanced as the diameter of the nanowires is decreased down to $\sim$30 nm. The thermoelectric response of graphene is similar to that in other 2-dimensional electron gases in both the zero magnetic field and high magnetic field limits. In both carbon materials studied, graphene and single walled carbon nanotubes, the electronic and thermoelectric responses are well correlated with each other through the semiclassical Mott relation. The linearity of the thermopower as a function of temperature in most of the materials studied indicates that diffusive thermoelectric generation is responsible for the observed signals.

The electronic and thermoelectric properties of the materials measured indicate that these materials, without any modification, are not strong candidates for thermoelectric energy conversion applications. However, studying the basic properties of nanoscale materials is the first step to integration of the materials into device applications. Because the materials can be enhanced with doping, chemical modification,

alloying, and geometric configurations that will be developed in future studies, there are possibilities that these advanced materials may be incorporated in high efficiency thermoelectric devices of the next generation.

Bibliography

[1] N. W. Ashcroft and N. D. Mermin, Solid State Physics (Thomson Learning, Inc., Stamford, CT, 1976).

[2] J. M. Ziman, Electrons and Phonons: The Theory of Transport Phenomena in Solids (Oxford University Press, New York, NY, 2001).

[3] I. S. Gradshteyn and I. M. Ryzhik, Table of Integrals, Series, and Products, 7th ed. (Academic Press, New York, NY, 2007).

[4] D. K. C. MacDonald, Thermoelectricity: An Introduction to the Principles (Dover Publications, New York, NY, 2006).

[5] T. H. Geballe and G. W. Hull, Physical Review **98**, 940 (1955).

[6] G. J. Snyder and E. S. Toberer, Nat Mater **7**, 105 (2008).

[7] F. Reif, Fundamentals of Statistical and Thermal Physics (McGraw-Hill, New York, NY, 1965).

[8] T. Harman and J. Honig, Thermoelectric and Thermomagnetic Effects and Application (McGraw-Hill, New York, NY, 1967).

[9] A. Majumdar, Science **303**, 777 (2004).

[10] C. B. Vining, Nature **413**, 577 (2001).

[11] M. S. Dresselhaus, G. Chen, M. Y. Tang, R. G. Yang, H. Lee, D. Z. Wang, Z. F. Ren, J. Fleurial, and P. Gogna, Advanced Materials **19**, 1043 (2007).

[12] A. I. Hochbaum, R. Chen, R. D. Delgado, W. Liang, E. C. Garnett, M. Najarian, A. Majumdar, and P. Yang, Nature **451**, 163 (2008).

[13] A. I. Boukai, Y. Bunimovich, J. Tahir-Kheli, J. Yu, W. A. G. III, and J. R. Heath, Nature **451**, 168 (2008).

[14] R. Kim, S. Datta, and M. S. Lundstrom, Journal of Applied Physics **105**, 034506 (2009).

[15] P. Yang, R. Yan, and M. Fardy, Nano Letters **10**, 1529 (2010).

[16] B. Poudel, Q. Hao, Y. Ma, Y. Lan, A. Minnich, B. Yu, X. Yan, D. Wang, A. Muto, D. Vashaee, X. Chen, J. Liu, M. S. Dresselhaus, G. Chen, and Z. Ren, Science **320**, 634 (2008).

[17] R. Venkatasubramanian, E. Siivola, T. Colpitts, and B. O'Quinn, Nature **413**, 597 (2001).

[18] T. E. Humphrey and H. Linke, Physical Review Letters **94**, 096601 (2005).

[19] Y. Lin, X. Sun, and M. S. Dresselhaus, Physical Review B **62**, 4610 (2000).

[20] L. D. Hicks and M. S. Dresselhaus, Physical Review B **47**, 16631 (1993).

[21] K. Bradley, S. Jhi, P. G. Collins, J. Hone, M. L. Cohen, S. G. Louie, and A. Zettl, Physical Review Letters **85**, 4361 (2000).

[22] T. C. Harman, P. J. Taylor, M. P. Walsh, and B. E. LaForge, Science **297**, 2229 (2002).

[23] R. C. Richardson, Experimental Techniques in Condensed Matter Physics at Low Temperatures (Perseus Books, New York, NY, 1988).

[24] O. Madelung, Semiconductors: Data Handbook, 3rd ed. (Springer, New York, NY, 2004).

[25] P. Horowitz and W. Hill, The Art of Electronics, 2nd ed. (Cambridge University Press, New York, NY, 1989).

[26] R. S. Muller and T. I. Kamins, Device Electronics for Integrated Circuits, 3rd ed. (John Wiley & Sons, New York, NY, 2002).

[27] W. Lu, J. Xiang, B. P. Timko, Y. Wu, and C. M. Lieber, Proceedings of the National Academy of Sciences of the United States of America **102**, 10046 (2005).

[28] J. Xiang, W. Lu, Y. Hu, Y. Wu, H. Yan, and C. M. Lieber, Nature **441**, 489 (2006).

[29] G. Liang, J. Xiang, N. Kharche, G. Klimeck, C. M. Lieber, and M. Lundstrom, Nano Letters **7**, 642 (2007).

[30] Y. Hu, J. Xiang, G. Liang, H. Yan, and C. M. Lieber, Nano Letters **8**, 925 (2008).

[31] Y. Cui, X. Duan, J. Hu, and C. M. Lieber, The Journal of Physical Chemistry B **104**, 5213 (2000).

[32] Y. Cui, Z. Zhong, D. Wang, W. U. Wang, and C. M. Lieber, Nano Letters **3**, 149 (2003).

[33] G. Zheng, W. Lu, S. Jin, and C. M. Lieber, Advanced Materials **16**, 1890 (2004).

[34] Y. Wu, Y. Cui, L. Huynh, C. J. Barrelet, D. C. Bell, and C. M. Lieber, Nano Letters **4**, 433 (2004).

[35] Z. Zhong, Y. Fang, W. Lu, and C. M. Lieber, Nano Letters **5**, 1143 (2005).

[36] G. Yi, C. Wang, and W. I. Park, Semiconductor Science and Technology **20**, S22 (2005).

[37] P. J. Pauzauskie and P. Yang, Materials Today **9**, 36 (2006).

[38] C. Lee, G. Yi, Y. M. Zuev, and P. Kim, Applied Physics Letters **94**, 022106 (2009).

[39] Y. M. Zuev, J. P. Small, Y. Hu, Y. Fang, C. M. Lieber, and P. Kim, to be submitted to Applied Physics Letters .

[40] P. Xie, Y. Hu, Y. Fang, J. Huang, and C. M. Lieber, Proceedings of the National Academy of Sciences **106**, 15254 (2009).

[41] J. P. Small, Ph.D. thesis, Columbia University, 2006.

[42] W. I. Park, D. H. Kim, S. Jung, and G. Yi, Applied Physics Letters **80**, 4232 (2002).

[43] M. Cutler, J. F. Leavy, and R. L. Fitzpatrick, Physical Review **133**, A1143 (1964).

[44] M. Cutler and N. F. Mott, Physical Review **181**, 1336 (1969).

[45] A. Ohtomo, M. Kawasaki, I. Ohkubo, H. Koinuma, T. Yasuda, and Y. Segawa, Applied Physics Letters **75**, 980 (1999).

[46] A. Hutson, Journal of Physics and Chemistry of Solids **8**, 467 (1959).

[47] S. A. Dayeh, C. Soci, P. K. L. Yu, E. T. Yu, and D. Wang, Applied Physics Letters **90**, 162112 (2007).

[48] Z. Zhang, X. Sun, M. S. Dresselhaus, J. Y. Ying, and J. P. Heremans, Applied Physics Letters **73**, 1589 (1998).

[49] J. Heremans and C. M. Thrush, Physical Review B **59**, 12579 (1999).

[50] J. Heremans, C. M. Thrush, Y. Lin, S. Cronin, Z. Zhang, M. S. Dresselhaus, and J. F. Mansfield, Physical Review B **61**, 2921 (2000).

[51] Y. Lin, O. Rabin, S. B. Cronin, J. Y. Ying, and M. S. Dresselhaus, Applied Physics Letters **81**, 2403 (2002).

[52] W. Shim, J. Ham, K. il Lee, W. Y. Jeung, M. Johnson, and W. Lee, Nano Letters **9**, 18 (2009).

[53] W. Shim, D. Kim, K. il Lee, K. J. Jeon, J. Ham, J. Chang, S. Han, W. Y. Jeung, M. Johnson, and W. Lee, Journal of Applied Physics **104**, 073715 (2008).

[54] C. Harmans, Mesoscopic Physics: An Introduction (Delft University, Delft, Netherlands, 1997).

[55] T. Thonhauser, T. J. Scheidemantel, J. O. Sofo, J. V. Badding, and G. D. Mahan, Physical Review B **68**, 085201 (2003).

[56] D. Hsieh, Y. Xia, D. Qian, L. Wray, F. Meier, J. H. Dil, J. Osterwalder, L. Patthey, A. V. Fedorov, H. Lin, A. Bansil, D. Grauer, Y. S. Hor, R. J. Cava, and M. Z. Hasan, Physical Review Letters **103**, 146401 (2009).

[57] H. Peng, K. Lai, D. Kong, S. Meister, Y. Chen, X. Qi, S. Zhang, Z. Shen, and Y. Cui, Nature Materials **9**, 225 (2010).

[58] V. A. Kulbachinskii, Z. M. Dashevskii, M. Inoue, M. Sasaki, H. Negishi, W. X. Gao, P. Lostak, J. Horak, and A. de Visser, Physical Review B **52**, 10915 (1995).

[59] M. Wuttig, Nature Materials **4**, 265 (2005).

[60] J. S. Dyck, W. Chen, C. Uher, C. Drasar, and P. Lost'ak, Physical Review B **66**, 125206 (2002).

[61] J. Jiang, L. Chen, S. Bai, Q. Yao, and Q. Wang, Journal of Crystal Growth **277**, 258 (2005).

[62] Y. Q. Cao, X. B. Zhao, T. J. Zhu, X. B. Zhang, and J. P. Tu, Applied Physics Letters **92**, 143106 (2008).

[63] Y. M. Zuev, J. S. Lee, C. Galloy, H. Park, and P. Kim, Nano Letters **10**, 3037 (2010).

[64] J. S. Lee, S. Brittman, D. Yu, and H. Park, Journal of the American Chemical Society **130**, 6252 (2008).

[65] B. Roy, B. R. Chakraborty, R. Bhattacharya, and A. K. Dutta, Solid State Communications **25**, 617 (1978).

[66] V. A. Kulbachinskii, A. Y. Kaminskii, N. Miyajima, M. Sasaki, H. Negishi, M. Inoue, and H. Kadomatsu, Journal of Experimental and Theoretical Physics Letters **70**, 767 (1999).

[67] J. Zhou, C. Jin, J. H. Seol, X. Li, and L. Shi, Applied Physics Letters **87**, 133109 (2005).

[68] R. Hartman, Physical Review **181**, 1070 (1969).

[69] H. W. Kroto, J. R. Heath, S. C. O'Brien, R. F. Curl, and R. E. Smalley, Nature **318**, 162 (1985).

[70] S. Iijima, Nature **354**, 56 (1991).

[71] K. S. Novoselov, A. K. Geim, S. V. Morozov, D. Jiang, Y. Zhang, S. V. Dubonos, I. V. Grigorieva, and A. A. Firsov, Science **306**, 666 (2004).

[72] Y. Zhang, Y. Tan, H. L. Stormer, and P. Kim, Nature **438**, 201 (2005).

[73] K. S. Novoselov, A. K. Geim, S. V. Morozov, D. Jiang, M. I. Katsnelson, I. V. Grigorieva, S. V. Dubonos, and A. A. Firsov, Nature **438**, 197 (2005).

[74] A. K. Geim and K. S. Novoselov, Nat Mater **6**, 183 (2007).

[75] A. H. C. Neto, F. Guinea, N. M. R. Peres, K. S. Novoselov, and A. K. Geim, Reviews of Modern Physics **81**, 109 (2009).

[76] Y. M. Zuev, W. Chang, and P. Kim, Physical Review Letters **102**, 096807 (2009).

[77] P. Wei, W. Bao, Y. Pu, C. N. Lau, and J. Shi, Physical Review Letters **102**, 166808 (2009).

[78] J. G. Checkelsky and N. P. Ong, Physical Review B **80**, 081413 (2009).

[79] S. Ghosh, W. Bao, D. L. Nika, S. Subrina, E. P. Pokatilov, C. N. Lau, and A. A. Balandin, Nat Mater **9**, 555 (2010).

[80] J. H. Seol, I. Jo, A. L. Moore, L. Lindsay, Z. H. Aitken, M. T. Pettes, X. Li, Z. Yao, R. Huang, D. Broido, N. Mingo, R. S. Ruoff, and L. Shi, Science **328**, 213 (2010).

[81] R. Saito, G. Dresselhaus, and M. S. Dresselhaus, Physical Properties of Carbon Nanotubes (Imperial College Press, London, 1998).

[82] P. R. Wallace, Physical Review **71**, 622 (1947).

[83] K. S. Novoselov, D. Jiang, F. Schedin, T. J. Booth, V. V. Khotkevich, S. V. Morozov, and A. K. Geim, Proceedings of the National Academy of Sciences of the United States of America **102**, 10451 (2005).

[84] P. Blake, E. W. Hill, A. H. C. Neto, K. S. Novoselov, D. Jiang, R. Yang, T. J. Booth, and A. K. Geim, Applied Physics Letters **91**, 063124 (2007).

[85] J. Yan, Y. Zhang, S. Goler, P. Kim, and A. Pinczuk, Solid State Communications **143**, 39 (2007).

[86] J. Martin, N. Akerman, G. Ulbricht, T. Lohmann, J. H. Smet, K. von Klitzing, and A. Yacoby, Nature Physics **4**, 144 (2008).

[87] S. Adam, E. H. Hwang, V. M. Galitski, and S. D. Sarma, Proceedings of the National Academy of Sciences **104**, 18392 (2007).

[88] K. I. Bolotin, K. J. Sikes, J. Hone, H. L. Stormer, and P. Kim, Physical Review Letters **101**, 096802 (2008).

[89] J. Cayssol, B. Huard, and D. Goldhaber-Gordon, Physical Review B **79**, 075428 (2009).

[90] E. H. Hwang and S. D. Sarma, Physical Review B **77**, 115449 (2008).

[91] E. H. Hwang, E. Rossi, and S. D. Sarma, Physical Review B **80**, 235415 (2009).

[92] T. Stauber, N. M. R. Peres, and F. Guinea, Physical Review B **76**, 205423 (2007).

[93] M. S. Foster and I. L. Aleiner, Physical Review B **77**, 195413 (2008).

[94] M. S. Foster and I. L. Aleiner, Physical Review B **79**, 085415 (2009).

[95] U. Sivan and Y. Imry, Physical Review B **33**, 551 (1986).

[96] L. D. Landau and L. M. Lifshitz, Quantum Mechanics Non-Relativistic Theory, Third Edition: Volume 3, 3rd ed. (Butterworth-Heinemann, India, 1981).

[97] S. Datta, Electronic Transport in Mesoscopic Systems (Cambridge University Press, Cambridge, UK, 1997).

[98] A. Tzalenchuk, S. Lara-Avila, A. Kalaboukhov, S. Paolillo, M. Syvajarvi, R. Yakimova, O. Kazakova, J. J. B. M., V. Fal'ko, and S. Kubatkin, Nature Nanotechnology **5**, 186 (2010).

[99] S. M. Girvin and M. Jonson, Journal of Physics C: Solid State Physics **15**, L1147 (1982).

[100] H. Oji, Journal of Physics C: Solid State Physics **17**, 3059 (1984).

[101] M. Jonson and S. M. Girvin, Physical Review B **29**, 1939 (1984).

[102] P. Streda, Journal of Physics: Condensed Matter **1**, 1025 (1989).

[103] H. Obloh, K. von Klitzing, and K. Ploog, Surface Science **142**, 236 (1984).

[104] T. Fromhold, P. Butcher, G. Qin, B. Mulimani, J. Oxley, and B. Gallagher, Surface Science **263**, 183 (1992).

[105] H. van Houten, L. W. Molenkamp, C. W. J. Beenakker, and C. T. Foxon, Semiconductor Science and Technology **7**, B215 (1992).

[106] D. A. Abanin, K. S. Novoselov, U. Zeitler, P. A. Lee, A. K. Geim, and L. S. Levitov, Physical Review Letters **98**, 196806 (2007).

[107] D. A. Abanin and L. S. Levitov, Physical Review B **78**, 035416 (2008).

[108] J. R. Williams, D. A. Abanin, L. DiCarlo, L. S. Levitov, and C. M. Marcus, Physical Review B **80**, 045408 (2009).

[109] C. Dean, A. Young, I. Meric, C. Lee, L. Wang, S. Sorgenfrei, K. Watanabe, T. Taniguchi, P. Kim, K. Shepard, and J. Hone, Nature Nanotechnology **5**, 722 (2010).

[110] W. Liang, M. Bockrath, D. Bozovic, J. H. Hafner, M. Tinkham, and H. Park, Nature **411**, 665 (2001).

[111] K. Grove-Rasmussen, H. Jorgensen, and P. Lindelof, Physica E: Low-dimensional Systems and Nanostructures **40**, 92 (2007).

[112] W. Liang, M. Bockrath, and H. Park, Physical Review Letters **88**, 126801 (2002).

[113] P. Jarillo-Herrero, S. Sapmaz, C. Dekker, L. P. Kouwenhoven, and H. S. J. van der Zant, Nature **429**, 389 (2004).

[114] P. Jarillo-Herrero, J. Kong, H. S. van der Zant, C. Dekker, L. P. Kouwenhoven, and S. D. Franceschi, Nature **434**, 484 (2005).

[115] R. Scheibner, H. Buhmann, D. Reuter, M. N. Kiselev, and L. W. Molenkamp, Physical Review Letters **95**, 176602 (2005).

[116] P. Kim, L. Shi, A. Majumdar, and P. L. McEuen, Physical Review Letters **87**, 215502 (2001).

[117] C. Yu, L. Shi, Z. Yao, D. Li, and A. Majumdar, Nano Letters **5**, 1842 (2005).

[118] K. Schwab, E. A. Henriksen, J. M. Worlock, and M. L. Roukes, Nature **404**, 974 (2000).

[119] J. P. Small, K. M. Perez, and P. Kim, Physical Review Letters **91**, 256801 (2003).

[120] M. C. Llaguno, J. E. Fischer, A. T. Johnson, and J. Hone, Nano Letters **4**, 45 (2004).

[121] V. V. Deshpande, B. Chandra, R. Caldwell, D. S. Novikov, J. Hone, and M. Bockrath, Science **323**, 106 (2009).

[122] D. Mann, A. Javey, J. Kong, Q. Wang, and H. Dai, Nano Letters **3**, 1541 (2003).

[123] L. Huang, X. Cui, B. White, and S. P. OBrien, The Journal of Physical Chemistry B **108**, 16451 (2004).

[124] Y. Li, D. Mann, M. Rolandi, W. Kim, A. Ural, S. Hung, A. Javey, J. Cao, D. Wang, E. Yenilmez, Q. Wang, J. F. Gibbons, Y. Nishi, and H. Dai, Nano Letters **4**, 317 (2004).

[125] A. R. Harutyunyan, G. Chen, T. M. Paronyan, E. M. Pigos, O. A. Kuznetsov, K. Hewaparakrama, S. M. Kim, D. Zakharov, E. A. Stach, and G. U. Sumanasekera, Science **326**, 116 (2009).

[126] Z. Yao, C. L. Kane, and C. Dekker, Physical Review Letters **84**, 2941 (2000).

[127] B. Chandra, R. Caldwell, M. Huang, L. Huang, M. Y. Sfeir, S. P. O'Brien, T. F. Heinz, and J. Hone, Physica Status Solidi (b) **243**, 3359 (2006).

[128] M. S. Purewal, B. H. Hong, A. Ravi, B. Chandra, J. Hone, and P. Kim, Physical Review Letters **98**, 186808 (2007).

[129] S. Cho and M. S. Fuhrer, arXiv:0901.4157 (2009).

[130] I. V. Krive, I. A. Romanovsky, E. N. Bogachek, A. G. Scherbakov, and U. Landman, Low Temperature Physics **27**, 821 (2001).

[131] Z. Zhong, N. M. Gabor, J. E. Sharping, A. L. Gaeta, and P. L. McEuen, Nature Nanotechnology **3**, 201 (2008).

[132] M. Bockrath, D. H. Cobden, J. Lu, A. G. Rinzler, R. E. Smalley, L. Balents, and P. L. McEuen, Nature **397**, 598 (1999).